Pulsatile Electropolishing of Nitinol Stents

By

Jeran Andre Cloete

CLTJER001

SUBMITTED TO THE UNIVERSITY OF CAPE TOWN

In fulfilment of the requirements for the degree

MSc (Med) in Biomaterials

Faculty of Health Sciences

UNIVERSITY OF CAPE TOWN

Date of submission: 11-02-2019

Supervisors:

Associate Professor Deon Bezuidenhout, Department of Surgery, UCT

Associate Professor Pieter Levecque, Department of Chemical Engineering, UCT

Jandre de Villiers, PhD, Senior Research Scientist, SAT

DECLARATION

I, Jeran Cloete, hereby declare that the work on which this dissertation/thesis is based is my original work (except where acknowledgements indicate otherwise) and that neither the whole work nor any part of it has been, is being, or is to be submitted for another degree in this or any other university. I empower the university to reproduce for the purpose of research either the whole or any portion of the contents in any manner whatsoever.

Signature:

Signed by candidate

Date: 11-02-2019

ACKNOWLEDGEMENTS

I would like to convey my sincere gratitude to the bursar, and my employer Strait Access Technologies who provided boundless opportunities for me to explore new topics and satisfy my scientific curiosity.

To my supervisor, Deon Bezuidenhout for keeping me motivated and providing infrastructure and tutelage in academic matters. The co-supervisors, Pieter Levecque and Jandre De Villiers who provided unfettered access to their laboratories and equipment with endless time to provide guidance and discussion on its usage.

Additionally, the staff of the electron microscope unit at UCT deserve respect for their professional management of the equipment and helpful attitude. My thanks to Miranda Waldron, Nasheeta Hanief and Michael Woodward.

I am particularly indebted to Whelan Mohali of Stellenbosch University for selflessly providing his time and assistance in using their Atomic Force Microscope.

Special thanks to all my colleagues at SAT for their endless interest and willingness to act as sounding boards for ideas and thoughts as the project progressed, as well as their faith in my abilities which kept me motivated through failures and dead ends.

To my family who supported me and provided feedback on draft versions, my wife, Julia Laurie, and mother, Rencia Cloete I convey boundless gratitude and love.

ABSTRACT

Alloys that oxidize easily such as those containing titanium or chromium present a challenge to electropolishing because the polarization that dissolves the metal species produces positive ions, these oxidize and form stable surface layers of metallic oxides that prevent further dissolution. This is usually overcome with the use of acid solutions that dissolve the metallic oxide. This thesis aims to shift the primary control of the electropolishing effect from electrolyte variables to a combination of potential variation and hydrodynamic interference. Traditionally this is achieved with one continuous mass removal process that operates after a steady state of dissolution is established, generally requiring hydrofluoric or phosphoric acid to achieve titanium dioxide breakdown. The resulting concentration gradient is heavily affected by electrolyte variables such as viscosity and electrical resistance, while the electrical polarization is constrained by the metallic oxide reaction rate which creates a complex net of interdependent variables that can be difficult to tune. A rapidly changing electric field was applied to modulate the alloying element dissolution rates. In tandem with the electropolishing development, stages prior to the electropolishing step were selectively removed to simplify the process.

Utilizing a three electrode system and an external potentiostat controller to permit greater flexibility, a variety of alternating current pulsatile waveforms were investigated and the resulting effect on surface topology was observed using SEM and AFM microscopes. Differential pulse voltammogram yielded a feedback parameter on surface composition, and various pulse parameters were adjusted to optimize for surface smoothness, and identify the primary control variable.

An electropolishing method is presented which achieves a $\sim$50% reduction in the Sa surface roughness value to an area average of 45 nm on a laser cut tubular stent geometry. It is shown that this method can be adapted to eliminate the need for chemical etching or mechanical polishing prior to electropolishing. The resulting polished surface displays corrosion resistance equivalent or better than other electropolished Nitinol surfaces from literature with a breakdown potential $>$1V vs SCE, and a similarly high repassivation potential.

Balancing the charge in the anodic and cathodic pulses was the key to minimizing the resulting surface roughness, and eliminating micropits. Nitinol is a nearly binary alloy of NiTi and a charge transfer ratio of 1 yielded the smoothest surfaces at current densities around $\sim$1 A/cm^2. The initial surface condition was found to be irrelevant to electropolishing control with respect to oxide composition, provided enough mass was removed to fully dissolve the initial layers of mixed composition.

Contents

List of Figures

List of Abbreviations

Acronym	Full Name
SEM	Scanning Electron Microscope
EDS	Energy Dispersive X-Ray Spectroscopy
EIS	Electrochemical Impedance Spectroscopy
CA	Chronoamperometry
CV	Chronovoltammetry
AFM	Atomic Force Microscope
DSC	Digital Scanning Calorimeter
XPS	X-ray Photoelectron Spectroscopy
ASTM	American Society for Testing and Materials
As	austenitic Start (temperature)
Af	austenitic Finish (temperature)
Ms	martensitic Start (temperature)
Mf	martensitic Finish (temperature)
WE	Working Electrode
CE	Counter Electrode
RE	Reference Electrode
SAT	Strait Access Technologies
DC	Direct Current
AC	Alternating Current

Table 1: List of Abbrevations

Chapter 1

Literature Review

1.1 Introduction

1.1.1 Project Rationale

The three commonly used medical implant materials based on titanium, and chrome alloys share a common feature in their processing requirements. Especially when used to create permanent implants, materials such as Nitinol, Cobalt-chromium and Stainless Steel must be exposed to some form of surface treatment that removes the toxic elements in the alloys from the surface layer. In addition, when used for vascular implants, it is usually desirable to create an extremely smooth surface that will not form nucleation points for cells to gather and create anomalous growth or accretion patterns. It is known that cyclic polarization between positive and negative potentials at high currents can yield an electropolishing effect. This was developed to deal with alloys and metals composed of components that have discrete non overlapping potential-pH regions in which their oxidized (passivated) species are stable. Generally such highly passivating materials have stable oxidized species at positive potentials in aqueous systems, thus it is difficult to maintain anodic dissolution.

Strait Access Technologies (SAT) is currently making use of Nitinol and Cobalt chromium in the above applications and requires an electropolishing solution to support medical device development and eventually mass market manufacture. Nitinol electropolishing was chosen for further development because of its demanding processing requirements which could potentially be eliminated by electropolishing.

1.1.2 Background on Nitinol

Developed in the 1960's, Nitinol was initially valuable for its high elasticity and hardness, which made it useful for engineering applications such as earthquake dampeners.[1] In recent decades it has become useful in biomedical applications due to advances in processing technology which permit it to be manufactured in increasingly complex and small geometries[2]. A significant hurdle to utilizing Nitinol as an implant material is the nickel content. Nickel cannot be allowed to enter the body in

significant quantities, and so the Nitinol surface must be made free of nickel and resistance to corrosion in its intended environment[3]. Nitinol stents are used to treat a variety of complications in tubular structures and organs, from the gastric to the coronary system. This variety of physiological conditions requires surface treatments which can withstand corrosion in this wide range of environments and even promote a favourable cellular response. Surface treatments and coatings can be difficult to apply to irregular or dissimilar surface compositions. Thus, chemical etching or electropolishing is usually required prior to further surface modifications, if not the final processing stage[4][5][6].

1.2 Overview of Surface Treatments

Hassel provides a handy diagram (1.1) outlining the various surface treatment options that have been applied to Nitinol (NiTi).

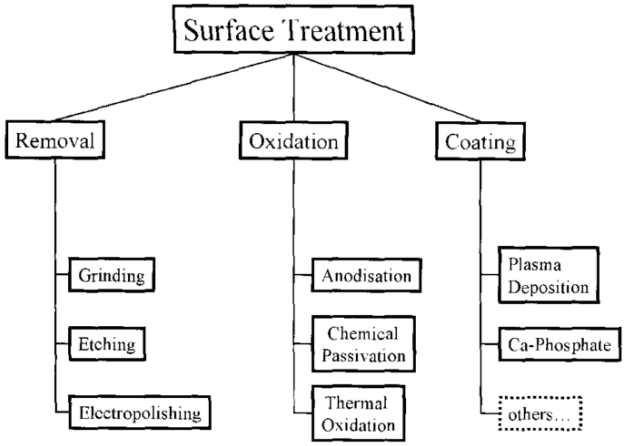

Figure 1.1: NiTi Surface Treatment Options [7]

The primary technique is considered removal, which covers grinding, etching and electropolishing. Grinding NiTi has some challenges due to the super-elastic nature of the alloy which leads to local deformation under mechanical loads damping the grinding result depending on the part geometry. Mechanical deformation of the crystalline structure in the surface layer can carry over into the polishing and coating processes (although this can be mitigated somewhat by the application of extremely fine polishing slurries). Thus, mechanical polishing must be used with caution on Nitinol.[7] An alternative to grinding is chemical etching which can be achieved with acid or alkaline solutions. The etchant must have its pH tuned to the metal being etched by referring to the relevant Pourbaix diagrams that outline the material's electrochemical stability versus pH for its various redox states[8]. The etching process is strongly influenced by metallurgic properties such as grain structure and crystallographic phase of Nitinol, which can result in anisotropic etching along grain

boundaries.[7]

Electropolishing is based on the principle of creating a dense metallic ion concentration gradient in the immediate vicinity of the metal surface that tapers off into the bulk solution. Asperities protrude through the concentration gradient into areas of lower concentration and are thus preferentially removed. Polarizing the system pushes the reaction towards the ionic side of equation 1.1 resulting in continuous dissolution of the metal surface. When the charge density is high enough, the concentration gradient forms a saturated layer directly on the surface of the anode several micrometers thick. Once again, in the special case of shape memory alloys like Nitinol, the phase of the crystal lattice must be taken into consideration. In the martensitic phase surface patterns will form during electropolishing.

$$M \rightarrow M^{+n} + ne^{-} \tag{1.1}$$

Passivation of Nitinol surfaces is critical for medical applications to prevent nickel release and enhance corrosion resistance. The primary method is the formation of a titanium oxide layer on the surface. This layer can be formed in several ways, but the most effective method includes a preliminary step of selective nickel dissolution prior to titanium oxide formation to ensure a low nickel content in the passivation film.[7]

A calcium phosphate coating can be applied to increase the adsorbance of human cells. This effect is dependant on high porosity of the crystalline structure of the calcium phosphate. Saturation of the coating solution is necessary to ensure continuous nucleation. Choi et al. [9] report on a supersaturated solution of 1.8 mM K^{+} , 3.0 mM Ca^{2+}, 1.8 mM $H_2PO_4^{-}$, 6.0 mM NO_3^{-} which achieved a $10\mu m$ coating after 24h at 20 °C.[9]

Electrochemical etching is one of the most suitable methods for micro-machining shape memory alloys. It is a very important technique for the manufacture of micro actuators.[10] Electrochemical etching for the formation of Nitinol stents has a massive advantage over conventional laser-based process flows because it incorporates several manufacturing steps into one. It can be considered electropolishing tuned to obtain a high material removal rate. Inman et al. demonstrated the effectiveness of pulse reverse waveforms for the electrochemical etching of Nitinol coupons with a pattern intended to simulate a stent that had 50-100 µm strut widths with slots 38-400 µm between them. Their target for a "feasible" process was an etching rate of 25 µm/min. Their application of pulse reverse process control allows them to use an aqueous electrolyte of 30 wt% sulfuric acid.[11] Mineta et al. were able to successfully manufacture Nitinol actuators from sheets and small diameter tubes with 60 µm struts spaced 20 µm apart in a wiggly pattern on a 30 µm thick substrate. They tested a variety of unconventional electrolytes utilizing conventional DC process control. Due to their need to limit the etching rate because of the low thickness and strut widths, their most successful solution was 1.0 mol/l LiCl in ethanol. However, they obtained etch rates of 10 µm/min when the ethanol was substituted for methanol. It was noted that lower LiCl concentration of 0.1mol/l in ethanol resulted in a rougher surface post etching as well as lower etch rates. One of the issues faced

in etching through a material to form micro actuators is the change that occurs as the etching breaks through in some areas and becomes severely non uniform due to the altered current density distribution. To combat this, Mineta et al. applied a backing layer of copper to the Nitinol by plating the inside of the tube and the back of a sheet. This was effective due to the lower etching rate of Cu which was easily removed in concentrated nitric acid post-process without damaging the SMA actuator. In 1.0 mol/l H_2SO_4 in methanol, etching rates of 16 µm/min could be depressed to 2.7 µm/min by switching to ethanol.[10]

Some chemical solutions reviewed in other literature are summarized in Appendix A.

1.3 The Nitinol Alloy

There are three common fabrication methods for Nitinol: vacuum induction melting, vacuum arc melting and electron beam melting. After ingot production by one of these three methods, the material is further processed by conventional methods into tubes, plates, rods, wires, etc. Often, laser based processing is used to convert these basic forms into more complex geometries with high precision. Alternatively, Nitinol can be sintered from a powder in furnace or with a laser in a 3D printer. Although, applying one of the three methods above and then converting the ingot into a powder produces a more homogeneous result than starting with Ni and Ti powders[12, 13]. The mechanical behaviour and chemical properties of a Nitinol part are dependant on the crystallographic and granular structure. Thus, the behaviour of the final part is dependant on the entire processing history.[14]

1.3.1 Titanium Dioxide Passive Layers

Titanium dioxide exhibits extreme polymorphism. There are four commonly found crystal structures which exhibit different band gap energies. This is important to note in electropolishing as it directly affects the charge transfer. The presence of impurities and multi-phase crystals makes it impossible to use standard values for this band gap. However, studies have produced accurate Raman Spectra and X-ray diffraction spectra. Monai [15] report a consensus on the band gap values of rutile (3.02eV) and anatase (3.2eV) TiO_2 [15]. Thus, it may be possible to determine the dominant polymorph in the TiO_2 surface layer of Nitinol. If this can be controlled by electrical parameters it may yield an avenue to modify the passivity of the surface during electropolishing.

Titanium alloys form titanium oxide surface layers that can be catalysed by annealing at temperatures above 300 °C. Zhu et al. studied the oxide layer thickness, composition and response to a cyclic potential scan, after various exposure times to different temperatures. They used Focused Ion Beam microscopy (FIB) to look at a cross section of heat treated Nitinol wire, which provided enough contrast to visually identify the different species of titanium oxides and nickel alloys. A layered microstructure of TiO_2 and Ni_xTi was found to form after longer heat treatments.

In Figure 1.2, referring to other publications, Zhu et al. were able to identify the composition of the nickel alloys as layers of Ni_3Ti and Ni_4Ti, while identifying regions of pure nickel as white areas using backscattered electron imaging. Black spots in the TiO_2 layers were labelled as voids which were filled with nickel at greater depths below the surface layer.[16] Unfortunately, only general conclusions can be drawn from this work because there is no reference to the raw material phase transition temperatures, and Nitinol is known to exhibit drastically different behaviour depending on its crystal format. The lamellar structure of the alternating TiO_2 and Ni_3Ti alloys is noted, as it may lead to short-duration electrodynamic observations of the initial potentiostat scans on the surface layers that do not hold for further "bulk" material redox reactions.

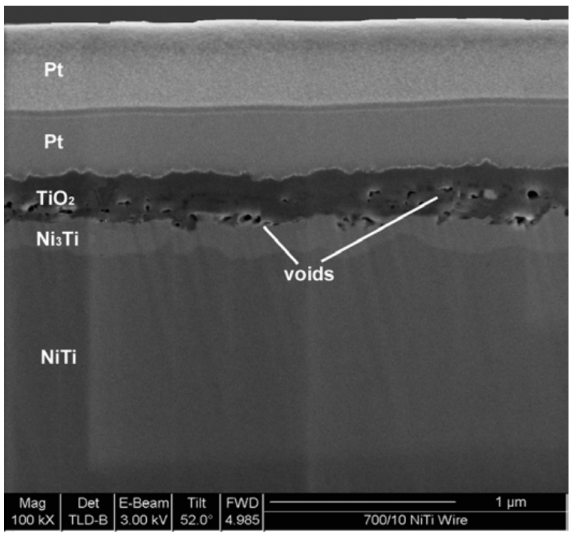

(a)

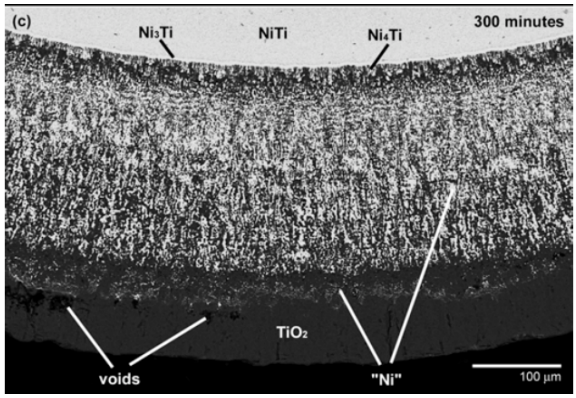

(b)

Figure 1.2: (a) Focused ion beam microscope image of NiTi at 100,000x magnification after heat treatment at 700 °C for 10 minutes (b) BEI image of Nitinol wire cross section after electropolishing and heat treatment at 1000 °C for 300 minutes [16]

Jerkiewicz [17]discovered that the titanium oxide layer formed at the surface of a titanium electrode could be reversibly modified. A sine wave alternating current operating at a frequency of 60 Hz and voltages between 0-80 Vac was able to adjust the colour of the titanium oxide layer. The colour is a result of optical absorption and reflection that is dependent on the layer thickness. The reversibility of this phenomenon was attributed to the presence of fluorine ions in the NH_4BF_4 solution (7.5 wt%). According to these authors literature review, fluorine ions are instrumental in controlling the titanium dioxide dissolution rate.

1.3.2 Solid-Solid Phase Transition

The solid-solid phase transition shown in figure 1.3 that occurs during heating or cooling of Nitinol can be analysed using Differential Scanning Calorimetry (DSC). Nitinol displays two distinct cubic and monoclinic solid crystal phases with drastically different physical properties. The transition displays hysteresis and is independent of temperature change rate. The hysteresis (which usually falls between 25-50 °C) can be used to determine the nickel and titanium percentages in the material. A third rhombohedral phase can also be found when it is exposed to thermal stress through thermal cycling. The rhombohedral or "R" phase is only stable during cooling, and manifests as a distinct dip in the peak of the heat flow DSC graph during the transition from cubic to monoclinic phases. [18]

The different lattice microstructures will lead to surface patterns during anodic stripping applied while electropolishing. Therefore, the selection of temperature is critical and the thermal history is of paramount importance in this selection. If thermal processing is applied, one must take care to account for the large hysteresis value to ensure a complete phase transition occurs.

The temperature dependence of the Nitinol's phase is interwoven with its dependence on strain, and due to the large hysteresis, the transition zones actually represent an area after which one of the three phases is eliminated. Until the hysteresis has been overcome and the phase transition is complete, the alloy will present a combination of its three polymorphs (austenite, martensite and rhombic).

Feeney [19] reported that large errors in transition temperature measurements by DSC are a result of residual stresses from processing. Annealing the material can allow DSC to provide accurate measurements.[19]

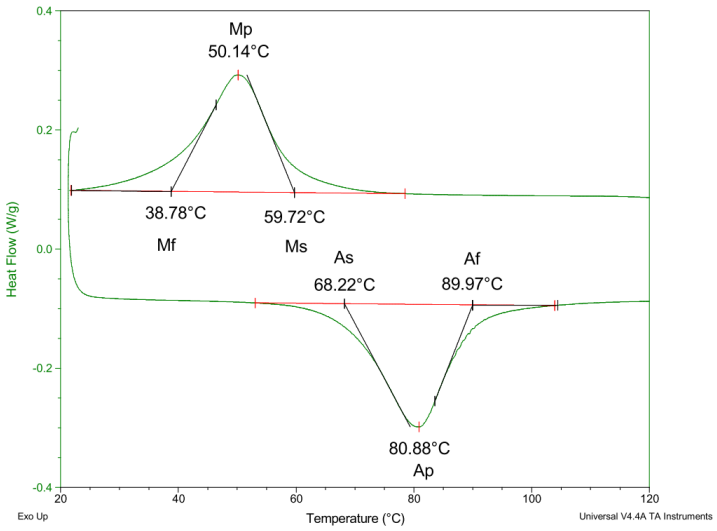

AFM

Figure 1.3: Nitinol Solid-Solid Phase transition (without R phase) [18]

1.3.3 Alternative Surfaces Topologies

Reduction in surface roughness is not the only objective of electropolishing. Depending on the process parameters, a variety of effects can be observed affecting the surface finish. The main body of literature on electropolishing is concerned with the mitigation of these effects to gain the smoothest possible surface free from defects and thoroughly passivated for corrosion resistance. Apolinario et al.[20] have found the "waviness" profile produced by specific polishing parameters a useful pre treatment for the formation of titanium dioxide nano tubules (NTs). The theory here is that the peaks of the polished sample provide initiation points for the formation of TiO_2 NTs, thus controlling the peak spacing. Uniformity and root mean square roughness average (R_q) value has significant effect on the resultant NTs formed after anodization.

It was found that specific parameters used to polish high purity titanium foils yielded a particularly uniform surface profile that did not correspond to the lowest surface roughness of the samples tested. Apolinario et al. observed that a greater reduction in surface roughness required higher EP voltage which resulted in a higher incidence of surface defects. These create focal points in the electric field when depositing NTs. Optimizing for the spacial period (SP) of the peaks and valleys on the surface yielded the best SP for the nucleation of NTs.[20]

While this may not be of immediate interest for the polishing of medical stents, it is worth noting that the surface reaction is not purely dependent on absolute surface roughness and passivity. Depending on the local environment of the polished sample, the spacial period of the surface profile may be of interest.

Huan et al. discovered a way to generate numerous uniform micropits across the surface of Nitinol, shown in the SEM images in Figure 1.4. The objective in this case was to create a hybrid structure of micropits filled with nanotubes that could potentially enhance the osseointegration abilities of Nitinol bone implants. The method used to generate the micropits was electrochemical etching (EE) in a solution of 65% nitric acid in methanol. SEM and surface roughness analysis showed an increase in average surface roughness (R_a) values with increasing etching time. The diameter of the pits rises to approach 1 µm after 30 minutes of EE. The resulting microstrucure has a uniform porous appearance. This initial etching result is poorly attached to the substrate with black material coming off in ultrasonic cleaning. Exposure to a solution of 20% nitric acid at 80 °C for 20 minutes removed the residual material to expose the underlying micropits. Etching titanium in this way to increase surface roughness, and consequent bio-actitivity of implants, is common practice. However, the technique is seldom applied to Nitinol, most likely due to the difficulty controlling nickel distribution in the surface with the high dissolution potential of nickel in this process. In this study, the uniform micropits were subsequently anodized in a solution containing fluoride ions to form nanotubes in the depths of the micropits. Huan et al. found that the applied voltage reached an equilibrium potential between electrochemical formation of titanium and the chemical dissolution of nickel at 30V. At higher applied potentials the nanotubes were less dense. At lower applied potentials, chemical dissolution dominated the titanium ion movement and nanotubes did

not form while the edges and peaks of the micropits were more strongly attacked, resulting in cracks forming from those areas under stress.[21]

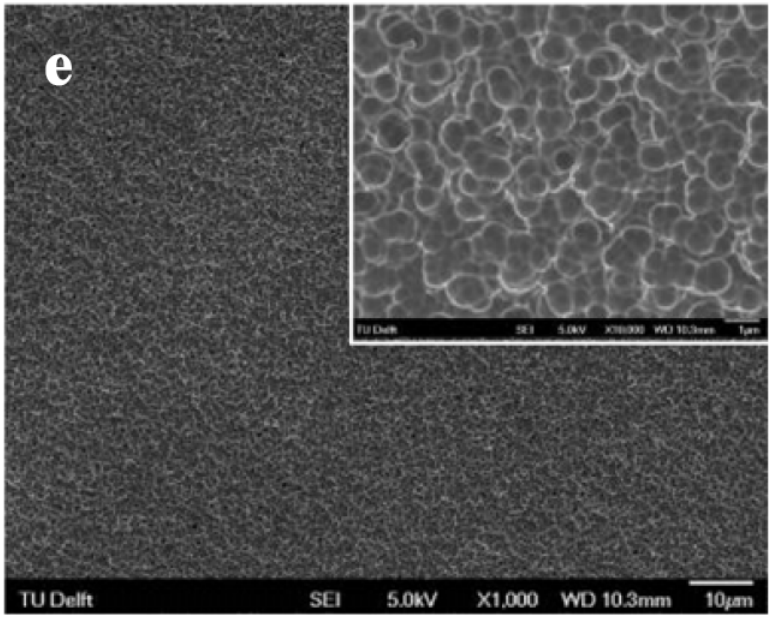

Figure 1.4: NiTi surface after electrochemical etching and nitric acid passivation with 65% HNO_3: methanol electrolyte with a volume ratio of 33:67. and 20% HNO3 acid at 80 °C for 20 min. [21]

1.3.4 Bioactivity of Nitinol

While the objective of polishing processes is usually increasing smoothness, several studies have shown links between surface microstructures, and cell proliferation and spread. Nitinol samples mechanically polished at room temperature (in the austenitic phase), which are subsequently electropolished in their martensitic phase develop a stepped surface profile shown in the SEM image in figure 1.6. This is attributed to the uniformity of shifting in crystalline planes within the alloy. The proliferation and adhesion of endothelial cells to grooved microstructures is reviewed by Shabalovskaya et al. Reportedly, the grooved microstructures can enhance migration of endothelial cells by up to 64.6% when compared to smooth control surfaces. The grooves cause the cells to elongate and align with the grooves. However, the growth rate of the cells was not investigated in this study[3].

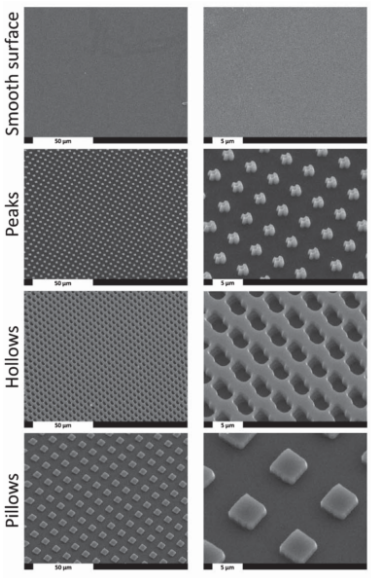

Figure 1.5: Surface microstructures tested by Lutter et al for endothelial cell adhesion and growth [22]

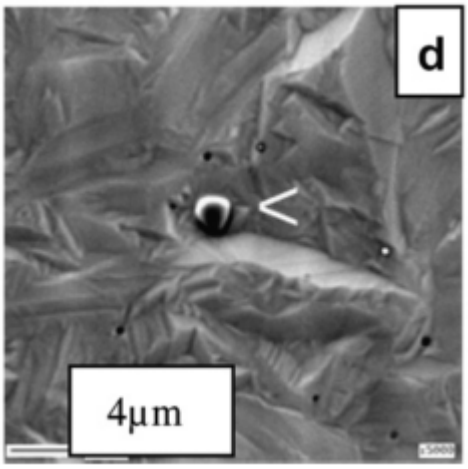

Figure 1.6: NiTi Sample electropolished in the martensite phase, carbide and oxide inclusions are visible [3]

Lutter et al. [22] performed a study of the effects of various microstructures on metallic surfaces. It was found that a pattern of 5x5 µm pillows spaced 5 µm apart and 1 µm high showed significantly higher endothelialization than the other two patterns tested and more than double the cell attachment and spread compared to that of smooth surfaces. The resulting platelet adhesion varied depending on static or flow conditions. Most notably, the platelet adhesion to the "peaks" microstructure shown in Figure 1.5 was higher than the others in static conditions but the lowest under flow conditions. The conclusion is that surface microstructures have the potential to increase the rate of endothelial cell attachment and growth. With the objective of reducing thrombogenicity to decrease the time after vascular stent implantation until the patients can be taken off dual-antiplatelet therapy[22]. The micro-strucures tested are pictured in figure 1.5.

1.4 Theory of Electropolishing

1.4.1 Fick's Law

The behaviour of particles that is commonly observed when a concentration gradient is present was first quantified by Adolf Fick in 1856 while working on problems in biophysics. He developed two simple laws by analogy with the flow of heat.[23]

$$\dot{V} = \frac{\Delta PAD}{x} \tag{1.2}$$

Where $\dot{V}$ is the rate the particles diffuse, ΔP is the pressure difference or the concentration difference at the source and the destination, A is the surface area, D is the diffusion constant, and x is the distance from the source. [24]

Rearranging this equation yields an expression for diffusion flux known as Fick's first law:

$$J(x) = D\frac{\partial C(x)}{\partial (x)} \tag{1.3}$$

Here $J(x)$ represents the flux of electroactive species in mol $s^{-1}cm^{-2}$ at the distance x, the fraction $\partial C(x)/\partial(x)$ is analogous to $\Delta P/x$ in equation 1.2 and it represents the concentration gradient at distance x, $C(x)$ is concentration at x.[25]

Fick's laws in simple English:

1. "The molar flux due to the diffusion is proportional to the concentration gradient".

2. "The rate of change of concentration at a point in space is proportional to the second derivative of concentration with space".[26]

These principles governing diffusion indicate the relationship between concentration gradient and mass transport by diffusion, with respect to the distance from the source of the diffusing particles. The general principle holds true for a remarkably large portion of observable particle interactions. Although, reality imposes a variety of additional factors on the diffusion that makes these formulae of limited use for practical applications. However, non-Fickian diffusion interactions appear when the diffusing particle's density is affected during diffusion by external factors.

1.4.2 Electric Double Layer

When an electrode in ionic solution is polarized, a layer of ions with opposite charge forms at its surface . These ions balance the charge of the electrode, and their density tapers off into the bulk solution. Helmholtz's original theory, which pertained only to the layers of ions closest to the electrode surface, describes that, on a positively charged plate, a layer of negatively charged ions would form at the surface. A second layer of positively charged ions would form beyond that to counteract the charge of the first layer of ions. The distance between the planes illustrated in Figure 1.7 as the inner and outer Helmholtz planes is in the order of a few tenths of a nanometer, while the electric field acting over this space is very high, in the range of $10^7 V/cm^{-1}$. [27] This effectively acts as the dielectric seperator found in conventional capacitors, forming a parallel plate capacitor made up of the electrode surface and charged particles in the electrolyte.[28] Helmholtz's model is an ideal model that considers the ion layers as static charges forming tightly packed layers. Several modifications have been proposed to more accurately describe reality.

The Gouy-Chapman-Stern theory, shown in Figure 1.7 separates the ionic interface between electric phases into a compact layer (which is approximately equivalent to the Helmholtz layers) and diffuse layer. In the compact layer, the electric potential

is a linear function of distance from the electrode, and in the diffuse layer potential change is exponential. The diffusion layer is orders of magnitude thicker than the diffuse layer and tapers off into the bulk solution, where the concentration of electroactive species at a distance is related to their diffusion coefficients. When varying the applied signal in electrochemistry, the diffuse layer forms concentration waves that propagate outward into the solution through the diffusion layer.[25] Stern joined the Helmholtz and Gouy-Chapman models into two regions of electric potential gradient. The Helmholtz (or compact layer) over which the potential drops linearly, and the diffuse layer, which consists of an exponential drop in potential with respect to distance from the electrode.[27]

The Fermi energy is the maximum energy level of any electron in a material at absolute zero. The Pauli exclusion principle means that no two electrons in an atom can occupy identical energy states, and they subsequently pack into the lowest available energy states. Therefore, all electrons in a solid are below a Fermi level with a statistically governed number of exceptions at temperatures above 0°K. Electrons that are in energy states below the Fermi level cannot take part in electrical conduction, because they cannot raise their energy levels due to the filling of all energy bands above them. Thus, their interactions are limited to the creation of ripples on the surface of the "Fermi sea".[29]An electrochemical reaction can be driven to favour reduction or oxidation by applying a voltage which represents the energy required to move a certain number of electrons. The application of a voltage or "electrochemical pressure" raises the Fermi energy by moving electrons from the valence band into the conduction band. The valence electrons are those which act to bind the atoms in a metallic lattice together thus raising their energy and removing them from the electrode favours oxidation of the metal releasing positively charged metallic ions.[25]

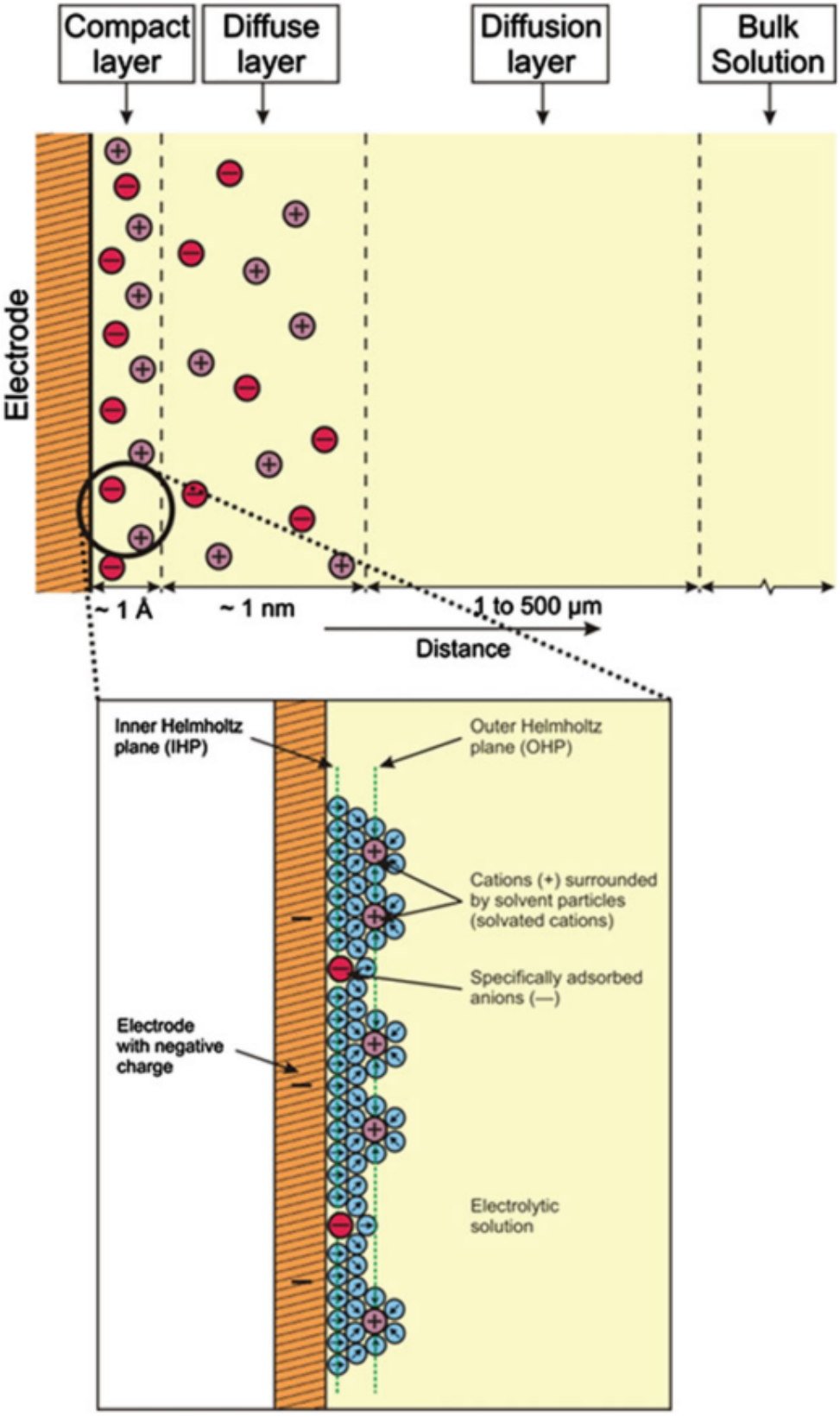

Figure 1.7: Ionic layers at electrode interface [25]

1.4.3 Surface Dissolution Simulation

Tailor [30] performed a numerical study modelling the formation of passive layers around a metallic anode during the electropolishing process, with the objective of revealing the effect of mass and momentum transport on the formation of the passive layer. The variables considered are electrolyte inlet flow velocity, co-efficient of diffusion of an electrolyte, the electrode spacing, and the initial surface roughness of the anode. Temperature is considered constant. Their study utilizes 2 dimensional electrodes 60mm×1mm inside a 150mm ×150mm electrolyte enclosure. This is not a practical system in reality, due to the anode and cathode being the same size. However, the authors neglected hydrogen bubble evolution and the effect of electron charge transfer limits, which minimizes the impact of an undersized cathode. A laminar flow of electrolyte is considered and combined with a convection-diffusion model. The primary and secondary processes being modeled here are represented by:

$$M \rightarrow M^{n+} + ne^{-} \tag{1.4}$$

$$nH_2O + ne^{-} \rightarrow \frac{n}{2}H_2 + nOH^{-} \tag{1.5}$$

$$M^{+n} + nOH^{-} \rightarrow M\left(OH\right)_n \tag{1.6}$$

$$M + nH_2O \rightarrow M(OH)_n + \frac{n}{2}H_2 \tag{1.7}$$

Equation 1.4 represents the anode surface metal dissolution, 1.5 is the tool surface (cathode), 1.6 is metal hydroxide diffusion from the work piece surface into the bulk electrolyte, 1.7 is the net process reaction. M represents the the metal and n is the valency of the metal.

The target of the variable manipulation is the speedy formation of a uniform passive layer, which can be said to promote polishing due to the preferential dissolution of peaks mechanism. The study concludes that electrolyte flow, diffusion coefficients and electrode spacing are the primary variables that affect the formation time of a stable passive layer. The time to obtain the passive layer was found to increase with short electrode spacing, but stabilized with greater gaps. Thus, the combination of higher inlet velocity, a medium diffusion coefficient and relatively larger electrode spacing yields the fastest formation of a stable passive layer.[30]

Several authors have suggested that there are three forms of diffusion layer that occur during anodic dissolution. The first occurs when a potential is applied to a cell at equilibrium and a diffusion layer starts to form. At this stage the diffusion layer is very thin and conforms to the surface features, providing uniform material removal rate. As the dissolution continues, the diffusion layer gets thicker and a larger concentration difference is found between protrusions and valleys on the surface, as seen in Figure 1.8 (a). The higher concentration difference results in the protrusions experiencing a higher rate of dissolution. If a diffusion or reaction rate limit is not imposed at this stage, the diffusion layer continues to thicken, eventually leading to a situation shown in Figure 1.8 (b). The concentration gradient near the surface is

not great enough to produce a significant difference in the dissolution rate of the peaks and valleys. Taylor et al. ignore the initial, very short duration, phase of thin diffusion layer and classified the effect as a macroprofile and a microprofile.[31] Teixeira performed the simulations shown in Figure 1.8 using a spherical diffusion model in Comsol Multiphysics.[32]

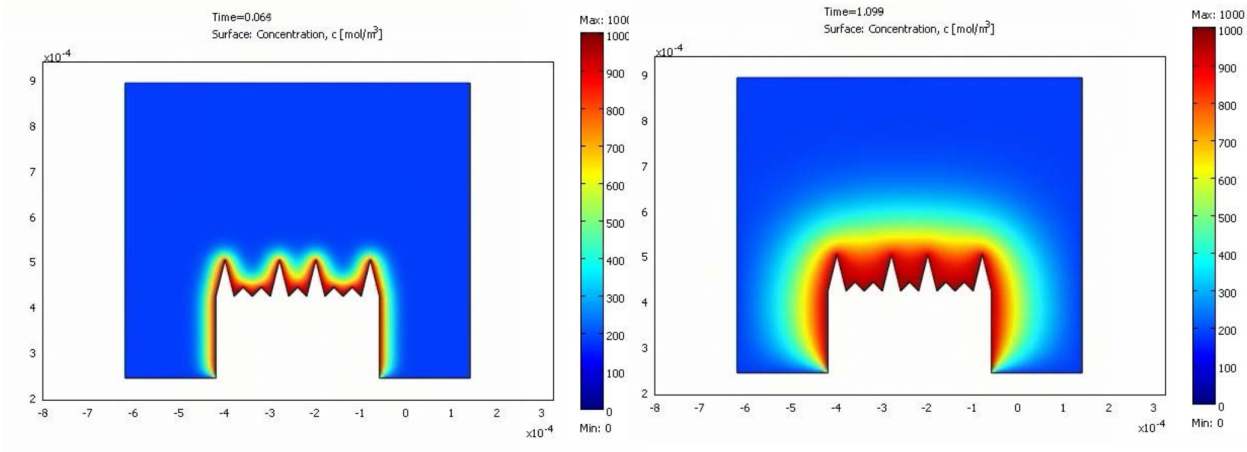

(a) (b)

Figure 1.8: 2D Simulation of concentration gradients at two time intervals. [32]

1.5 Electropolishing Techniques

1.5.1 Alternating Pulses

With conventional electropolishing processes, when electropolishing metals that passivate easily, it is necessary to make use of powerful acids to break through the passivated film that forms on the anode. There is an alternative, however. The passivated layer can be re-activated by briefly reversing the electric potential on the electrodes. Combining these reverse pulses with carefully tuned forward pulses has been shown to work on niobium and Nitinol using an aqueous electrolyte composed of 30 wt% sulfuric acid. When careful process control is implemented, in conjunction with strategic off times to facilitate cooling and electrolyte flow, it is possible to obtain surface roughness characteristics comparable and even smoother than those produced by more acidic electrolytes and a direct current (DC). Inman and Taylor provide guidelines for tuning the pulse widths in the form of mathematical relationships between diffusion layer thickness and pulse times [11]

$$\delta_p = 2((D \bullet t_p)/\pi)^{1/2} \tag{1.8}$$

In equation 1.8, δ_p is the thickness of the diffusion layer formed by each pulse, D is the diffusion co-efficient and t_p is the duration of the anodic (forward) pulse.

The limiting current density above which the polishing effect breaks down is also higher in this pulse polishing paradigm. The ratio between the steady state (DC)

mass transport limited current (i_{lim}) and the limiting current during short anodic pulses (i_p) is:

$$\frac{i_P}{i_{lim}} = [\delta_P/\delta\,(1-\gamma_a)+\gamma_a]^{-1} \tag{1.9}$$

Here $\gamma_a$is the anodic duty cycle and δ is the diffusion layer thickness for a given DC limiting current i_{lim} that corresponds to the same system being pulsed at anodic pulse maximum current i_P. [33] A typical pulsed waveform including forward and reverse pulses with strategic off times is shown in Figure 1.9. The polarization potential of the cathodic reverse pulses given in Figure 1.9 by V_c, is hypothesized to be dependant on the free energy of the material that requires depassivation by Taylor et al. They admit that the mechanism of depassivation is not fully understood. Others have shown the effectiveness of pulsatile DC current on reducing the grain size during electrodeposition of copper, gold and nickel.[34]

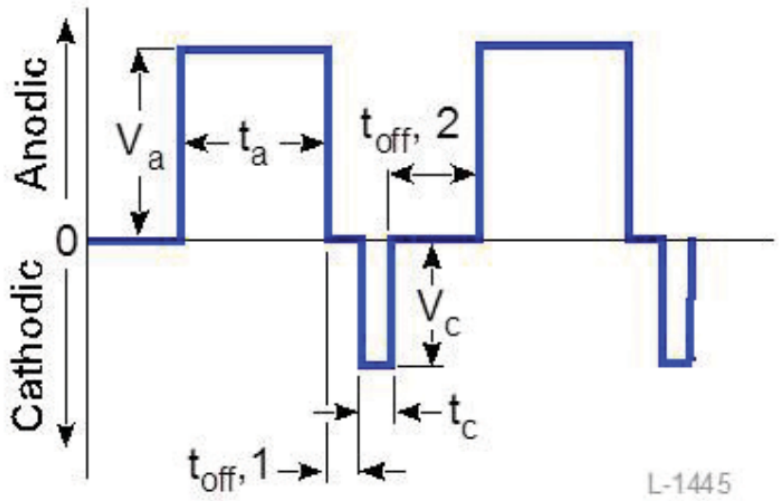

Figure 1.9: Pulsed Electropolishing Waveform [33]

Another study using pulsed control and an aqueous electrolyte on a stainless steel workpiece was performed by Kim and Park. Their electrolyte was composed of 2.4 mol/L H_2SO_4 and 5.9 mol/L H_3PO_4in distilled water. An electrolyte that was itself drawn from a study by Chen et al.[35] Kim et al. found that while pulse polishing produced good surface roughness improvement and oxide layer formation, there was still a profusion of micro-pits which acted as corrosion initiation points during a test in 0.05989 mol/L NaCl (synthetic seawater). This study was performed using anodic pulses only and an optimum pulse width of 0.8 ms was selected, with shorter pulse widths of 0.1 ms creating more micro-pits and longer pulse widths, up to 2.2 ms, producing higher surface roughness.[36] While the aqueous nature of this

electrolyte is advantageous from a cost and maintenance perspective, they still make use of phosphoric acid to assist with passive layer breakdown in order for polishing to proceed.

1.5.2 Plasma Electrolytic Polishing

Taking the general principle of electropolishing one step further, and using a higher voltage to perform the anodic dissolution by the formation of a layer of plasma around the part, provides several advantages. Plasma electrolytic polishing (PeP) can achieve surface roughness smoothing down to less than 0.02 µm. However, it cannot be used as a stand-alone process for smoothing very rough surfaces with large burrs, because it will result in extreme rounding of edges and reduction in part accuracy over long periods. A typical PeP process is set up with a cathode to anode surface area ratio greater than 10:1. Usually the cathode will form a ring around the part. The cell is polarized to between 180-300V with a current density of 0.2 A/cm^2. The aqueous electrolyte conductivity should be adjusted to be between 4 and 30 S/m through the use of less than 12% addition of salts. The electrode surface area ratio is necessary to create the current density required for plasma formation at the anode. The applied potential and current density must be tuned to induce the formation of an electro-hydrodynamic plasma skin that envelops the part. Under these conditions, several processes take place that result in polishing; ionization of the steam layer, dissolution of the metal peaks that protrude through the plasma layer into the water, anodic oxidation and hydrogen evolution[37]. One theory on the mechanism of preferential dissolution is known as the streamer theory, which postulates that plasma discharges bridge the steam ion layer to the asperities resulting in preferential dissolution.[38]

1.5.3 Direct Current

By far the most commonly applied electropolishing technique applies a direct current anodic potential to the workpiece. The widely accepted theory for the mechanism through which electropolishing is achieved is a viscous salt film model. First described by Jacquet et al. in relation to copper electropolishing, they presented the voltage-current relationship in Figure 1.10. The graph indicates a current plateau in which a stable, uniform thickness salt film adheres to the metal surface and promotes preferential dissolution of asperities that project further through the layer towards the solution bulk.[39] In the plateau region with a stable metallic salt film present, mass transport is limited by the electrolyte interaction with the metallic and ionic species and the associated reaction and diffusion rates.[40]

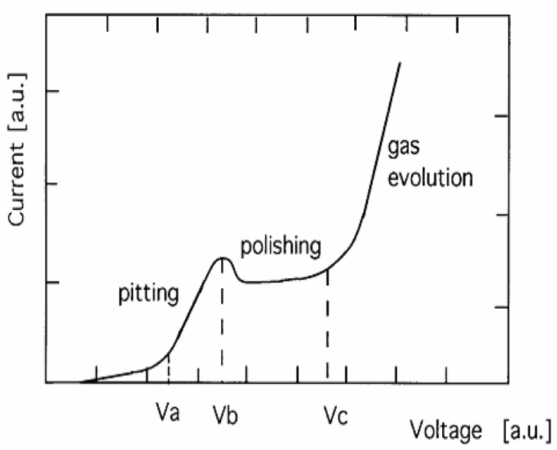

Figure 1.10: DC current plateou

1.5.4 Electrolyte Agitation

A study on Stainless Steel electropolishing was performed utilizing DC and pulsed DC (no reverse pulse) at a low frequency (50Hz). The authors found it difficult to eliminate pitting, which they attributed to gas bubble formation. To mitigate the bubble formation, they attempted mechanical and ultrasonic agitation of the electrolyte, which resulted in reduced pitting. Using DC pulses and varying the frequency led to an observation that surface roughness increased at higher frequencies. Since DC electropolishing is dependant on the formation of a viscous salt layer above which peaks are removed, it was hypothesized that shorter pulses did not provide sufficient time for the salt layer to form and thicken enough to promote electropolishing. Agitation resulted in greater material removal rate. Above a certain limit, the electrolyte motion disrupts the salt layer after which the surface roughness increases again. It was found that the local minima shown in figure 1.11 exist at certain magnetic stirrer speeds which resulted in the best surface finish. These tests were performed with current density between 310-320 mA/cm^{2}and temperature of 65-70 °C.[41] [42]These results illuminate the dynamic between electrolyte motion and the salt film model of electropolishing. It is possible that a similar trend exists utilizing high frequency pulse and reverse waveforms at higher current densities in place of a viscous salt film (this has not been studied in literature).

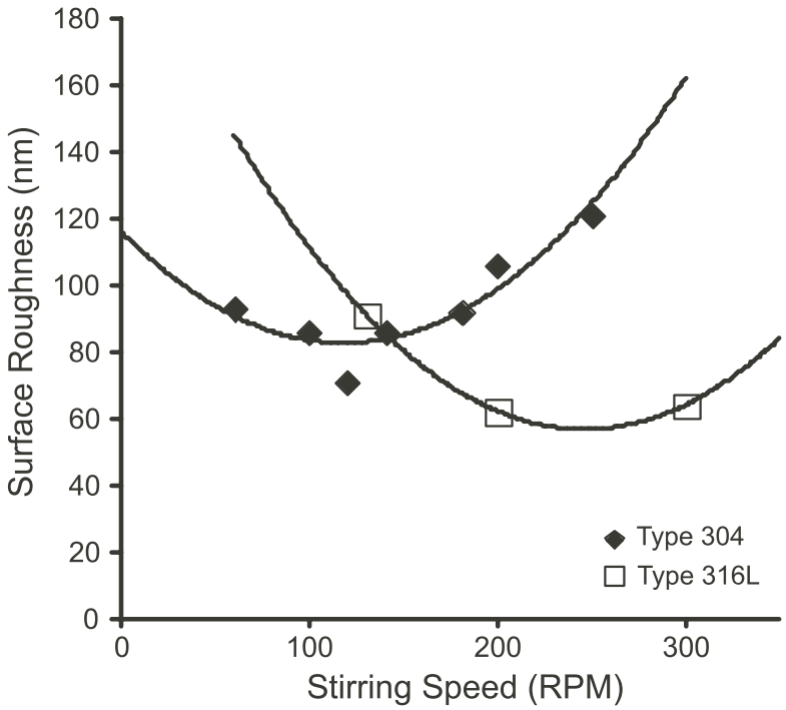

Figure 1.11: Local minima in surface roughness of Stainless Steel at varying stirrer speed [41]

1.5.5 Control Algorithms

There are a large number of parameters that control the electropolishing process. Some of them are difficult to measure and others vary as the process proceeds. This makes it difficult to make a general-purpose control algorithm without human intervention. To compensate for the uncertainty of the system, Surmann et al. constructed a fuzzy logic controller which considers all of the input parameters simultaneously, before deciding what to modify. Their work is focussed on polishing Cobalt chromium dental casts, and they identified several parameter dependencies which are programmed into their fuzzy logic controller.[43]

- Relative motion of the anode and the electrolyte assists with heat removal and electrolyte reactive species replenishment.
- Electrolyte deterioration as polishing cycles increase. More metal ions are dissolved in the electrolyte which results in an increase in electrolyte resistance which affects current density and polishing time requirements. Different temperature settings can also effect a positive change to counteract electrolyte age.
- The number of anode pieces to be polished has a non linear effect on the current density requirements. Thus, the electrode spacing must be modified to compensate.

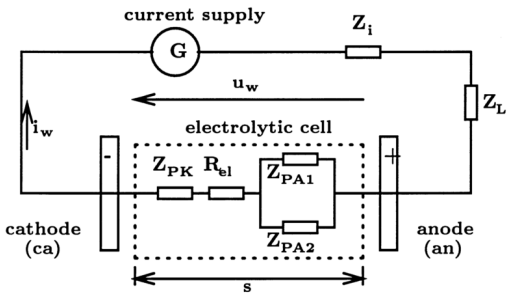

Figure 1.12: Electrolytic cell equivalent circuit [43]

Surman et al. created an equivalent electrical circuit of a typical polishing cell shown in figure 1.12. Here the impedance of the cell Z_w is comprised of the polarization resistance of the cathode and anode Z_{PK} and Z_{PA} respectively (Z_{PA} is split into parallel elements to simulate multiple anodes often found in industrial processes). R_{el} represents the electrolyte resistance. G is a current source with its internal complex impedance Z_i and $Z_L$is the wire and electrode contact resistance.

1.6 Measurement Techniques

1.6.1 Atomic Force Microscopy

AFM imaging utilizes a tip on the end of a cantilever which scans across the sample. Depending on the interaction mode of the tip, different information can be gathered. It is thus suitable for a variety of applications and sample types. Because the deflection of the tip can be measured in the z-axis, it is suitable for surface roughness analysis. Another operation mode is to measure the lateral force which yields information about the friction co-efficient of the materials being scanned. Equipping the scanning tip with a magnetic module allows mapping of the magnetic phase of the material.[44] AFM has the highest resolution of existing imaging techniques, with Angstrom level resolution. The performance of an AFM system is limited by the quality of the cantilever tip. The deflection of the tip is typically measured optically through reflected light phase difference measurement. Thus, calibration is dependent entirely on the cantilever and tip performing as expected.[45]

1.6.2 Confocal Microscopy

A confocal microscope combines two mechanisms to create a 3D scan by rejecting out of focus light, and only accepting light from a single point or pixel, which corresponds to the focal point of the lenses that make up the microscope. Scanning this point across the surface and adjusting the focal point in the vertical direction yields slices of data that can be built into a 3D model. The resolution is limited by optical scattering, which results in a minimum resolution on most commercial confocal microscopes around 200 nm in the XY plane and 500 nm in the Z direction.[46] Some modern

confocal optical microscopes can achieve resolutions as low as 20-50 nm in XY and 50 nm in Z.[47] The issue of resolution is somewhat convoluted, because the accuracy of the laser-sample interaction position can be higher than the resolution dictated by total spot size, and the intensity data can be gathered in a continuous manner rather than as discrete points.[48]

1.6.3 Scanning Electron Microscope Surface Analysis

Bannerjee et al. used the standard deviation of Pixel intensity to measure the surface roughness of paper.[49] The rationale for using standard deviation in this case was based on the observation that a plot of the pixel counts was in the form of a symmetrical bell curve.

Scanning Electron Microscope analysis of 3D topography is an active area of research. Recent advances enabled by leaps in computation power and machine learning, have resulted in commercial software packages which can use images captured at various eucentric tilt angles to reconstruct a 3D model of the sample. However, most software reconstruction methods require significant surface features that can be identified and subsequently correlated to align the images taken at different tilt angles. [50]

One group investigated the relationship between pixel brightness or grey-scale level in SEM images of paper. The number of electrons that escape from recesses is lower than the amount produced by peaks or flat areas, because some electrons are reabsorbed by the material above the recess. This means that flatter surfaces produce SEM images with a more uniform brightness level. They acquired images with the beam positioned perpendicular to the surface of interest. The paper samples were sputter coated with gold and the Hitachi S800 SEM was operated with an acceleration voltage of 12 kV. They found that a histogram displaying pixel brightness versus pixel count produced a generally symmetric bell curve shape. Thus the standard deviation was identified as an effective index of surface uniformity. The correlation was confirmed by visual identification of the same micrographs and the SEM roughness index obtained from the standard deviation of pixel brightness.[49]

1.6.4 Potentiostat

Potentiostats perform complex electronic control and measurement on electrochemical cells, making use of multiple electrodes immersed in the electrolyte to accurately measure the reaction at an electrode surface. A potentiostat is indispensable for any electrochemical research. Unfortunately their high cost makes them relatively inaccessible and non-viable on industrial scales, with high current versions (20A) costing over R300k. (source: confidential quotations obtained from industry leading potentiostat manufacturers). Some progress has been made in open source designs such as Dstat and CheapStat that can be made for a few thousand rand. However, they cannot yet rival the capabilities of commercial solutions.[51, 52]

Reference Electrodes

Reference electrodes for electrochemical measurements commonly use nanoporous glass frit to maintain a salt bridge between the electrode filling solution and the electrolyte under test. Mousavi et al. concluded that larger pore size resulted in lower electrode drift at the cost of high leakage of reference electrode filling solution, which can result in contamination of the sample. This effect is ascribed to the influence of the Debye length on ion screening as the pore size varies. Therefore, they recommend using pore nanoporous frits with pore size that matches the ionic strength of the solution under test (smaller pores can be used for higher ionic strength solutions, but larger pores must be used for weakly ionic solutions, otherwise there can be a drift in electrode potential as high as 100mV). The ideal porous frit should be made of a material without ionic surface groups. However such a material has not yet been fabricated in a nanoporous format with sufficient hydrophilicity. [53]

Luggin Capillaries

Luggin capillaries are used to bring the reference electrode closer to the surface by creating a capillary connecting the reference electrode's porous junction to the electrolyte, close to the working electrode surface. A small diameter luggin capillary can negatively impact the reference electrode's response time due to the resistance of the electrolyte in the capillary. Using a larger diameter capillary can mitigate this effect. [54] However, care must be taken to ensure the tip is maintained at a distance of at least 2x the tip diameter to avoid ionic screening of the working electrode surface.

Chapter 2

Research Proposal

2.1 Research Objectives

- Describe the process of cyclic bi-directional polarization.
- Identify the transition stages between dominant electrochemical equilibrium states of Nitinol, in an aqueous electrolyte on very short time scales (<10 ms).
- Find the ratio between chemical reactions that need to be balanced to achieve a minimum energy (flat) surface.

2.2 Experimental Objectives

- A rapidly alternating control signal will be used to control the surface environment around a metal during electrolytic dissolution.
- The waveform parameters need to be optimized to produce a minimum surface area.
- A method for identifying the parameter set that will yield surface roughness reduction on a complex stent geometry will be determined.
- Surface characteristics will be examined using atomic force and electron beam microscopy. The imaging and processing parameters that provide a good representation of the surface roughness will be identified.
- Often the passivation or smoothing is assisted by additional chemical steps that are not part of the electrochemical dissolution process (e.g. thermal oxidation or diamond slurry polishing). One of the aims of this research is to combine them into one step with a sequence of electrical control parameters.

2.3 Process Flow Diagram

The raw material is received in the form of a tube with a ground outer surface and an oxidic inner surface. The tube is then exposed to the processing steps outlined in Figure 2.1, and described below.

1. Laser cutting is done on a Rofin Starcut fibre laser cutter that is used for stent cutting.

2. Mechanical cleaning is done on the inner faces of the tube after laser cutting to remove molten material and cutting swarf which is blown inwards by pressurized argon gas during the cutting process. This process involves heat shrink applied to the outside and an abrasive rod or wire brush passed through the inside.

3. De-scaling is achieved with immersion in tetra butyl ammonium hydroxide which is intended to aid in removal of organometallic compounds.

4. The Nitinol is heat-treated in a Techne SBL-2D fluidised bath at a temperature of 500 °C. The thermal treatment was used to shape-set the stent to a larger, 5mm inner diameter (originally 3.886 mm). This process also raises the upper phase transition temperature by a rate around 1 °C / minute. The raw material is supplied with a wide tolerance on the upper phase transition temperature usually as 0-10 °C. Therefore it is necessary to determine this limit after the thermal shape and phase setting step.

5. An industry standard process documented in ASTM B600-11 was used for removing surface impurites and dissolving oxide layers in titanium alloy surfaces. This is necessary to remove the thick oxide and non-binary nickel-titanium layers formed during laser cutting and thermal treatment.

6. Finally, electropolishing was applied immediately, to smooth the surface and create a stable uniform passive layer of titanium oxides.

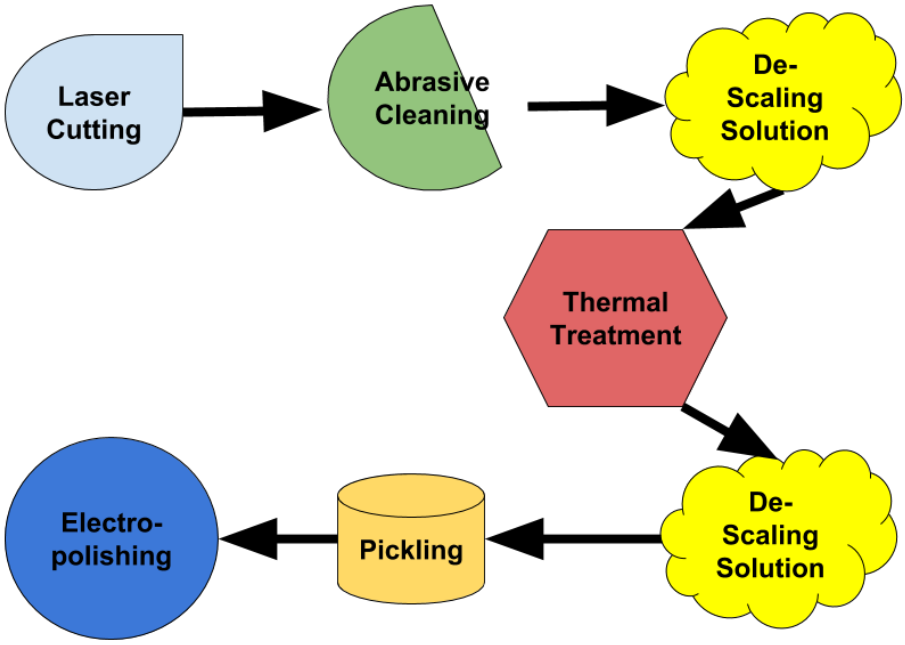

Figure 2.1: Nitinol stent processing flow diagram

Chapter 3

Materials and Methods

It is difficult to convert an interconnected web of information (the real world) into a serial format. The reader, must de-convolute this result and attempt to recreate the original. To aid you with this process Figure 3.1 was created to help piece together the puzzle by providing an overview of the thesis in a non-linear layout which displays the linkages between sequentially separate methods and conclusions which were previously connected in time and space.

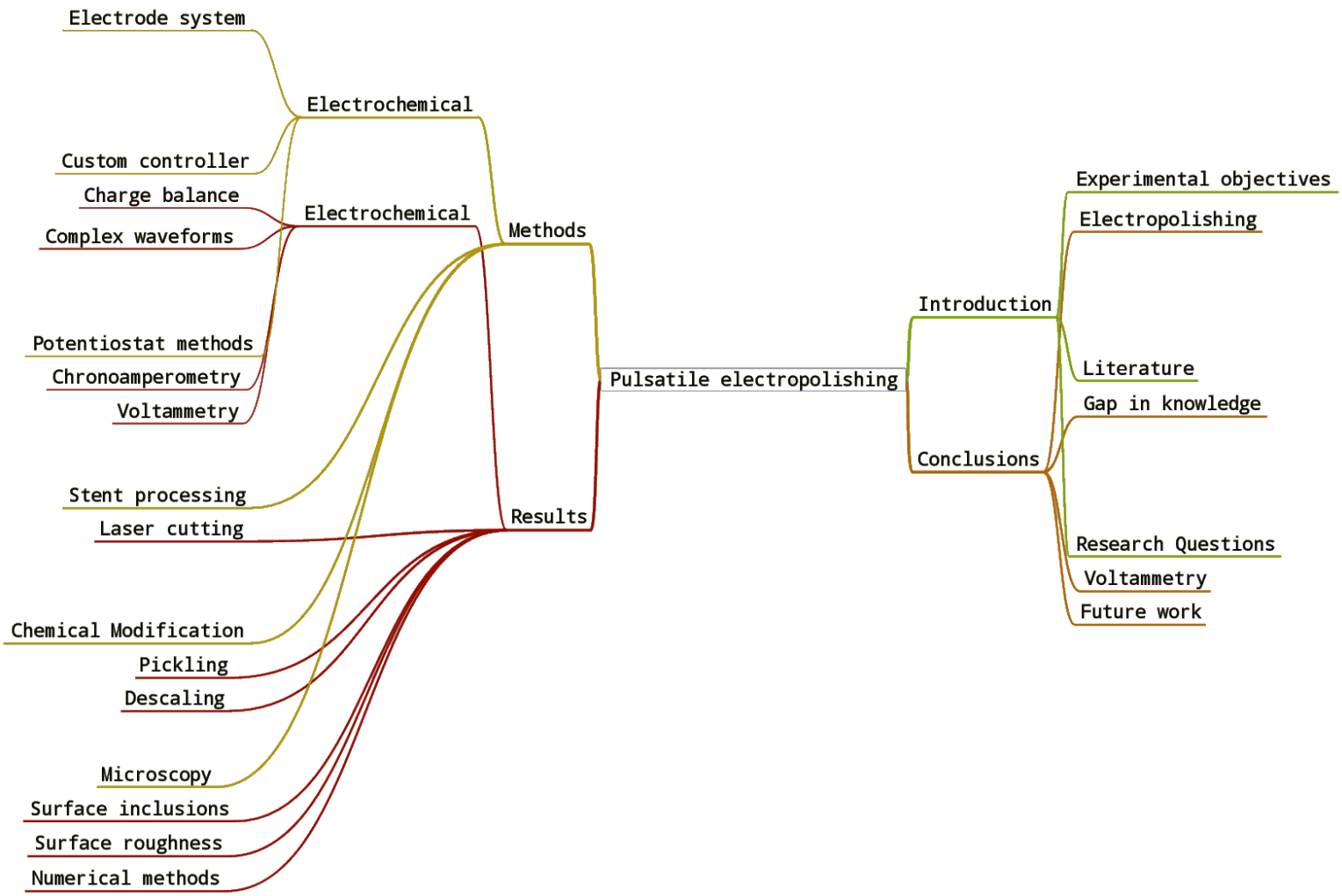

Figure 3.1: Connecting the dots: A non-linear layout displaying the linkages between sequentially separate methods and conclusions which were previously connected in time and space.

3.1 Stent Processing

Due to the multistage nature of the stent processing flow, it is necessary to pay careful attention to all the conditions the material is exposed to prior to electropolishing, for two reasons:

1. Isolate the effects of changes to the electropolishing stage from the processing.
2. Ensure the final stent is biocompatible.

Data on experiments was recorded on a tablet with a stylus that backed up the notebooks to the cloud. Information on preprocessing of individual samples was stored in a google sheet, also a cloud based software, to eliminate the risk of data loss.

Table 3.1: Stent processing steps

Process	Details	Data
Laser Cut	Raw tube is cut on rofin laser cutter	laser cutter parameters, tube dimensions, cut pattern
Cutting swarf removal	Abrasion of stent inner diameter	method
Storage		Sample number, medium
Wash	solvent, distilled H_2O	Method, solution
Scale removal	Immersion in tetrabutyl ammonium hydroxide	Duration, temperature, volume of solution, solution molarity, SEM image
Wash	solvent, distilled H_2O	Method, solution
Thermal treatment	Shape setting at temperatures around ~500 °C	duration, diameter, temperature
Wash	solvent, distilled H_2O	Method, solution
Oxide removal (pickling stage)	immersion in solution of HNO_3/ HF	solution, duration, temperature
Wash	solvent, distilled H_2O	Method, solution
Storage	(this step should be avoided if possible)	medium, duration
Electrolytic modification	The process under study.	All electrical, mechanical and chemical properties of the reaction.

3.1.1 Washing

A standard washing process was applied before and after every processing stage. Agitation was accomplished using a contact shaker on low intensity with the sample immersed in 30-40ml of solution inside a standard 50ml polypropylene centrifuge tube.

- Reverse osmosis Millipore water was used to wash the samples with agitation for at least 2 minutes.
- Acetone immersion with agitation and drying at 60-75 °C for 60 seconds.

3.1.2 Raw Material

The raw material chosen as a substrate for this project is Nitinol SE508, a superelastic variant that is 55.8 wt% nickel, <0.07 wt% carbon and oxygen with the balance made up of titanium. It was selected because the manufacturer (Nitinol devices and components) claims it is the world's most implanted Nitinol material in their data sheet.[55] The tubing is supplied with a ground outer surface and an oxidic inner surface. The ground outer surface presents a surface structure made up of circumferential grooves. The tubing used had an OD of 4.394mm and wall thickness of 0.254mm

3.1.3 Laser Cutting Tubular Nitinol

The first stage in the processing is laser cutting to form the stent geometry. This was performed using Rofin Starcut Fibre Laser tube cutter and the design in Figure 3.2. Cutting Nitinol requires an inert gas (argon) be used to eject the molten material to prevent oxidation and excess heat generation. Due to the heat sensitivity of Nitinol and the high melting point, a secondary coolant (water) is pumped through the tube ID.

Some optimization was performed on the cutting parameters, and better laser parameters for the Rofin Starcut Fibre laser were identified to improve 4 factors:

1. The heat affected zone (HAZ)
2. The amount of remelted material left on the cut face.
3. The quantity of remelted material attached to the inside cut edge.
4. Frame deformation during cutting.

Based on the knowledge that femtosecond laser pulses produce better results when used to cut Nitinol[56, 57], the pulse duration was decreased while increasing the frequency. This caused a greater amount of energy to be delivered per cut length, creating a greater heat affected zone. Thus the cutting travel speed was increased to balance the change in instantaneous power. Optimization was performed by setting the frequency to its maximum value and then adjusting the pulse width and cutting

speed incrementally until the cut did not travel all the way through the tube. Increasing the pulse width slightly would then cause it to cut through with the minimum instantaneous energy delivery possible. Optimization was stopped when a clean cut that travelled all the way through the tube wall with a minimum of melted Nitinol on the inner surface was achieved.

The stent design shown in Figure 3.2 was composed in a computer aided design program (SolidWorks) to contain elements similar to those found in a variety of similar Nitinol medical devices. The design was tweaked to provide a $3cm^2$ surface area when immersed to a specific point to permit easy calculation of current density.

3.1.4 Stent Design

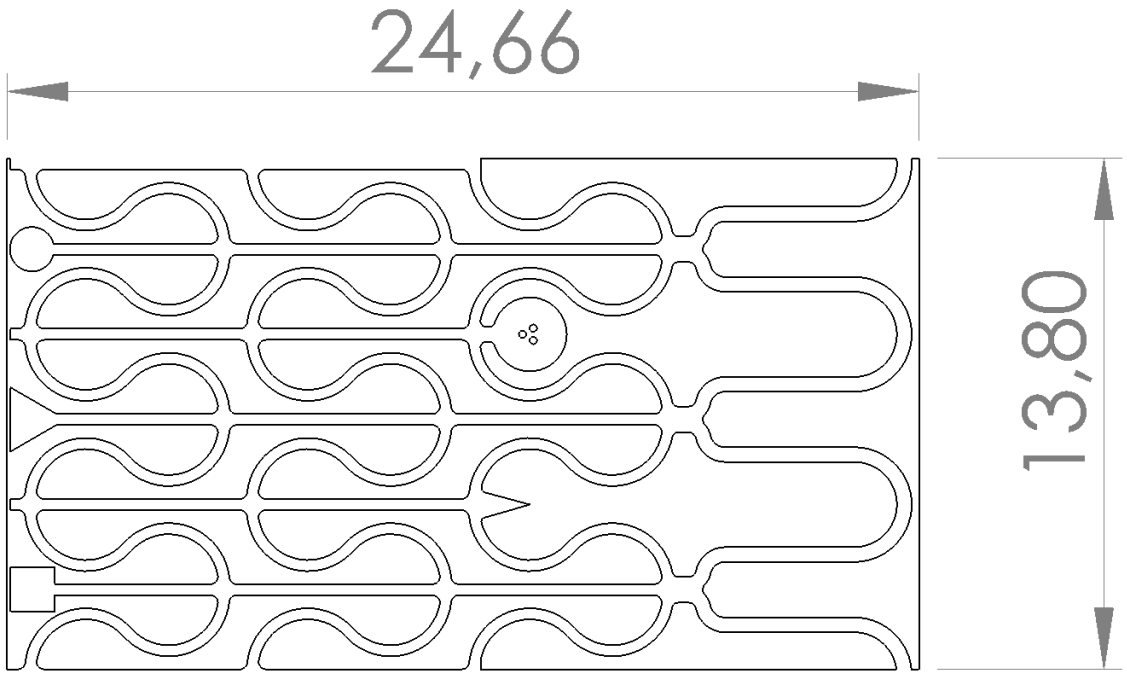

Figure 3.2: Stent design 2D drawing used for laser cutting

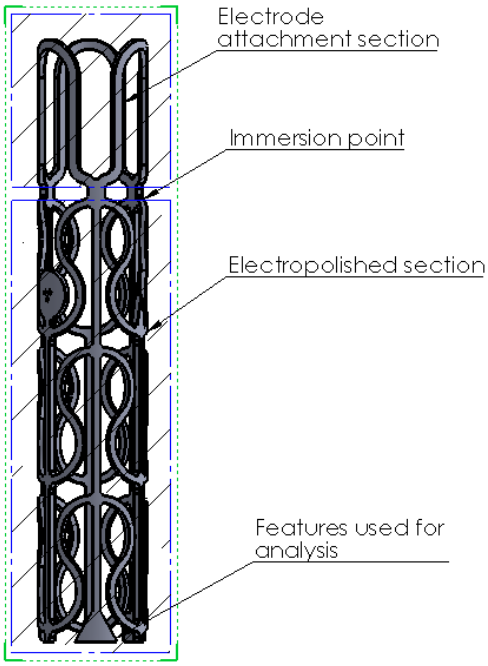

Figure 3.3: Stent design 3D model with labels

3.1.5 Thermal Treatment

Thermal treatment is often performed on Nitinol devices to remove residual stress from processing, shape set them into specific geometries, or adjust the phase transition temperature. A simulated thermal treatment was performed on every sample by shape setting it to a slightly larger diameter (5mm ID) for 4 minutes at 500 °C with 1.5bar of air pressure fluidising the sand in a Techne SBL-2D Fluidised bath. The sample was then quenched in distilled water at 25 °C. 4 minutes was found to be the minimum immersion time after which there was no recoil towards the original diameter afterwards. The fluidised medium was UG1 activated alumina (aluminium oxide), and the process gas was compressed air. The stent was placed onto a 5mm stainless steel tube (raising the ID to 5mm) before thermal treatment to ensure rapid and even heating from the inner and outer surface (original tube ID = 3.886mm).

3.1.6 De-Scaling Solution

Scale, is deposits or flakes of metal salts or organometallic compounds in the surface, usually following production processes. In this case the scale was made up of carbon compounds which impede electropolishing.

A solution of 0.25 M tetrabutyl ammonium hydroxide (TBAOH) was used. The TBAOH was created by combining 0.5 M tetrabutyl ammonium bromide (80.59g in 500ml water) and 0.5M sodium hydroxide (10g in 500ml water), producing an approximately 0.25 M TBAOH solution containing sodium bromide as a byproduct. This solution is intended to break carbon bonds and assist in scale removal. The

descaling process used was immersion for 2 hours at 50 °C with agitation from a magnetic stirring element and the stents suspended on stainless steel wire in the solution. A Heidolph magnetic stirrer-hotplate was used with a temperature probe placed in the solution. When descaling was applied, it was performed before and after thermal treatment for a total of 4 hours of immersion.

3.1.7 Oxide Removal (Pickling)

An ASTM standard for oxide removal on titanium and its alloys is present, which recommends a final cleaning solution composed of nitric and hydrofluoric acid in the ratio 8:1 (when 48% HF and 70% NO_3 is used). The standard recommends a temperature of 49 °C, but gives no indication of immersion duration.[58]

A contact shaker was used and 20ml of pickling solution was placed in a polypropylene container, the stent was added and the lid replaced followed by 45 seconds of agitation on the shaker after which the stent was immediately removed and placed in distilled water. The agitation reduced the mass loss rate compared to stents pickled with no agitation permitting greater control of total mass loss. Unfortunately, agitation requires additional handling and further equipment contact with this extremely hazardous solution. Further efforts in this direction were discontinued in favour of developing an electropolishing process that did not require the TiO_2 starting layer be removed with HF. Due to the highly toxic nature of HF, the following safety precautions were taken:

- Acid resistant pants and jacket were placed over ordinary clothing.
- A polypropylene apron was worn over the acid resistant clothing.
- Polypropylene gloves were worn over nitrile rubber gloves.
- A respirator and safety glasses were worn under a polycarbonate face shield.
- The HF was handled inside a fully polypropylene fume hood equipped with water filtration system.
- The HF was stored in polypropylene vessels which where placed into polypropylene bags and then a metal tin.

3.2 The Electropolishing Reaction System

With the primary objective of increasing the uniformity of the reaction a cylindrical vessel was chosen to conduct the experiments. Since the stents to be polished at this stage were all cylindrical meshes. It was decided to construct a vessel that can be sealed to prevent condensation or other atmospheric conditions interfering with the electrolyte composition. The vessel must provide a means to cool the electrolyte to 5 °C. Therefore, a cooling jacket or electrolyte thermal exchanger must be used. We will refer to the stent which is being electropolished as the working electrode or WE to conform with electrochemical conventions.

3.2.1 Electrolyte

The electrolyte was prepared by mixing 456.5ml of concentrated H_2SO_4 with 1963.5 ml of distilled water. This produces 2420ml of aqueous $H_2SO_4$with a molarity of 3.54 (33 wt. %).

This electrolyte was chosen because of its high conductivity which is shown in Figure 3.4. An electrolyte with high conductivity is desirable to emphasize the impact of electrical control parameters, instead of passing control of the surface layer thickness and formation time variables to electrolyte viscosity and resistance. Aqueous sulphuric acid is a well understood and documented electrolyte, and was also the electrolyte of choice in the other alternating current pulsatile electropolishing method published by Faraday Technologies.[11, 31, 33]

3.2.2 Working Electrode

The working electrode (WE) is the laser cut Nitinol stent. A simple mounting method was devised that allows easy and secure stent removal and replacement with a pressure-based electrical contact that remains outside of the solution during electropolishing. This was achieved by placing the stent a short way onto a 6mm titanium rod and placing a Teflon ring over it, which applied compression onto the rod (the stent ID is 5mm at this stage). The working electrode, counter electrode and reference electrode were held in position by 3D printed components. An exploded view of the electrode assembly is shown in figure 3.5.

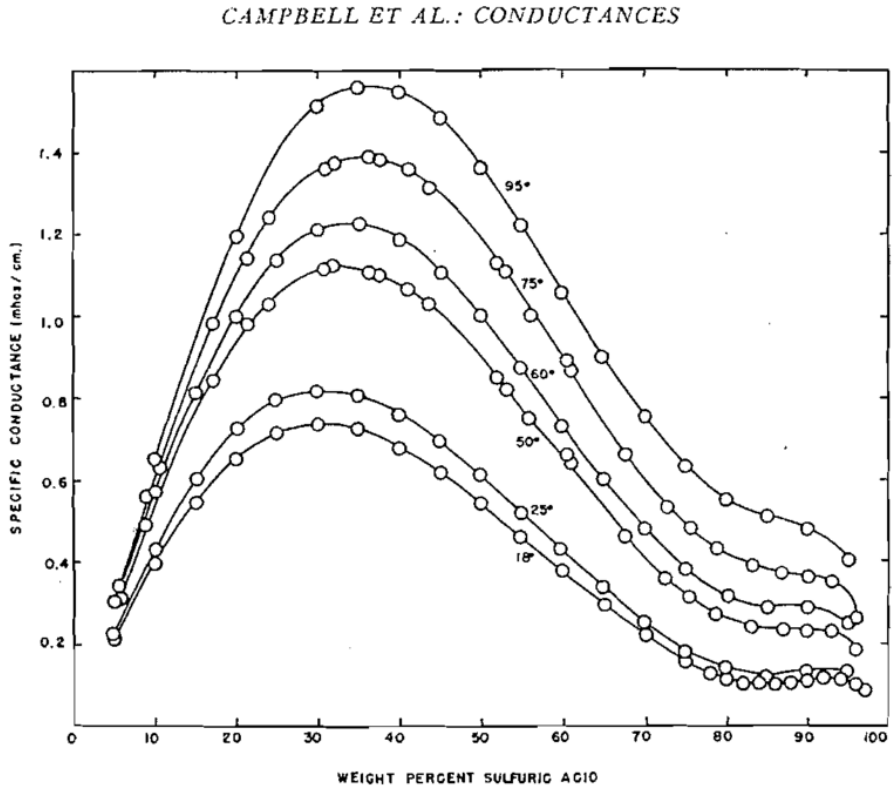

Figure 3.4: Aqueous Sulphuric Acid conductivity. [59]

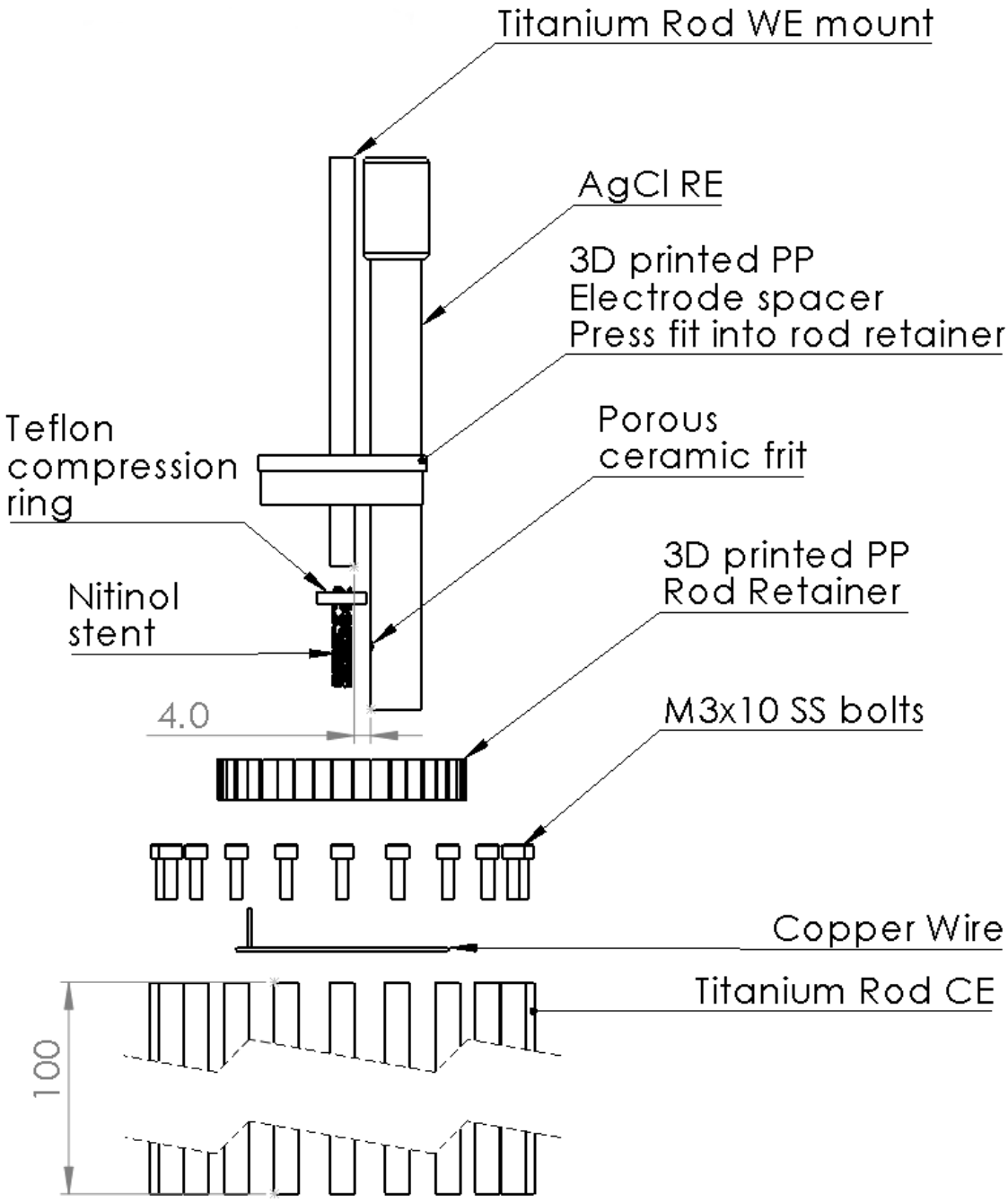

Figure 3.5: Exploded view of electrode components (all dimensions in mm)

3.2.3 Reference Electrode

The electrode used to measure the potential drop between the metal surface and the bulk electrolyte solution must not react with the electrolyte, to ensure an accurate measurement through a variety of conditions. A silver-silver chloride reference electrode (Ag/AgCl RE) was selected due to;

- Stability in contact with aqueous electrolytes.
- Well documented mechanism of operation
- Ease of availability in case of failure
- Freely available filling and storage solutions

Most reference electrodes have three weak points that will cause measurement errors if they change when coupled with the electrochemical cell: The interface with the liquid in the cell, the filling solution or gas, and the electrode body. Additionally, a slow change in chemical composition due to undesirable reactions within the RE, or between the RE and the electrolyte or analyte substance can cause a gradual change in the measured potential between the Ag metal and the electrode filling solution. The RE should be checked against another RE; preferably one that can be regenerated to ensure repeatability. The Standard Hydrogen Electrode (SHE) was unavailable due to safety reasons and no access to flowing hydrogen. However, a temporary SHE was made by Archie Fortuin (a postdoctoral researcher at UCT) and used to check the state of the AgCl reference electrode before each use. It is filled with the aqueous sulphuric acid electrolyte and a hydrogen bubble is generated at the platinum wire to leave approximately half the wire immersed in the fill solution. Before generating the bubble or testing the electrode potential, the system is allowed to equilibrate for 20 minutes to ensure all components are at a similar temperature. Throughout the testing, the Hanna RE potential vs this SHE was kept within $\pm$3mV of 200mV.

Two AgCl RE were tested with the characteristics outlined in table 3.2. The Kowslow AgCl filled with saturated KCl is supposed to remain stable over a wide temperature, because the electrolyte remains at saturation by formation of solid crystals at lower temperatures. However, at 10 °C, a large cubic crystal forms that settles to the bottom of the electrode (which is also the location of the electro-porous KT glass) resulting in an unstable potential vs the SHE. Therefore the HI5313 filled with a gel electrolyte was used.

Table 3.2: Reference Electrodes Tested

Electrode	Junction Type	Electrolyte	Body Material	Operating Temp.	Body Diameter
Hanna HI5313	Ceramic	gel (KCl 1M + AgCl)	PEI	-5 to 30 °C (23 to 86°F)	12mm
Koslow AgCl	Electro-porous KT Glass	aqueous saturated KCl + AgCl	Glass and Teflon	not given	9mm with a 5mm "head"

3.2.4 Counter Electrode

To study the formation and destruction of the double layer at the working electrode surface, there must be no interference from the counter electrode. This is easily achieved by having the CE surface area much greater than the WE, which ensures that the mass transport is not limited at the CE. Due to the high currents involved, an even higher surface area is required on the CE to ensure that contributions to rate limiting or accelerating reactions are limited to interactions at the WE. The CE surface area used here is >100x the WE area (approximately of 300cm^2).

A counter electrode that will not introduce an additional element to the Nitinol surface is desirable. A completely inert counter electrode would be ideal, but unfortunately inert materials are rare and expensive in high volumes. Some options include Pyrolytic carbon or Platinum. Pure titanium was chosen because it will have a low corrosion rate due to passive layer formation, and can be scaled at low cost. Additionally, a tungsten CE was tested, but was found to release tungsten oxide flakes into the solution while continuously dissolving at a high enough rate to turn the electrolyte golden after only a few seconds of high current pulse reverse application. Titanium will also provide an indication of the pulse parameter's effect on the titanium in the Nitinol. This is because titanium forms colourful passive layers with a colour that is dependant on the passive layer thickness. The reaction at the CE will effectively be the inverse of the WE. Thus if the CE is heavily oxidized, it is likely the WE will be experiencing conditions favourable for titanium dissolution.

3D printed polypropylene parts were used to assemble a cylindrical arrangement of commercial purity grade 3 titanium rods. The rods were supplied and machined by Wagner Systems into 6mm OD, 100mm lengths with m3 tapped holes 12mm deep in one end to provide electrical contacts. Photographs of the titanium and tungsten counter electrodes can be seen in appendix D, figures D.3 and D.6.

3.2.5 Reaction Vessel

The reaction vessel must provide the ability to cool and heat the electrolyte between 0-40 °C. The material must be resistant to aqueous sulphuric acid, and should provide an easy method of inserting and removing the electrodes for cleaning between tests.

Three different forms of electrolyte agitation were tested in 3 seperate reaction vessels.

A large jacketed reaction vessel (110mm ID) was manufactured by Glasschem. It was used to test a pulsatile electrolyte flow mechanism, whereby electrolyte was removed from the bottom of the cell and added at the top. However, it proved unsuitable for the small scale testing required for this thesis. A cross section of this vessel is shown in Figure 3.7, with a photograph in appendix D, figure D.1.

An ultrasonic cleaning bath was fitted with a sealing lid which incorporated a glass beaker submerged in the coolant/ultrasound conducting medium (water). It is shown in Appendix D Figure D.2 (b).

A method of transforming ordinary glass beakers into a cooling jacket arrangement was developed. This requires two concentric beakers with a large enough gap between them to acommodate two tubes which act as the coolant inlet and outlet. The beakers and tubes must be placed and suspended above a plastic or metal sheet. The gaps between the smaller internal beaker and the plate should be sealed with moulding clay. The outer tube is then filled to a suitable height with two part silicon and the larger outer beaker is lowered into position 10-20mm above the plate. After the silicon cures, the jacketed reaction vessel is ready for use. Additional features can be added to the silicon top face by including a 3D printed part on the plate to accommodate a lid or other electrode components directly into the vessel. A cross-section of the reaction vessel made by this method is show in Figure 3.6, and a photograph is present in appendix D, figure D.4.

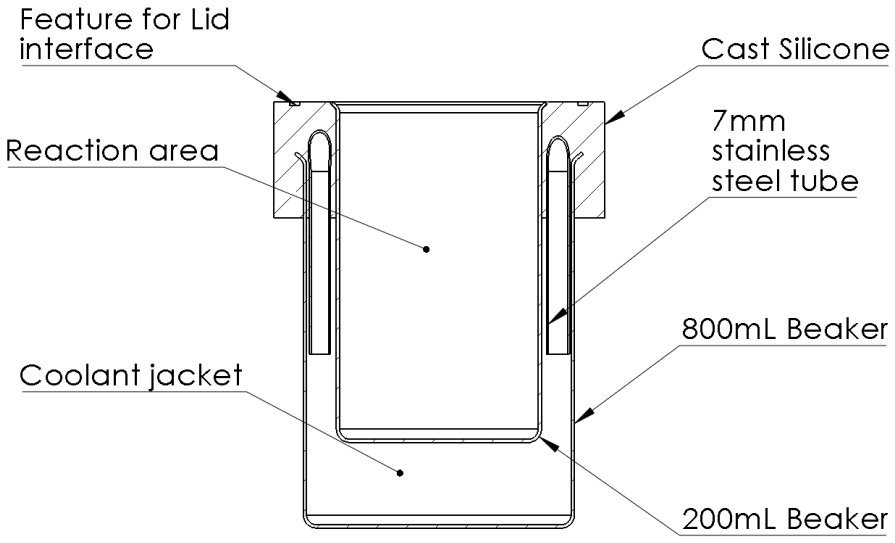

Figure 3.6: Cross section of beaker based silicone reaction vessel

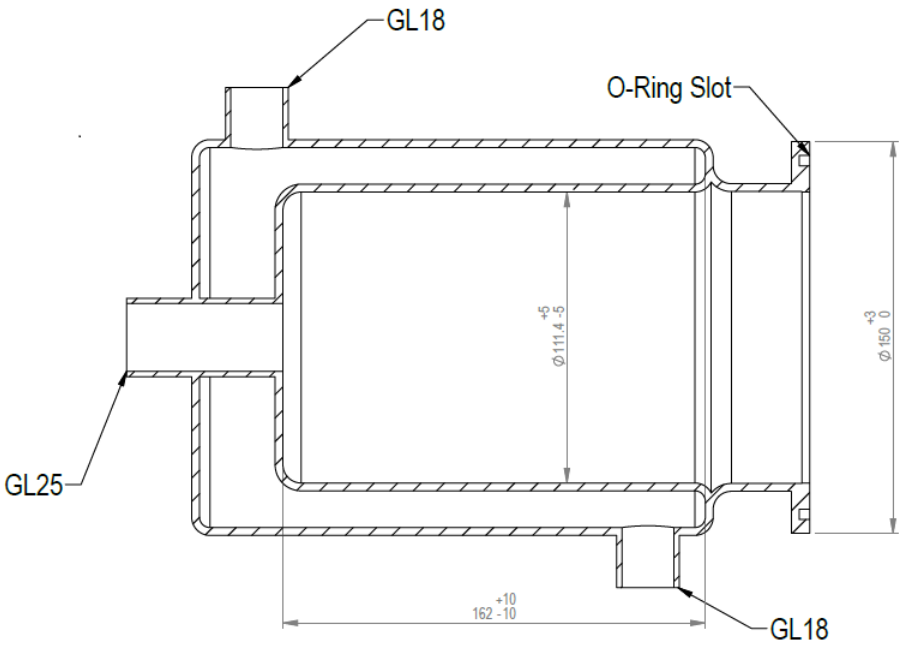

Figure 3.7: Cross section of reaction vessel manufactured by Glasschem

3.2.6 3D Printing Electrode Components

3D printed parts were used to assemble the electrodes into a repeatable configuration. A polymer that is resistant to $H_2SO_4$was required. Polypropylene (PP) 3D printing filament has recently emerged onto the market for additive fused deposition manufacturing (FDM) printers. The 3mm polypropylene filament developed by Ultimaker was used in conjunction with a modified Wanhao Prusa i3 Plus. Polypropylene has excellent chemical resistance and good thermal stability. DSC data on the polypropylene filament revealed a glass transition temperature of 105 °C, confirming its suitability for the 0-40 °C temperature range of its intended use in the reaction vessel.

The first hurdle was to ensure that parts adhered firmly to the print bed, since polypropylene suffers from a greater shrinkage during cooling than most other filaments and is inherently lubricious, thus failing to bond with most build surfaces. To mitigate this the printer was placed inside an enclosure to maintain a higher ambient temperature, and the bed was changed to a glass plate with a layer of PP tape available at most convenience stores. A variety of electrode mounting mechanisms where printed and tested, the simplest and most reliable setup is shown in figure 3.5.

In the following section two types of walls are referred to:

1. Vessel walls - Macro features that make up the geometry of the reaction vessel

2. Shell wall - Artifacts of the 3D printing process, the nozzle is only 0.4mm in diameter and must therefore make several passes to create thicker features. Typically thicker features are composed of several shell walls with a lattice of infill in between.

Initially attempting to 3D print an entire reaction vessel, was unsuccessful. The reaction vessel requires a cooling jacket and PP has low thermal conductivity, so the first attempts were designed with thin vessel walls. Unfortunately, small defects that arise during printing can create flaws which breach the thin shell walls and result in leaking. Additionally, PP is fairly flexible and pressurising the jacket caused some deformation resulting in de-lamination of the layers that make up the vessel walls. These weaknesses can be attributed to the nature of the FDM process, which was in this case performed using a 0.4mm extrusion nozzle. This results in thin vessel walls being constructed from only 3 or 4 passes of the nozzle to construct the shell walls, as shown in Figure 3.8. Thus, efforts to 3D print the reaction vessel were discontinued.

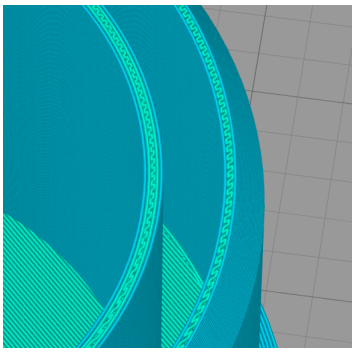

Figure 3.8: Composition of thin walls as pictured in the slicing software

3.3 Electrochemical Methods

Studying electrochemical reactions by potential perturbations has yielded many well-defined relationships. However, most deal with far slower kinetics and reactions than those present during the high frequency pulsating control studied here. For example, cyclic voltammetry will yield information only about a TiO_2 surface layer that will form rapidly on the application of an anodic potential.

A good reference point for understanding reaction waveforms is a Pourbaix diagram, which presents relative elemental stability in a potential versus pH diagram given element concentrations in an aqueous medium. A Pourbaix diagram assumes fixed concentrations and provides the stability of various ions and solids at a given applied potential. It is a purely theoretical description that is calculated on ideal thermodynamic formation energies. The H_2SO_4 electrolyte used had a pH of -0.58. The Pourbaix diagrams shown in this thesis were generated using the materialsproject.org web applet and the Python wrapper for their internet based application processing interface. This allowed the concentrations of the elements to be easily adjusted and colourful illuminating plots of ionic stability were overlaid on the generic diagrams.

3.3.1 Iteration sequence

The parameters presented in the results section are the culmination of approximately 60 electropolishing iterations. Figure 3.9 gives a general overview of the temporal sequence and the iteration loops. The main line represents the temporal sequence. The nodes on the right each represent an iteration loop with the main parameter being modified as the node text. Decisions on what to modify and in which direction were partially informed by observations and partially by considering the principles of diffusion, migration and electric field interactions at the stent surface.

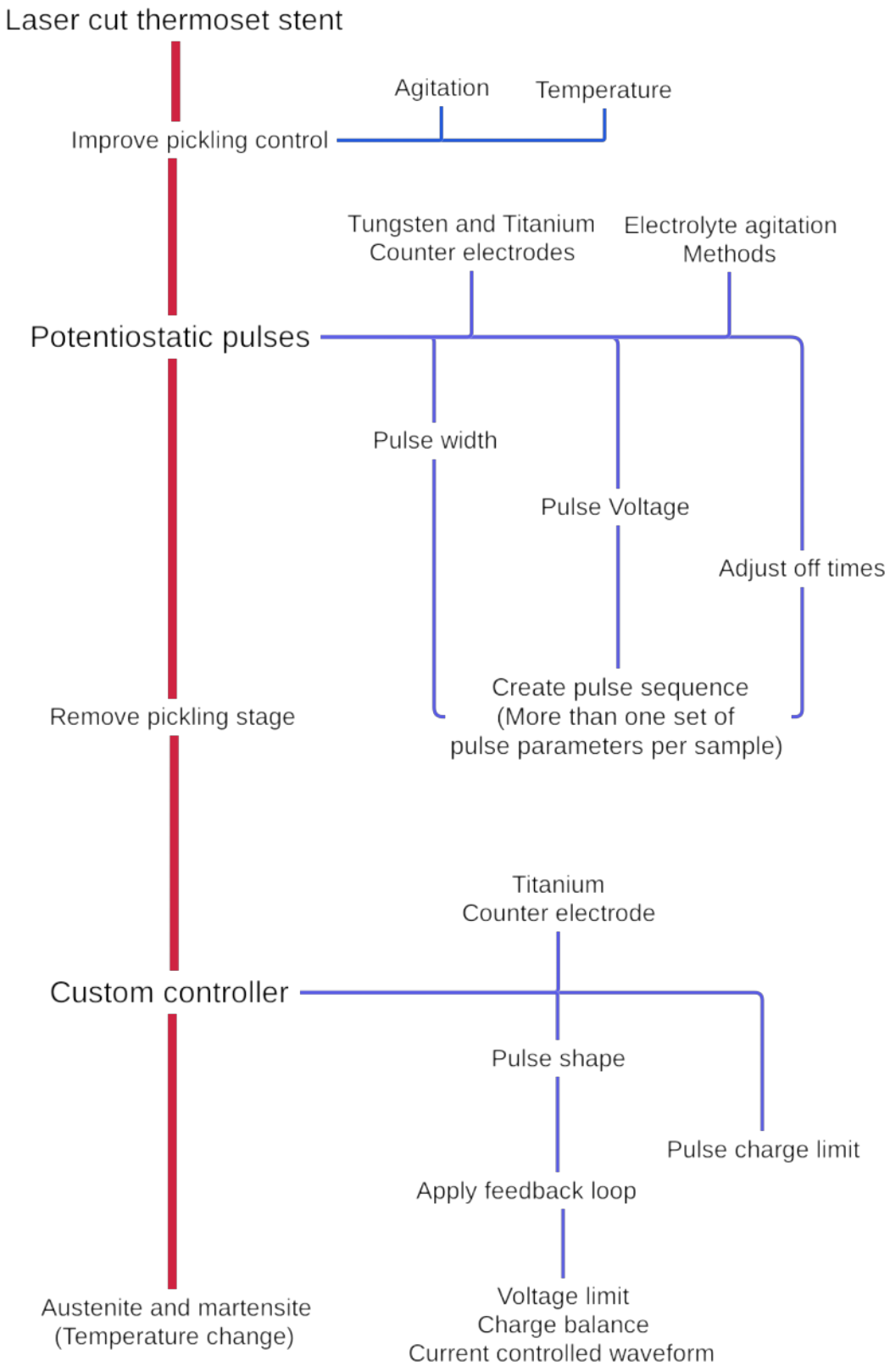

Figure 3.9: Diagram of electrochemical parameter changes and iteration loops

3.3.2 Electrochemical testing process

A general testing method used for most electrochemical tests is outline below:

1. Apply the steps outline in Section 3.1 (stent processing) to create the working electrode (WE).
2. Fill reaction vessel with 100ml of electrolyte.
3. Place the CE in the reaction vessel and wait 20-30 minutes until the electrolyte and CE temperature have equilibrated at the temperature set point. All optimization and development of electropolishing processes was performed with the Nitinol in its Martensite phase at 10 °C unless otherwise specified.
4. Place the stent on its mount into the reaction cell.
5. Wait for the open circuit potential to stabilize before applying a pulsatile waveform for 60-120 seconds.
6. Remove the stent and place it in distilled water.
7. Remove the water by acetone immersion.
8. Remove the acetone by placing in an oven at 60 °C for 30s.
9. Replace the stent into the reaction vessel in the same electrolyte used for the dissolution reaction, and wait until the OCP stabilizes (or 120 seconds) before performing the square wave voltammetry scan.

3.3.3 Square Wave Voltammetry

Square wave voltammetry operates by applying a voltage step, then applying an additional modulation step on that scanning base voltage. The current is measured at some time after the modulation step is applied to obtain the change in current induced by a fixed potential modulated around the scanning potential. Figure 3.10 shows a typical differential pulse voltammetry (DPV) waveform taken from the user manual for the Nova software for the Autolab potentiostat (PGSTAT302N) . A DPV scan utilizes a differential measurement that captures the difference in current values between two pulses. The resulting differential current is a measure of the activity of surface compounds versus voltage which can be directly compared with Pourbaix diagrams given the limitations discussed in the previous section. Unfortunately, the 10A limit on the potentiostat was often exceeded during the positive potential scan, which results in the positive differential peak dropping to zero prematurely. It would be possible to avoid this by utilizing a smaller sample specimen area, but the onset and peak potential provide enough information.

This method of mapping surface reactivity was chosen for four reasons:

1. High sensitivity to small changes in concentration at the electrode surface.

2. The measured current response does not indicate the process taking place at steady state conditions because the measurement is taken soon after the potential perturbation. However, the measurement should be taken after the inflection point when the current pulse dies down due to double-layer charging effects in order to minimize measurement errors.

3. It will be more representative of the behaviour that is likely to be observed during pulsatile control of the double layer than typical cyclic voltammetry or amperometry.

4. The time to perform a full scan can be kept below two seconds which facilitates its incorporation into the electropolishing process as a feedback mechanism.

Several scans were performed varying the parameters to obtain a minimum scan time and high sensitivity:

1. Scan rate (step potential)

2. Modulation amplitude on sensitivity

3. Modulation time on sensitivity

4. Scan range (start - stop potential)

5. The duty cycle = interval time / modulation time

The DPV parameters used for all tests are shown in Table 3.3, and described in Figure 3.10.

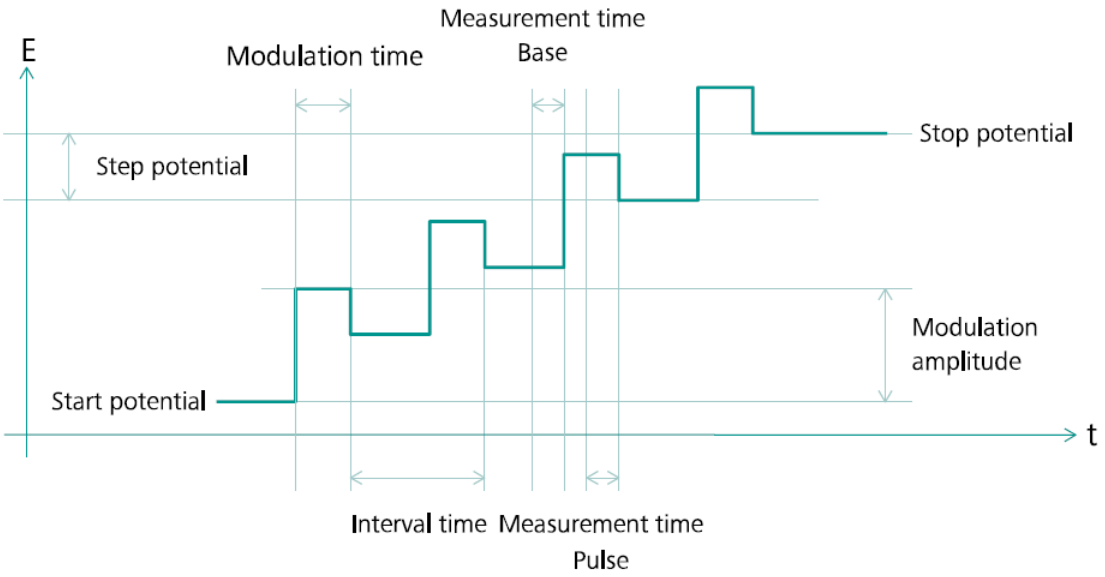

Figure 3.10: Overview of the applied waveform during differential pulse voltammetry [60]

Parameter	Value
Step potential	0.02V
Modulation Amplitude	0.025V
Modulation time	5 ms
Interval Time	10 ms
Total scan duration	1.9s
Scan rate	2V/s

Table 3.3: Differential pulse voltammetry parameters

3.3.4 Corrosion Measurements

There is an ASTM standard for measuring corrosion charectaristics of small metallic implant devices intended for use in the vascular system. According to those recommendations, the following test method was constructed.

The electrolyte is 0.1 M Phosphate Buffered Saline solution (PBS) with a pH of 7.4. This has the advantage of maintaining its pH after de-aeration. The following steps were performed in accordance with ASTM F2129 − 15 Standard Test Method for Conducting Cyclic Potentiodynamic Polarization Measurements to Determine the Corrosion Susceptibility of Small Implant Devices:

- 50ml of test solution was purged for 30 minutes with nitrogen gas.
- All electrodes besides the test piece were placed in the cell and brought to 37 °C ±1 °C. The PBS temperature was monitored with an alcohol thermometer and the electrodes temperature allowed to stabilize for 10 minutes after reaching 37 °C.
- The working electrode (test piece) was placed into the electrolyte, suspended by a retort stand, so that it was not within the stream of nitrogen bubbles or contacting any of the other electrodes or cell walls.
- The open circuit potential was allowed to stabilize until no change greater than 3mV/min was recorded.
- A potentiodynamic scan in the forward (positive or noble) potential direction at a scan rate of 1mV/s was performed.
- The scan is reversed when the current density reaches two decades above the current density at breakdown. This was done by manually observing the graph of potential vs log(current) until the shoulder which indicates breakdown is observed, then checking the current flow and waiting until the current reaches 100 times this value before clicking the reverse scan button.
- The scan was manually stopped when the current dropped back to the passive current density (the current density observed directly after start of test).

- The pH of the PBS was measured before and after each test.

Only a small segment of the stent sample was tested. Specifically, one of the small features added to the end of the stent for this purpose. The fixture method was designed to be similar to the stent mounting system laid out in the ASTM standard. A copper wire with a slot in the end is made. The stent fragment's cut end is inserted into the slot and encased in conductive epoxy (Chemtronics CW2400). The copper and conductive epoxy that is exposed to the test solution is encased in non-conductive epoxy (Dymax 211) with a Nylon 12 extrusion used as a sheath.

The rest of the electrode system is comprised of:

- A small jacketed borosilicate reaction vessel with $\sim$70ml capacity and 4 ports in the top was used.
- The Hanna HI5313 Ag/AgCl reference electrode.
- The stent fragment exposed to the solution had a surface area of 0.35mm^2 according to the 3D model used to laser cut it.
- A platinum wire with a surface area of 15cm^{2}was used as the counter electrode.
- 50ml of PBS was used for each test.

All pH measurements where conducted using a ThermoFischer Orion Star A111 with an Orion 8157BNUMB Ross Ultra pH/ATC Triode.

3.3.5 Potentiostatic Control

Potentiostatic control was achieved through the use of the Nova software provided by Metrohm for controlling their potentiostats. Utilizing the high speed chronoamperometry method permits a sequence of pulses to be specified with a voltage and duration for each step. The sequence can then be placed within a repeat block to create pulse trains of a specific length. The software permits the sample rate of voltage and current to be specified, but places a limit on the maximum number of data points, making it impossible to capture waveform data for a full electropolishing process. Therefore, a two stage program was necessary. 50 pulse cycles are applied while capturing data, followed by the amount of pulses required for the electropolishing cycle and then another 50 pulses with data capture.

While observing the effect of the pulse parameters on the differential pulse voltammogram, the process in Figure 3.11 was utilized. After which a seperate program applied the same pulse train captured in the Chrono methods step, followed by another iteration of the square wave voltammogram process.

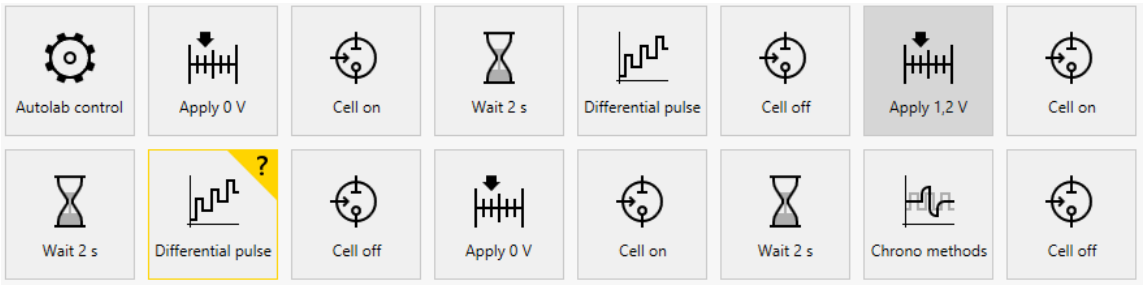

Figure 3.11: Differential pulse voltammogram process with pulse train measurement

A composite pulse method was also used which involved applying a series of 3 different pulse settings in sequence.

3.4 Equipment and Instruments

3.4.1 Potentiostat

The 10A booster module available at UCT with the Autolab PGSTAT302N has a limited bandwidth of just 4.5kHz, and exhibited significant overshoot when performing a large potential step at lower frequencies. This is a common issue in electrical engineering when supplying power to loads with capacitive or inductive properties. An electrochemical cell exhibits external (at the electrode terminals) properties that contain both inductive and capacitive elements. In power supply design, it is common to add inductors or capacitors to the output to stabilize the performance when used with reactive loads. Adding a capacitor between the RE and the CE acts to dampen the potential oscillation measured by the potentiostat, as reactive components in the cell cause the current to oscillate. This is because it adds a charging time constant to the RE response which is proportional to the RE potential. In order to obtain accurate charge transfer measurements, the oscillation will need to be dampened with this capacitor. The capacitor value that was experimentally found to produce the best oscillation damping was a 1.0033uF arrangement of tantalum capacitors. The capacitor was only necessary when using the Autolab potentiostat's built in pulse generation methods and was removed for all testing with the custom feedback controller. The capacitor was also not used during differential pulse voltammetry measurements.

3.4.2 Differential Scanning Calorimeter (DSC)

The Nitinol phase transition temperature was measured utilizing a Perkin Elmer DSC4000.

Prior to sample analysis, a baseline scan was done on an empty pan. If the baseline scan was not flat, then a calibration procedure was performed on an Indium sample kept on hand for this purpose. The Nitinol samples were cut from a stent using a side cutter. The mass of the sample was recorded and it was placed into a

50ml aluminium pan, which is crimped shut using the Perkin Elmer crimper. The sample pan was placed into the DSC with an empty pan in the other slot. The temperature was scanned from 0-60 °C and back to zero at a rate of 10 °C per minute.

3.4.3 Scanning Electron Microscope

Several different SEM were used based on availability.

1. Nova NanoSEM
2. Tescan MIRA RISE SEM
3. JEOL JSM5200

On SEM 1 and 2 the imaging parameters were essentially the same, with only minor variations in the contrast and brightness settings to obtain a good image. The Jeol SEM is old and is only suitable for low magnification images. Notably, most published literature on electropolished surfaces provide SEM images at a relatively low magnification. Few exceed 1000x which is not sufficient to capture the nanoscale surface features affected.

During the initial stages of this project, no AFM was available for surface roughness measurement. Pixel brightness histograms were used as a qualitative measure of roughness. They were created based on a standardized SEM imaging parameter set. The SEM image needed to have a repeatable relationship between surface position and pixel brightness, while having a high enough magnification to capture the surface features. The NanoSEM was operated with the beam perpindicular to the sample surface, 10 000x magnification, 5kV, spot size 3.5. Software autofocus must be executed to ensure that the same algorithm which optimizes the contrast/brightness is applied each time. This is what creates the normal distribution of pixel brightness. An area free from foreign matter inclusions should be selected. Typical brightness histograms for surfaces imaged using the Nova NanoSEM are shown in Figure 3.12.

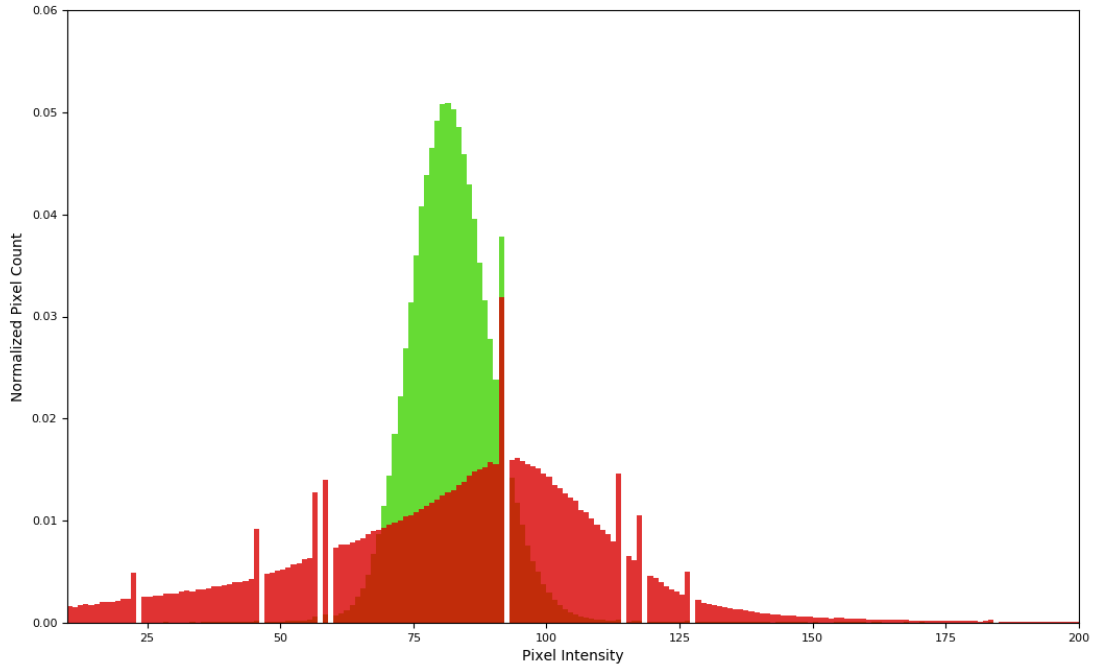

Figure 3.12: Histogram of pixel brightness for SEM images of pre (red) and post (green) electropolishing surfaces

3.4.4 Energy Dispersive X-ray Spectroscopy (EDS)

EDS can provide information about the composition of surface inclusions and defects. EDS is not suitable for thin surface layer analysis however, due to its X-ray emission pattern receiving the bulk of its signal from 1-2 µm below the surface of interest. Although it is unreliable for detection of lighter elements such as oxygen, even weak signals from light elements with unreliable detection accuracy can be trusted if it is a primary signal in the spectra.

EDS accuracy can suffer several sources of error. An area scan was used to minimize the inaccuracy stemming from local variations in composition, such as those along crystal grain boundaries or near subsurface inclusions. Figure 3.14 illustrates how such errors can occur. Where possible, multiple non overlapping area scans where taken from a single site of interest and the resulting mean composition presented.

All scans were performed by scanning a small area which is fully contained within the defect borders, as illustrated in Figure 3.13 by the green square.

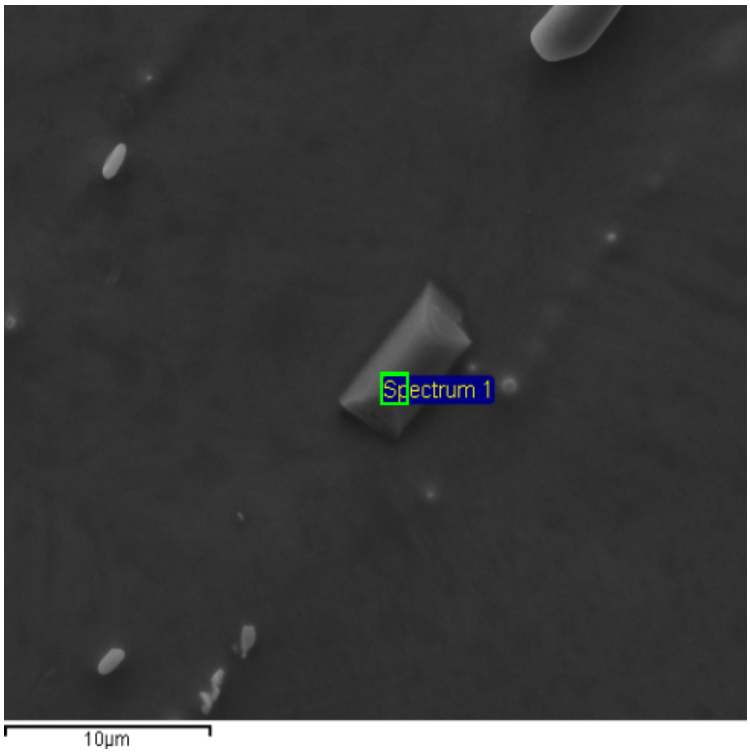

Figure 3.13: EDS Area scanning method

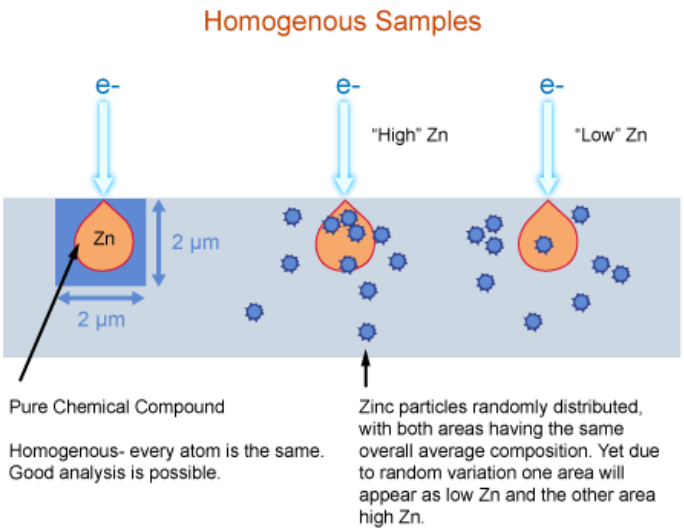

Figure 3.14: Local Variation in composition affecting EDS accuracy [61]

3.4.5 AFM (EasyScan 2.0)

Irregular sample geometries are difficult to scan with an AFM, because the mean plane of the scanned surface cannot be made perfectly parallel to the scanning plane. When dealing with curved surfaces, such as the surface of a stent laser cut from a tube, the surface will have a curvature. Over a 30 µm length orientated circumferentially, a deviation of the curved surface of 50 nm can be expected (calculated from a chord 30 µm long in a 4.495mm diameter circle). This meant that using the AFM in contact mode would be too risky, as the tip could easily run into a feature that would cause it to break, for this reason it was used in tapping mode, wherein the tip is oscillated and the amplitude change in oscillation when it makes contact with the surface is recorded. Some processing of the raw data is required to obtain measurement of the roughness parameters. The Nanosurf Easyscan software was used to extract a 30x30 µm square from the Z axis forward scan channel of the data and export a 3D topology view. The Z axis displacement data was imported into Gwyddion where a mean plane subtraction was performed to level the data. Gwyddion then calculated the surface area roughness parameters. A line scan was extracted by manually drawing a 30 µm long line diagonally across the scan area, positioned to bisect the image. This is displayed as a 2D plot of Z axis displacement. Gwyddion provides options to fit a waviness profile to the data and extract the roughness after the waviness is subtracted. However this yields unrealistically low Ra values in the region of 1-5 nm, so the waviness subtraction was disabled. Gwyddion also provides the ability to average each point by sampling the neighbouring pixels, implemented by selecting a line width for the scan. The roughness measurement drops with increasing line width, so a single pixel width line was used. The oxidic inner diameter of the Nitinol tubing raw material has an extremely rough surface made up of deep crevices and jagged protrusions. It is a bad target for AFM imaging because the scanning head will skip over the narrow crevices and interact poorly with the larger cracks. Due to the rough internal crack features the scanning head will be unable to gauge crack depth. It was sufficient to utilize SEM images that verify that the inner surface and laser cut face were significantly rougher than theouter surface of the tubing prior to electropolishing.

The AFM tip shown in Figure 3.15 had a 10 nm radius in a rotated shape with half coned angles 20-25° along cantilever axis and 25-30° from the side with 10° angle at the apex.

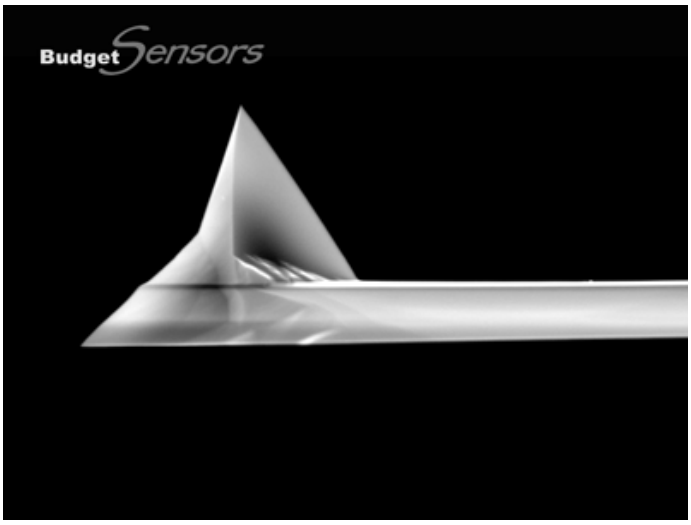

Figure 3.15: AFM Cantilever Tip: Tap 190Al from budgetsensors.com

3.4.6 5 Decimal Balance

The highest precision scale available provided 5 decimal points, which corresponds to an accuracy of 10µg (Mason Technology XS105). The balance was used to weigh the stents between processing stages. In order to accurately weigh the stent, significant amounts of adsorbed foreign matter had to be removed first. This was achieved with agitation in distilled water and then acetone for 60 seconds each.

3.4.7 Temperature Control

Temperature control was achieved using a Lauda Alpha RA 8 refrigeration and heating device. The coolant used was initially ethylene glycol, which was switched to water for use with prototype reaction vessels in case of leakage.

3.5 Custom Potentiostat Controller

Ultimately, applying control using only potential steps resulted in an uncontrolled current waveform, which was dependant purely on electrode surface kinetics and reaction rates. On the other hand utilizing purely galvanostatic control will result in cell potentials that may result in undesirable reaction products. One other complication arises from the need to create an industrially robust process that can be applied to different alloys of NiTi. The ability to create rest periods between pulses that maintain zero net current flow is of course not possible using potentiostatic control without significant trial and error. The potential that produces no current flow changes depending on the initial conditions which are dependant on a variety of factors. Thus, an external controller for the potentiostat which permits greater flexibility with control and feedback was made.

The Autolab PGSTAT302N provides an external input connection (Ein) which accepts a single input and provides two output signals. The outputs correspond to current and voltage measurements at the WE-CE and CE-RE. All signals are ±10V. The input control type is set in the Nova software on the computer to galvanostatic or potentiostatic. In galvanostatic mode, the potentiostat output is equal to the current range multiplied by the voltage on Ein. This means the effective range required for galvanostatic control is ±1V, but is ±10V for potentiostatic control. A dual supply amplifier circuit was made to interface a microcontroller (Arduino Due) with the potentiostat (Schematic in Appendix C.1). The potentiostat could not keep up and did not provide sufficiently high speed data capture while under the control of an external input. Utilizing an oscilloscope, the current and voltage waveforms provided by the Iout and Eout signals on the External Input connector were captured and stored in comma delimited value (.csv) format on a flash drive.

Initially, a ±13.5V switch mode power supply was used to power the controller, but the interference with the operational amplifiers resulted in 100mV of noise on the output. In galvanostatic mode, this corresponds to 1A on the potentiostats output. Replacing it with a ±12V PS2126 linear power supply (which is advertised to produce just 1mV of ripple on its output) reduced the noise on the amplifier output to 20mV. This controller was used to apply custom waveforms that could operate with voltage feedback while controlling the current with the potentiostat set in galvanostatic (current control) mode.

The system's response to a variety of waveforms was examined to gain further understanding of the surface reaction during AC current application. To observe the behaviour of the double layer following a rapid switch in charge transfer direction, a form of pulsatile current scanning was employed (shown in Figure 4.16). This was intended to provide a current baseline to which the voltage change could be compared to gain insight into the physical changes taking place.

The software written for the custom potentiostat controller can be found on Jeran Cloete's Github account at:

https://github.com/MachineKing/MatterCompiler
/tree/master/Arduino/Potentiostat_Controller

3.6 Secondary Reaction Control

The electrochemical reaction taking place to perform electropolishing action is dependent on several interdependent variables. Table 3.4 attempts to logically deduce the dependencies between the variables. The dots indicate that the variable label on that row is affected by variations in the parameter at the top of the marked column. The rows with more dots are the controlled variables and the columns with more dots are the controlling variables. Deciding which parameters to modify to effect a change in the system output (polished stent) can be guided by this reference table, which has evolved over the course of the research. Indirect relationships can be found by following chains of dots, e.g. temperature controls viscosity which in turn controls hydrodynamic diffusion rate. Thus, temperature has a second order effect

on hydrodynamic diffusion rate. Each dot represents a physical relationship which can be described by a mathematical formula.

Table 3.4: Reaction Variable Dependencies

Controlling Variable→	Temperature	Viscosity	Current Density	Electrolyte motion	Voltage	Concentration Gradient	Cation Concentration	cathode area	Magnetic Field
Temperature			♦						
Viscosity	♦						♦		♦
Current Density	♦				♦			♦	♦
Electrolyte motion	♦	♦							♦
Voltage			♦						
Anion Concentration	♦	♦	♦	♦	♦		♦	♦	♦
Cation Concentration	♦	♦	♦	♦	♦	♦		♦	♦
Cathode Area									
Magnetic Field			♦	♦	♦				
Diffusion Layer Thickness	♦	♦	♦	♦		♦	♦		

3.6.1 Hydrodynamic Control

Electrolyte motion is a primary contributor to concentration gradients and the diffusion layer thickness. Turbulence at the surface of the metal will cause variations in the concentration gradient which controls the diffusion rate and thus the mass transport rate. However, a lack of electrolyte flow will lead to a localized change in bulk concentration and a depletion of reacting species, which will cause a gradual change in process variables as the electropolishing proceeds. The ideal conditions under which most theoretical models of electrode kinetics are constructed involve laminar flow across the surface of interest. However, in reality laminar flow is difficult to maintain, even in simple geometries. The nature of the stents under study completely eliminates the possibility of achieving laminar flow. The electrolyte flow regimes which can realistically be achieved are:

1. Continuous uniform flow and turbulence.

2. Pulsatile or binary flow which swings between a turbulent and relatively stagnant condition.

3. Analog variation of flow direction and velocity.

Continuous uniform flow will lead to non uniform diffusion conditions on irregular stent geometries. The second option allows the mass removal processes to occur in relatively stationary conditions, while the electrolyte replenishment is achieved during dead zones in the process. This method is appealing because of its ease of application. However, it relinquishes primary control of electrolyte flow during the dissolution stage.

In order to digitize the control of electrolyte flow, a peristaltic pump with pump-head position control was designed and built. The mechanism was adapted from an open source OpenScad 3D model found on thingiverse.com that has undergone several iterations by various designers.[62] The code was modified to add the mounting mechanisms to fit various stepper motors and a hall effect sensor for position control. Open source and modular electronics were employed to drive the motor. Software running on an Arduino Uno microcontroller receives input from the potentiostat and delivers pulses of electrolyte flow. The volume of the pulse is set by the size of the pump head and the flow rate can be controlled by adjusting the rotation speed. The pump volume was determined by weighing a single pulse of distilled water. A schematic of the electronics built to control the pump is in apendix C.1. A photograph of the controller and 3D printed pump head mounted on a stepper motor can be found in appendix D, figure D.5. The software written for the peristaltic pump controller can be found on Jeran Cloete's Github account at:

https://github.com/MachineKing/MatterCompiler
/tree/master/Arduino/PulsedPeristalticPump

The effect of pulsatile flow was observed using the reaction vessel in Figure 3.7.

A magnetic stirrer was used with Reaction Vessel in Figure 3.6.

The modified ultrasonic cleaner was used to provide cooling and ultrasound application simultaneously.

In all cases, greater pitting occurred when applying electrolyte agitation. The ultrasonic cleaner operated at a fixed frequency of 40kHz, and produced extreme pitting when applied during electropolishing, although it had a very interesting effect on gas evolution and dissolution, causing micro bubbles to freeze and remain suspended in the electrolyte without rising to the surface. Thus electrolyte agitation was excluded from the optimization process.

3.6.2 Gas Evolution

Gas evolution at the working electrode (WE) was observed to occur at a rate which permitted bubbles to form and grow on the surface (hydrogen and oxygen). At low current densities, the bubbles result in bubble shaped craters on the surface after electropolishing. Raising the voltage of the positive pulse from 1.5 to 4.5V shows a steady increase in gas evolution rate, and the electrolyte becomes opaque as tiny gas bubbles saturate the area between the WE and the counter electrode (CE inner diameter = 60mm, WE outer diameter=5.5mm). This produces convection and limits the size of the gas bubbles that remain attached to the electrode surface. When utilizing a square wave voltage pulse administered via the Nova software, pitting was observed with smooth areas between pits. The pitting is most likely due

to surface defects which permit non uniform passive layer breakthrough during the positive (mass transporting) pulse. The non uniformity is exaggerated by the high mass transport rate leading to a runaway pit.

Chapter 4

Results and Discussion

4.1 Material Processing

4.1.1 Raw Material

A large obstacle to successful electropolishing is the oxidised inner surface of the tubing. The SEM image in Figure 4.4 (a) shows the irregular porous structure of the matte black oxide layer on the ID.

AFM data on the ground outer surface is presented in Figure 4.1. An AFM scan revealed an average roughness (Ra) value of 48.62nm which is sufficiently low to maintain a mirror finish. However, it displays a significant maximum height (Sz) over a 30 µm square area of 1.395 µm. The DSC scan of the raw material shown in Figure 4.2, indicates that it will be austenitic when heated above 8.91 °C and martensitic when cooled below -25.41 °C. The extremely wide hysterisis is likely

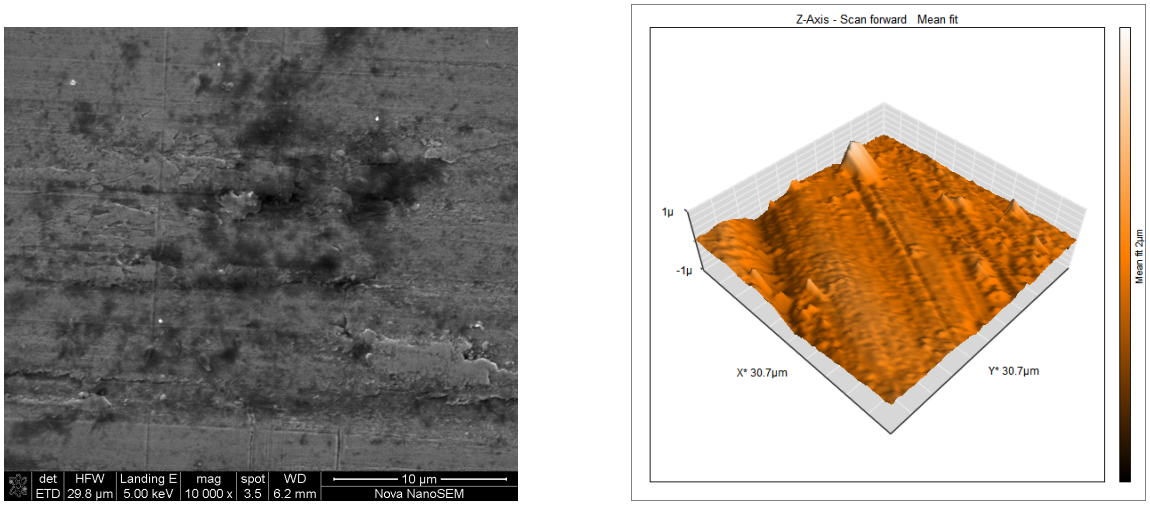

(a) (b) Raw

Figure 4.1: AFM and SEM data for the raw material

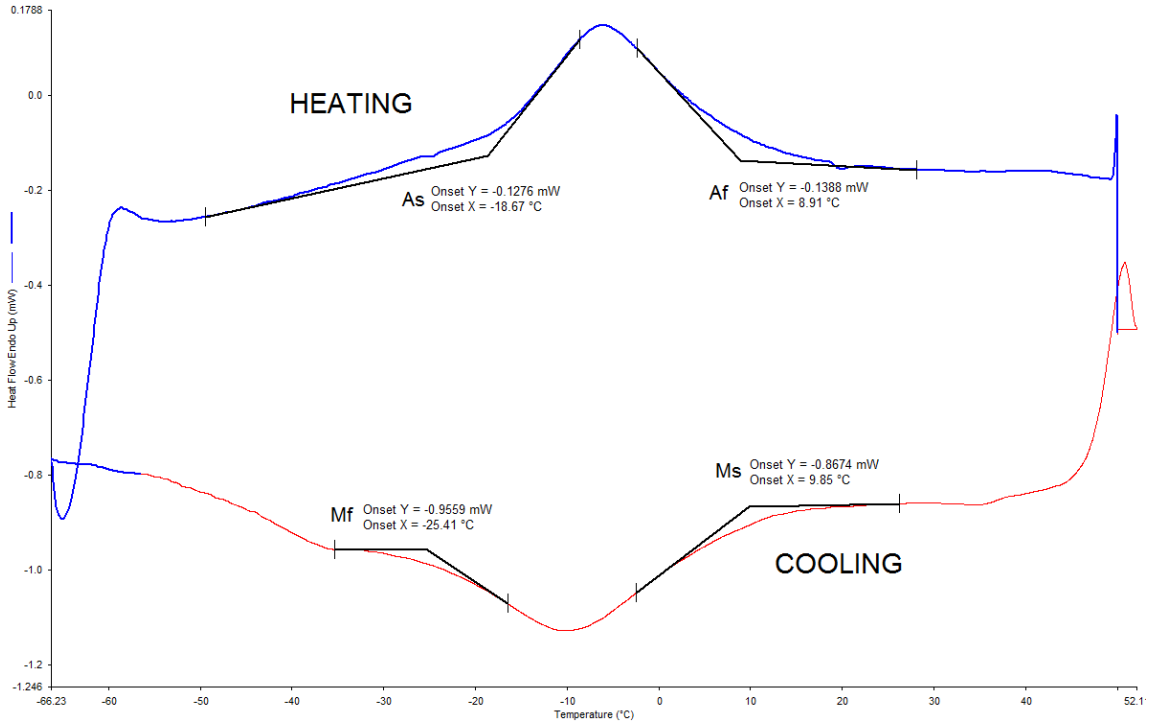

Figure 4.2: Heat flow diagram of SE508 Nitinol raw material

4.1.2 Laser Tube Cutter

A set of higher frequency laser cutting parameters for Nitinol on the Rofin Starcut Laser cutter were identified that deliver just the right amount of energy to cut through the tube in the shortest duration possible. The Rofin Starcut Fibre Laser was set to its maximum frequency and power. The selected parameters are presented in Table 4.1. The cut edge following laser cutting and cleaning in acetone is shown in Figure 4.3.

Table 4.1: Laser parameters selected for cutting the SE508XS 230 µm thick 4.495mm OD Nitinol Tubing

Parameter	Value
Laser Power (W)	200
Frequency (kHz)	20
Pulse Width ρ(µs)	10.5
Pulse Duty Cycle(ρ/λ)	0.21
Argon Gas Pressure (bar)	7
Water Pressure (bar)	1
Cutting Speed (mm/sec)	30

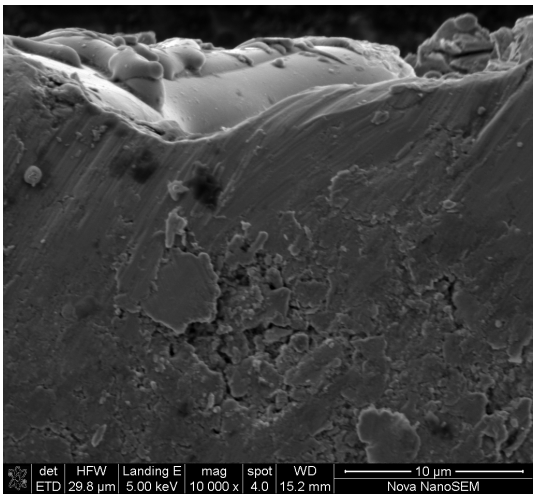

Figure 4.3: Laser cut edge viewed with the beam perpendicular to the inside face (cut area is the top half, lower half is tube inner surface) prior to electropolishing

4.1.3 Thermal Treatment

The stent surfaces following immersion in the fluidised bath are shown in Figure 4.4. The outer diameter is the smoothest, as it has been mechanically ground to a mirror finish. The tube is supplied with a thick black oxide layer on the inner surface which tends to crack during thermal treatment or strain application. The laser cut face is remelted Nitinol which has a large micron scale roughness composed of overlapping segments of melted material. The phase transition temperatures of the stent samples measured after thermal treatment are shown in the heat flow graph in Figure 4.5. It indicates the existence of the Martensite phase below 10 °C and the Austenite phase above 32 °C. A Rhombohedral intermediate phase (R-phase) also emerges that was not present prior to thermal treatment, the R-phase will return to a martensite state upon further cooling below the final martensitic phase transition temperature (Mf).

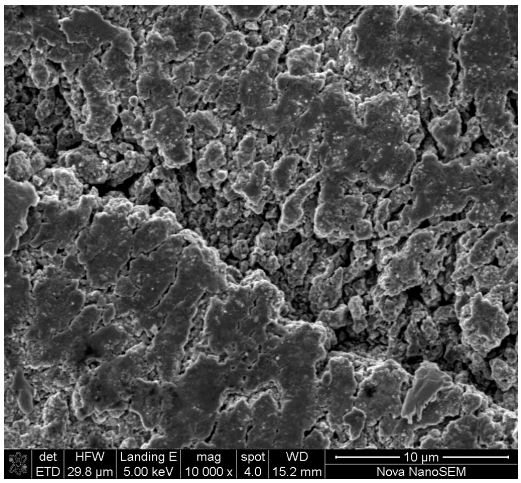

(a)

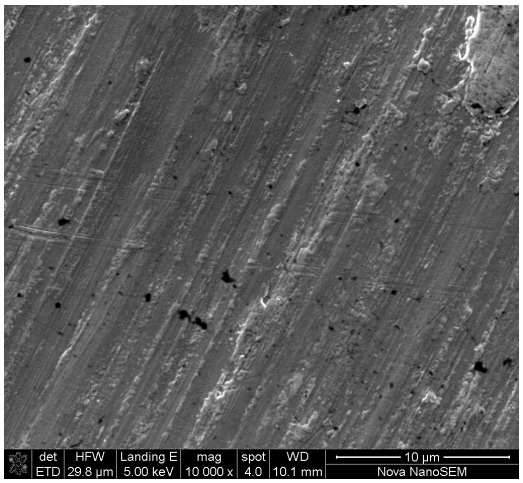

(b)

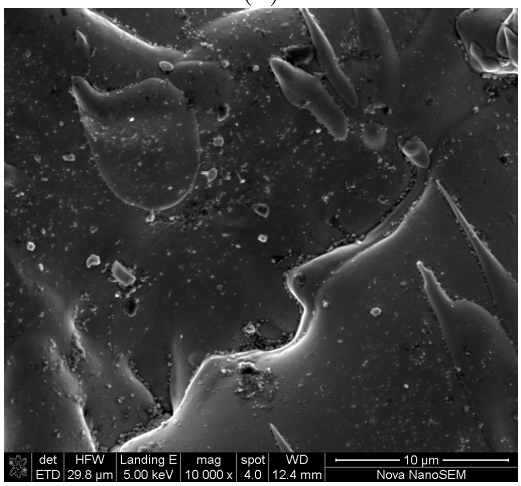

(c)

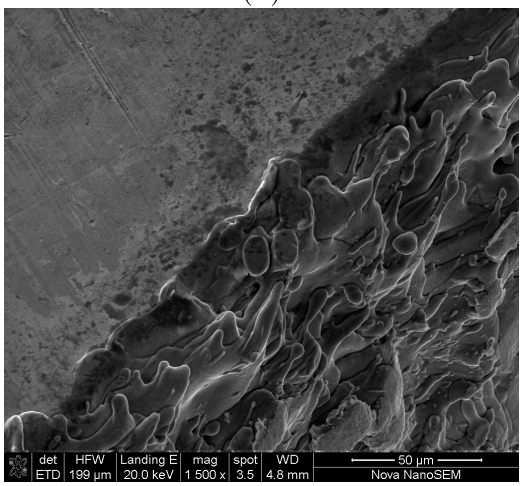

(d)

Figure 4.4: Nitinol stent surfaces following immersion in a Techne fluidised bath. (a) Tube ID, (b) Tube OD, (c) Laser cut face, (d) Tubeouter surface - laser cut face (lower magnification)

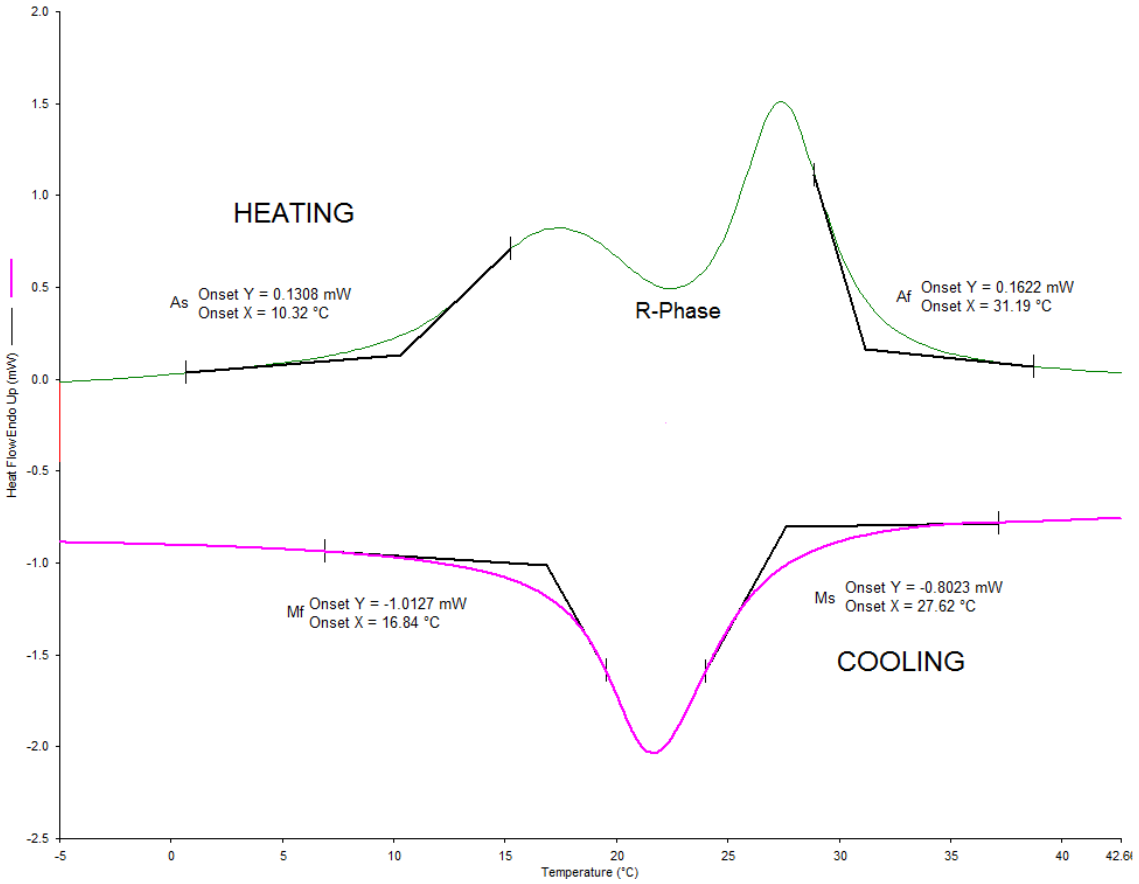

Figure 4.5: Thermoset Nitinol stent heat flow graph

4.1.4 Descaling

The effect of descaling is masked by the pickling step. However, electropolishing without the pickling step (with and without descaling) shows no noticeable difference in surface defects, so the descaling process was discarded.

4.1.5 Pickling

The stent surface after pickling is consistent with etched Nitinol surfaces found in literature[1, 63, 64]. Pickling in this concentrated acid has a powerful homogenizing effect, whereby all surfaces presented in Figure 4.4 are converted to the topology shown in Figure 4.6. Placing a laser cut Nitinol stent into this concentrated acid solution was found to produce highly variable mass loss resulting in extreme pitting and high rejection rates. Close examination revealed a viscous layer forming on the surface of the stent, which would slough away and fall to the bottom of the container in an irregular manner. Adding mechanical agitation as described in section 3.1.7 stabilized the process and ensured even mass removal over the entire surface.

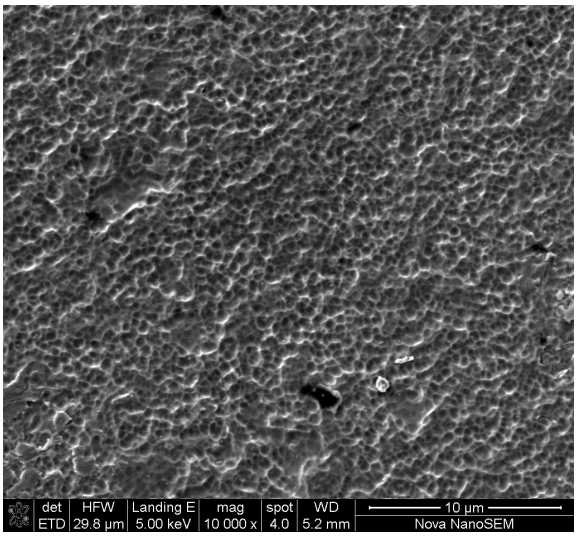

Figure 4.6: Pickled NiTi

4.2 Potentiostatic Control

Chronoamperometry (CA) was performed using a high sample rate and longer (10 ms) pulses. It was found that after an initial high current spike, the current rapidly drops back to a steady state value which continues to fall at a much slower rate. A CA with 2 ms pulses shown in Figure 4.7 illustrates the region of interest. The rise and fall times, as well as the peak and steady state current values, change over the initial 10-50 pulses, after which they remain constant as the anode under study dissolves and a specific surface composition is maintained.

With the initial change in current, the corresponding overshoot in the controlled voltage waveform is an undesirable artefact of the potentiostat's control algorithm. Thus, the height of this initial spike is disregarded in our analysis of the electrochemical processes. Following a change in potential, there is a sharp rise in current, which can be attributed to double layer charging. Following this, the current tapers off and the surface reaction approaches a steady state of ion/electron exchange, called faradayic current. It takes several seconds for charge balance between the electrode and the solution to recover its passive potential (which is not 0 V) following a change. Thus, stepping back to 0V after a pulse causes an opposing current to flow, because the charge stored in the electric double layer and surrounding charged molecules must be dissipated through the reaction-diffusion resistance. This current is a result of the double layer charge dissipating and the (previously) stable charged species near the surface undergoing rapid oxidation or reduction as the difference between their charge and the charge level in the liquid electrolyte (zeta potential) changes. The interval at 0V following the anodic pulse was thought to allow the dissolved ions to diffuse away from the surface and prevent their recombination with the Nitinol surface during the reverse pulse. Analysing the current and charge in a positive voltage pulse following an interval at 0V or directly following a negative pulse as seen in Figure 4.7; the higher charge transfer and current density created in the an-

odic pulse without the interval was hypothesized to be favourable for the creation of a high charge density gradient near the surface and its rapid creation. The 3 factors required for good electropolishing: edge rounding, surface roughness reduction and lack of pitting, were observed with changes in anodic pulse potential, maintaining a fixed reverse pulse potential and pulse width. It was found that higher potentials (2-4V vs Ag/AgCl) yielded greater edge rounding at the cost of surface roughness and a higher incidence of pitting. Lower potentials (1-2V vs Ag/AgCl) created a smoother surface while also producing larger and more widely spaced pitting.

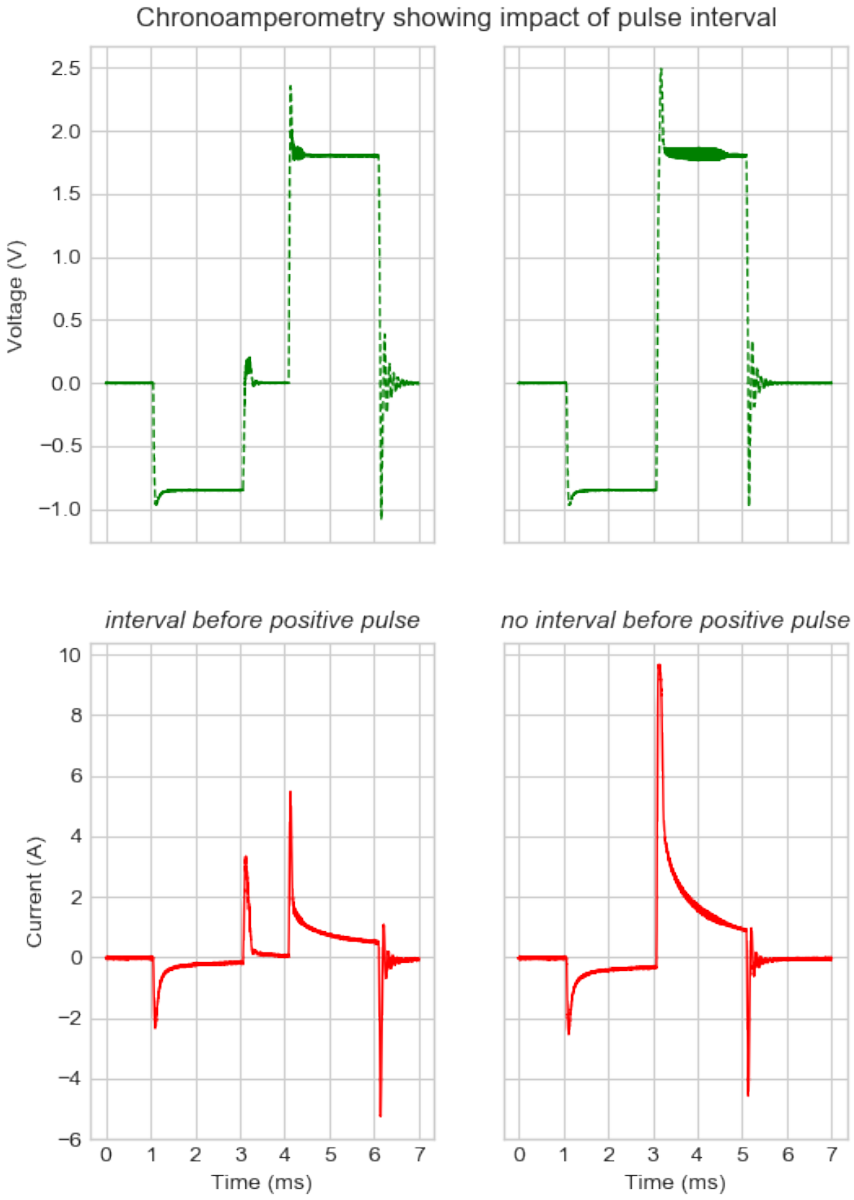

Figure 4.7: Effect of interval between negative and positive pulses

Utilizing a square wave voltage pulse system of 5 ms pulses, multiple iterations were performed observing the surface brightness between tests, the anodic potential was scanned between 0.5 and 3.5V. It was not possible to eliminate pitting from the surface of non pickled stents, regardless of the smoothing effect between pits. This is likely because of the non-uniform breakthrough of the passive layer during the initial high current (>4 A) spike when applying a square potential step. Thus, all further results in this section were applied to samples that had been pickled in the pickling solution outlined in Section 3.1.7.

Initial waveform parameters were selected by attempting to place the pulses at equal activity potentials by referring to the DPV waveform and selecting a potential for the anodic and cathodic pulses so that the corresponding differential currents were similar. This took several attempts due to the open loop control method. Figure 4.8 shows a waveform which produces nearly zero net charge transfer. The effect of this waveform applied for 10 minutes is shown in Figure 4.9. All areas that displayed circular pits were accompanied by tracks along the surface oriented vertically as the stent is mounted in the cell. Therefore the pitting is likely due to gas bubbles forming on the surface and travelling upward, disturbing the concentration gradient in the surface layer. All surfaces processed by this control method exhibited a regular cellular surface appearance which is probably also due to gas evolution. Observing the stent in the reaction vessel during polishing confirms these hypotheses, as a uniform layer of microbubbles is formed on the surface of the stent while arbitrary locations form nucleation sites at which larger bubbles form and grow before detaching and travelling to the electrolyte surface. Figure 4.10 shows this pitting effect, which is observed to form parallel vertical lines. The smoothing result is good, aside from these irregular scars. Initially, the samples polished with this method displayed a patchy surface with rougher areas spread randomly around the stent. Adding agitation to the pickling stage prior to electropolishing eliminated this effect.

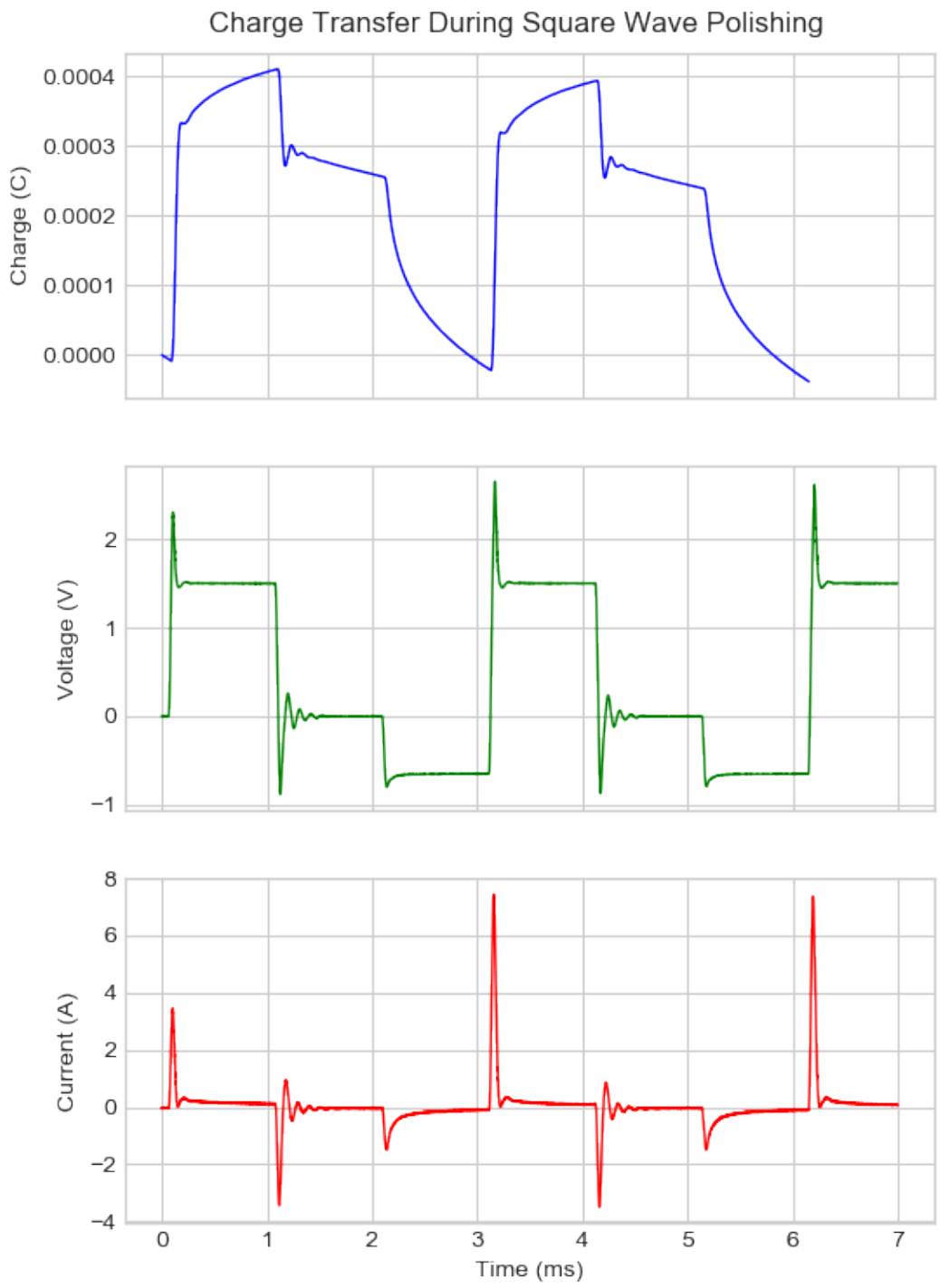

Figure 4.8: Square potential step polishing waveform applied at 10 °C

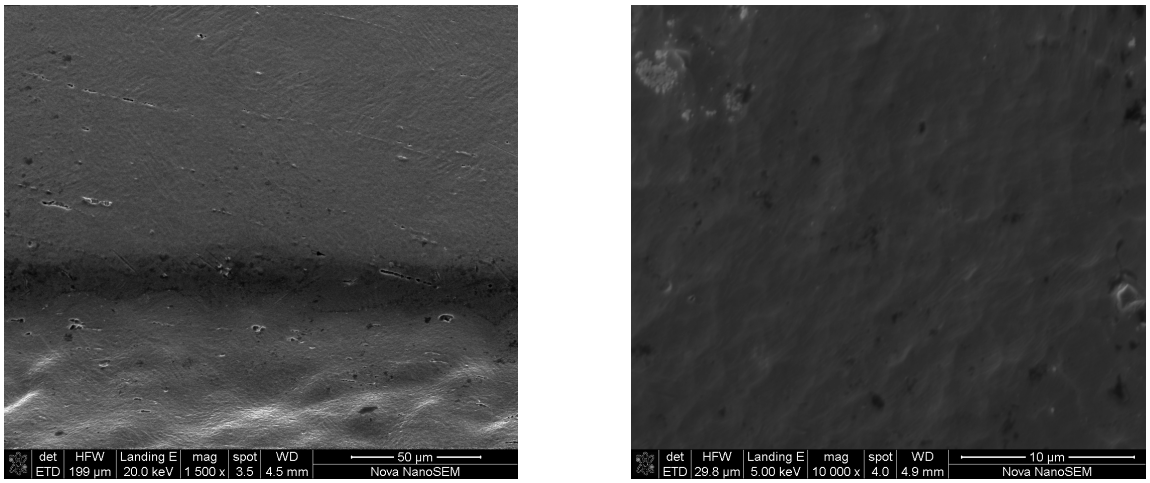

(a) (b)

Figure 4.9: Effect of waveform in Figure 4.8. (a) Edge of strut with laser cut face below and tubeouter surface above. (b) Tubeouter surface at 10kx magnification

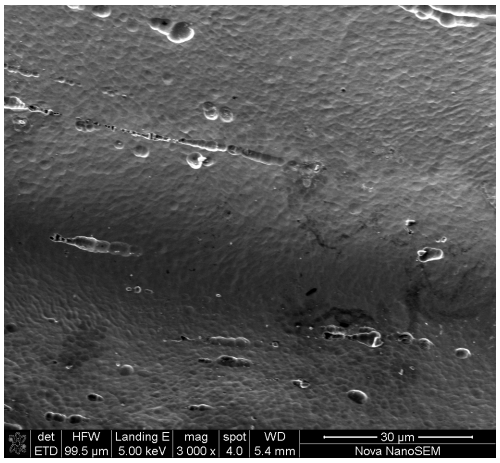

Figure 4.10: Bubble traces on electropolished surfaces (Bottom: Laser cut face, Top: Tube OD) 13 °C.
Stent processing: Laser Cut, Thermoset (4m @ 500 °C), Pickle (45s, 45 °C, Agitated)

4.2.1 Composite Pulse Sequence

Following on the observations that higher anodic potentials produced greater edge rounding but higher nanoscale roughness, it was hypothesized that sequencing a series of potential steps would be able to produce edge rounding and nanoscale smoothing. This would produce a pulsating wave of ionic concentration that would travel away from the surface into the bulk. Initially the pulse settings where applied individually with 3 electropolishing cycles in series and the high voltage edge rounding parameters first. This yielded very high incidence of pitting. Thus, a sequence

was constructed that would apply each set of pulse parameters for 0.3s, looping through all three parameter sets every 0.9s. Although there was still some evidence of pitting as seen in Figure 4.10, this yielded the most uniform surface with edge rounding and nanoscale smoothing. Pickling was required due to the lack of balanced charge transfer between anodic and cathodic pulses, which was applied later using the custom controller. The most successful parameter set which is analysed in section 4.9 (Roughness Measurements), used the following three parameters sets:

Negative V	Positive V	Interval V	Negative duration (ms)	Positive duration (ms)	Interval duration (ms)
-1	2.5	0	10	5	5
-1	2	0	10	5	5
-1	1.5	0	10	5	5

Table 4.2: Most successful sequenced parameter set

4.3 Square Wave Voltammetry

A typical DPV scan of Nitinol is shown in Figure 4.12. In Figure 4.12 (a) the potential was scanned from -3V to +3V. Some sensitivity was lost in the negative voltage portion of the scan and the positive voltage portion would react to the products created in the preceding scan. The scan was split in two, with the negative section being scanned from 0V to -3V, then the positive section being scanned from 0V to +3V after leaving an interval for the system to stabilize. The scan is subsequently stitched together with Python and the portion where the potentiostat booster module had reached its maximum current is cropped. This two-part DPV shown in Figure 4.12 (b) has better sensitivity in the negative voltage range. Note how the sign of the differential current is related to the slope of the base current and the scan direction. The onset and peak positions of the curves in the DPV can be connected to the trends observed in the Pourbaix diagrams, although no quantitative conclusions can be drawn. Comparing two DPV can indicate which has a greater Ti:Ni ratio from the peak positions and onsets. Comparing the Pourbaix diagrams of Ni or Ti rich environments in Figure 4.11, a number of trends can be observed. Generally, the stability bands shift to increase the area in which the abundant element is stable in a solid non ionic state.

- Solid nickel is stable at more negative potentials when Ti is depleted.
- In a Ti rich environment, TiO_2 is the favoured titanium compound for a larger potential band extending from -0.5V above 2V.

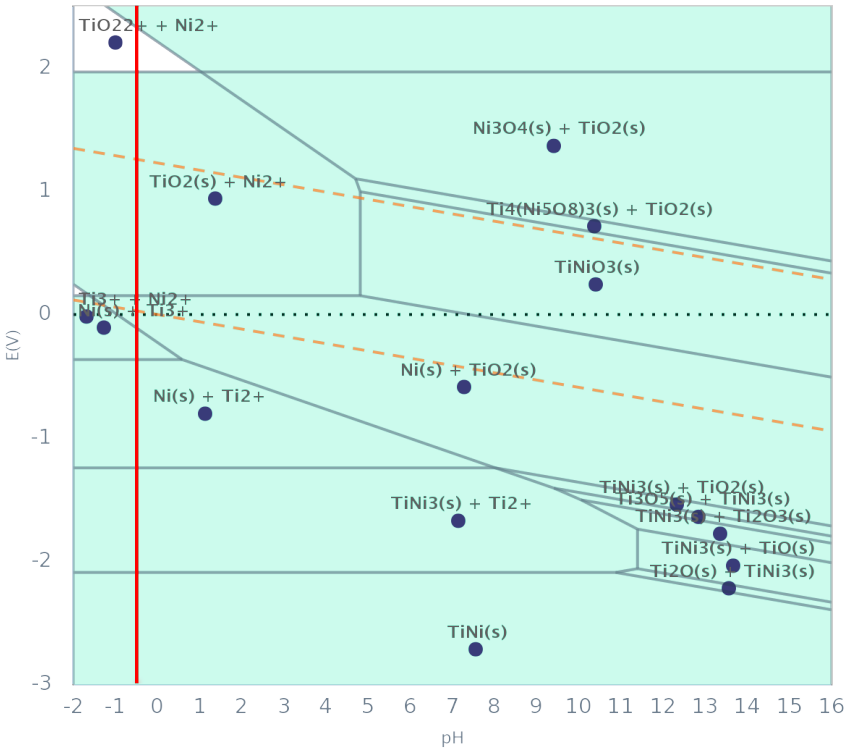

(a) Nickel rich

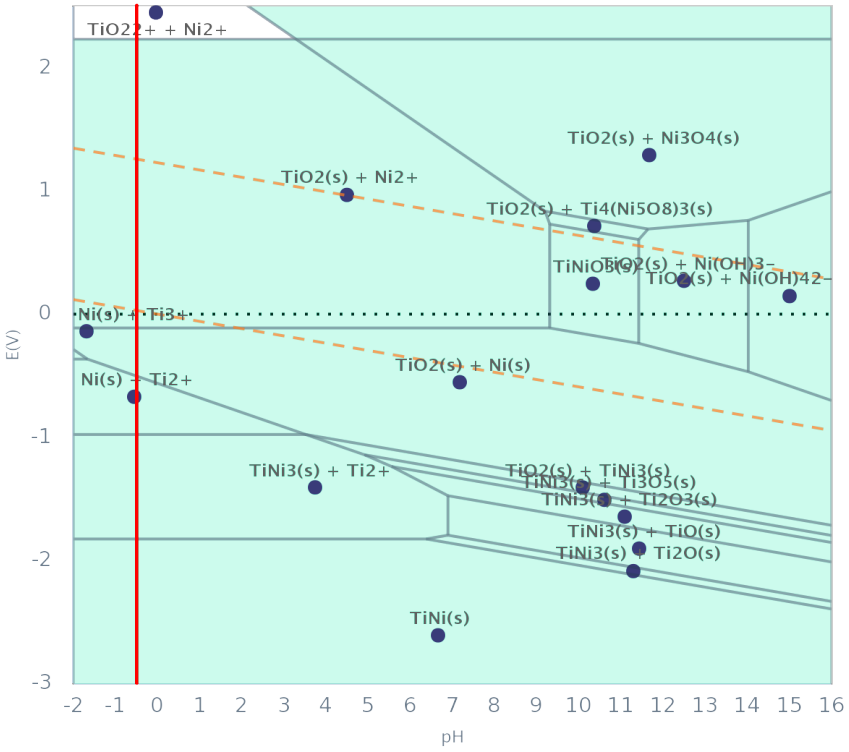

(b) Titanium rich

Figure 4.11: Pourbaix Diagram of NiTi in Aqueous medium for different concentrations (Vertical red line marking -0.5pH), generated using the materialsproject.org web applet[65].

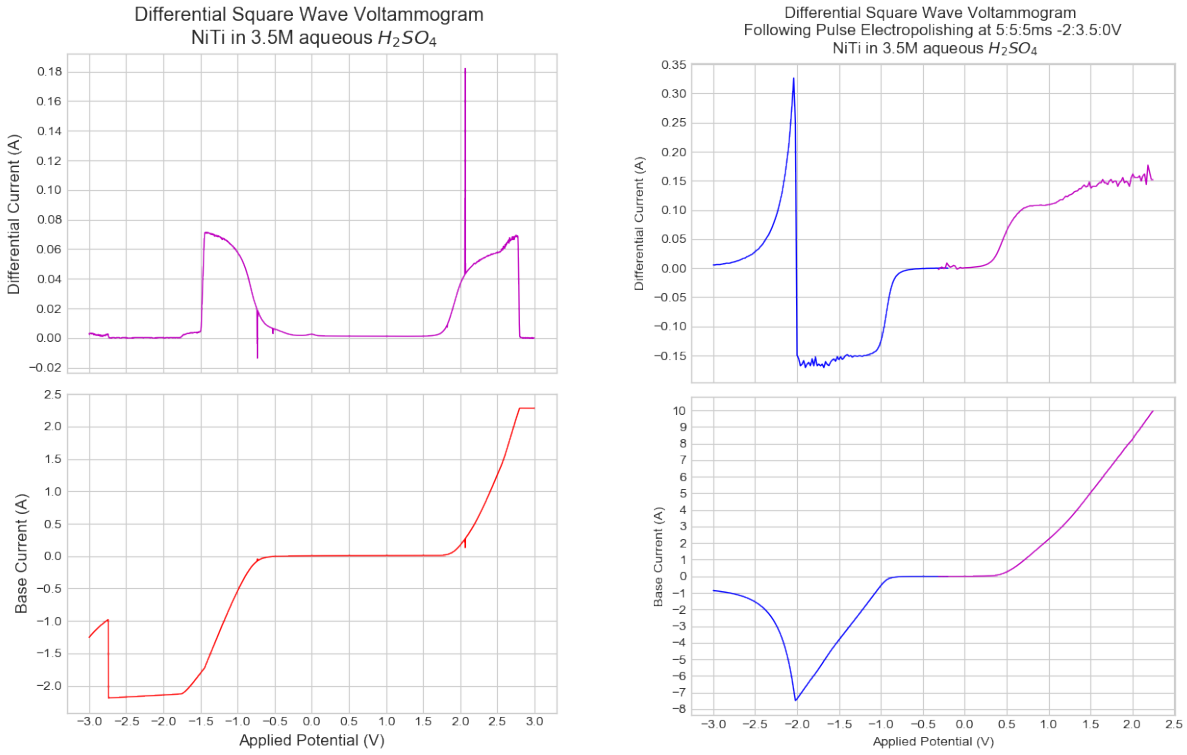

(a) (b)

Figure 4.12: (a) Scanned from -3V to 3V (b) Two seperate scans from -3V to 0V and then 0V to 3V

Observing the peak positions of a differential pulse voltammogram after a certain configuration of pulses is applied until a steady state is reached shows the formation of a repeatable and reversible surface composition.

The effect of anodic pulse potential on surface activity in the negative potential range is shown in Figure 4.13, (applying 50 cycles of pulses made up of three 5ms intervals at -2V, [anodic pulse potential], 0V, varying only the anodic pulse potential. Followed by the DPV scan). There is a clear trend towards increased activity at greater negative potentials with the application of a more positive anodic pulse. A Pourbaix diagram highlighting the stability range of the Ti^{2+}ion is shown in Figure 4.14 (a). The correlation between the activity range and the titanium ion stability points towards a nickel depletion with a higher anodic-cathodic potential ratio since the reactivity of the surface at negative potentials is dependant on the presence of titanium oxides. Nickel is a stable solid at these negative potentials (stability range shown in Figure 4.14 (b)), and so will be unlikely to provide significant contributions to activity in this potential range. Additionally, results presented by Hrapovic et al. also show a higher activity in the hydrogen evolution region after the generation

of TiO_2 surface layers on pure Ti using AC voltage [66] (hydrogen evolution occurs below 0V in the -0.5pH electrolyte used here).

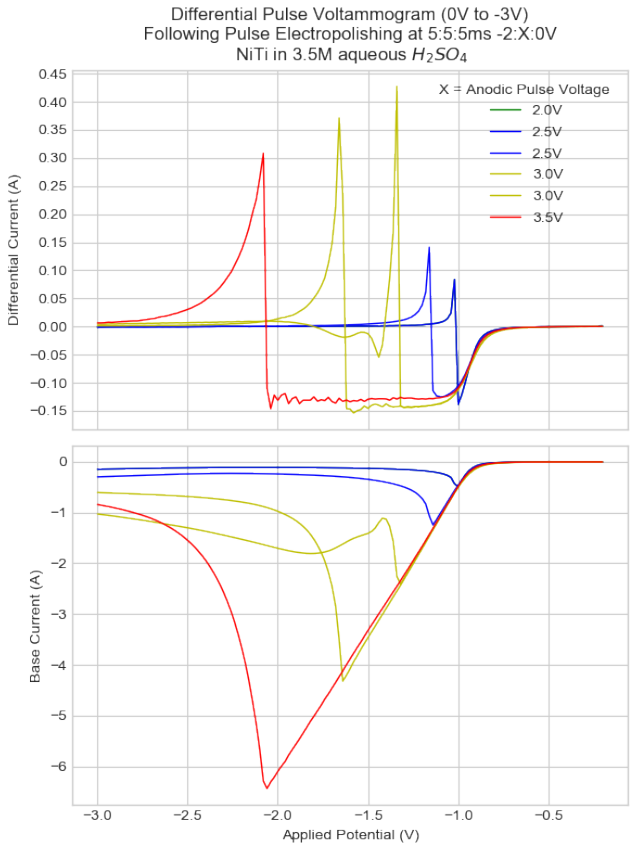

Figure 4.13: DPV scan showing the effect of anodic pulse potential on surface activity with negative applied potential during the scan.

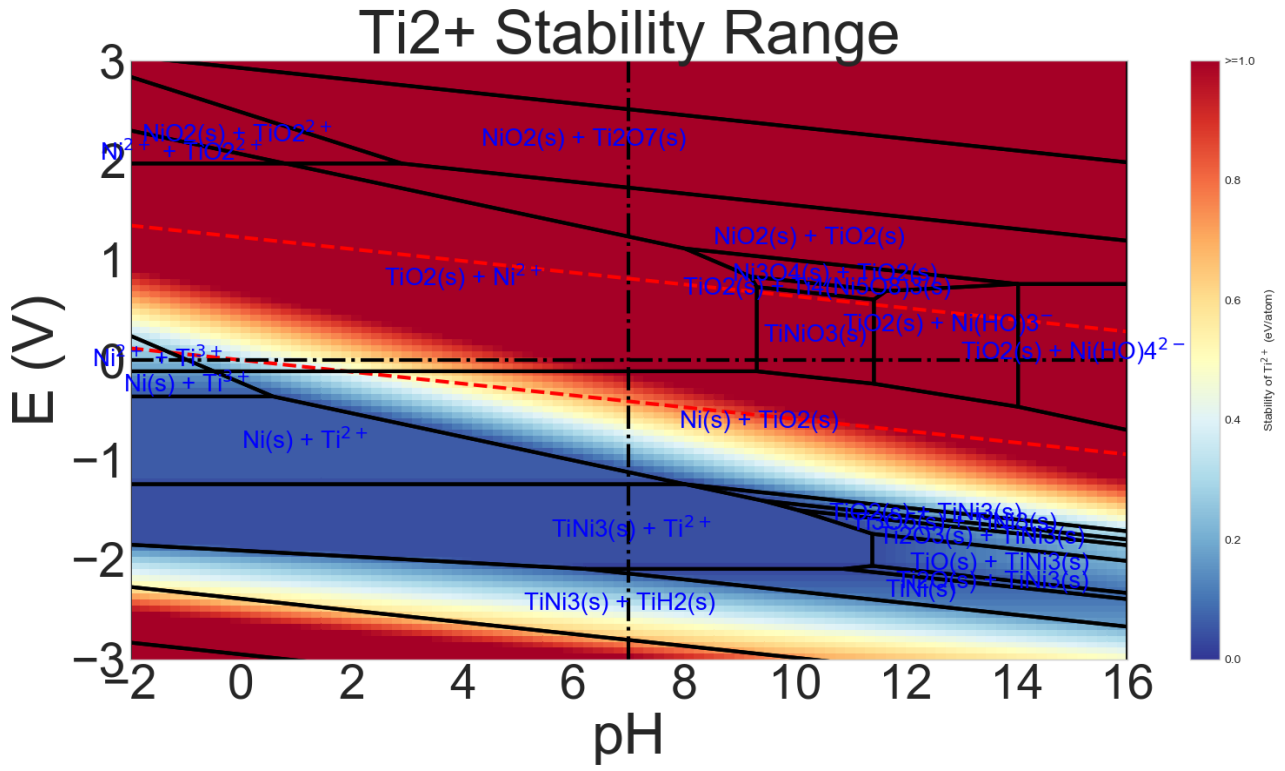

(a)

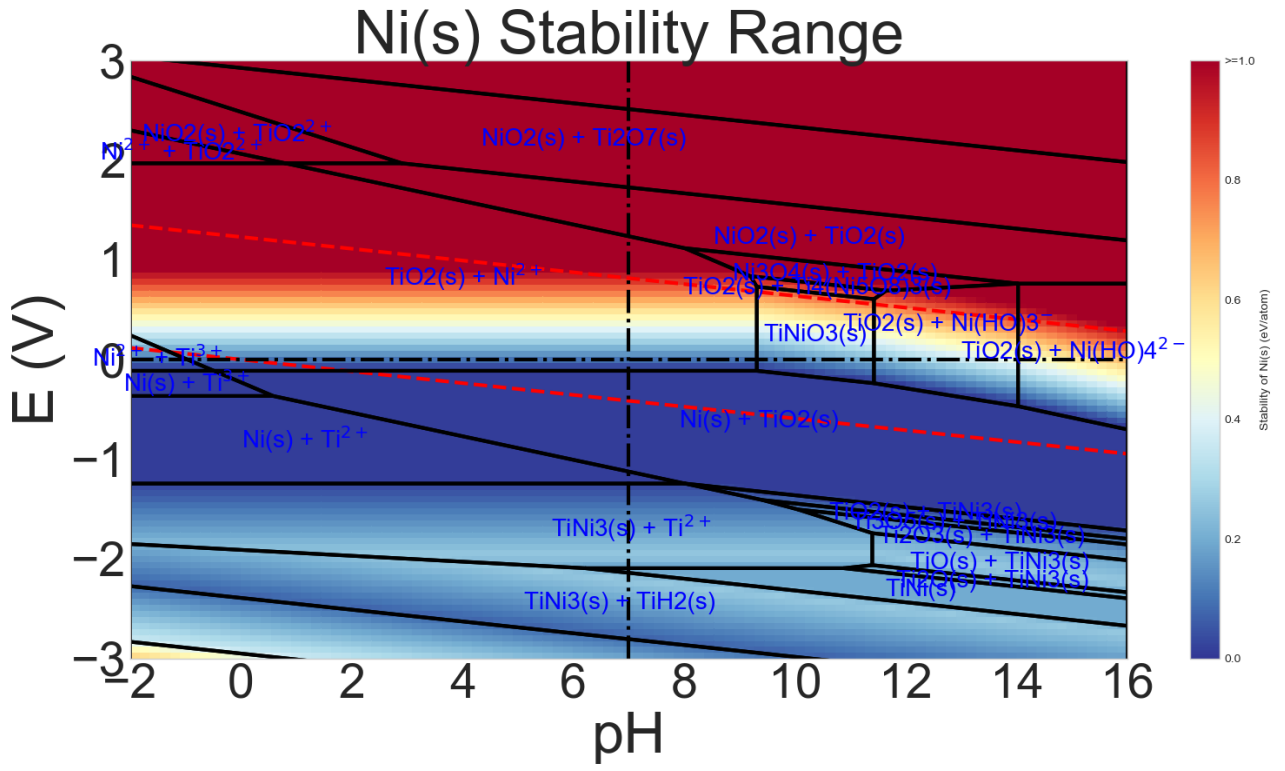

(b)

Figure 4.14: Pourbaix diagram of NiTi system highlighting (a) $Ti^{2+}$and (b) $Ni_{(S)}$ stability range Generated using the Pymatgen Python wrapper for the materialsproject.org API [67].

4.4 Complex waveform Analysis

Using the custom potentiostat controller the following waveforms were generated and the cell response recorded.

There is an important clarification of the language used to describe these waveforms: A negative current is not lower than zero current. The negative current still decreases to zero, because the charge flux is decreasing, although it is numerically increasing (becoming less negative).

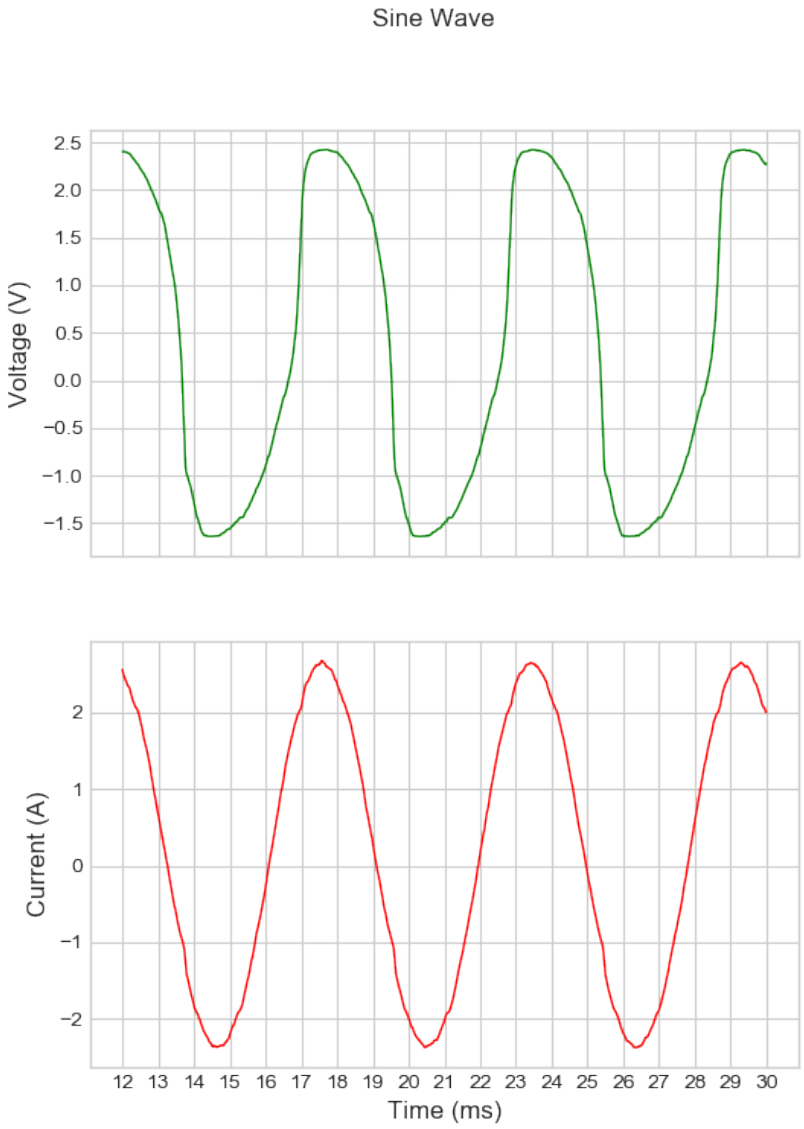

Figure 4.15: Sine Wave

First, the classic sine wave shown in Figure 4.15 displays a voltage waveform typical of a capacitor. The voltage signal lags behind the current signal as the double

layer capacitance absorbs charge. As the current falls again, the capacitor now has a higher charge level than its neighbouring circuit elements and it discharges. The discharge rate is in this case set by diffusion, kinetic rate constants and the activity coefficients of the ionic species present in the electric double layer and the diffusion layer. In an ordinary electric circuit this would be the impedance in series with the capacitor. However, because the former values will change with the pulse parameters, it is not appropriate to build an electronic circuit model at this stage.

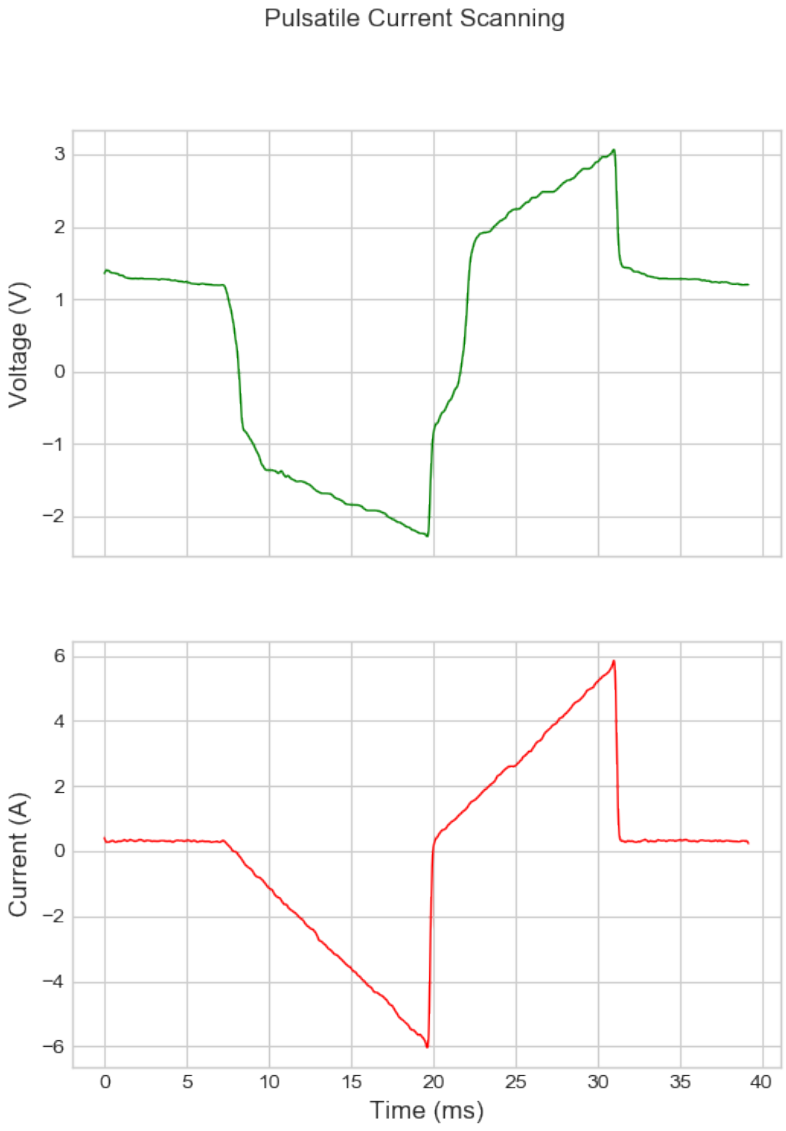

Figure 4.16: Pulsatile Current Ramp

A curious effect is evident in Figure 4.16. With a change in current polarity (negative to positive potential), there is a corresponding drop in negative potential (numerical rise in voltage), observed on every pulse in a 50 pulse cycle. This most

likely represents the change in double layer charge, since this is the most readily accessible free charge in the system. After the double layer contents have switched polarity, the dissolution of metallic species can proceed until the oxidation of the titanium and nickel in the surface layer raises the effective impedance. The potential required to maintain the same change in current rises rapidly until a steady state between oxygen diffusion to the surface, metallic ion dissolution and electron tunnelling through the double layer is reached. The relationship between the current and voltage slopes, then becomes linear and the voltage waveform tracks the applied current waveform. The mass lost during discharge and recharging of the double layer would not contribute to an electropolishing effect because matter would be dissolved when no concentration gradient or surface layer is present to protect the valleys. This mass will remain near the surface and contribute to the concentration gradient which subsequently promotes electropolishing.

Obtaining a smooth surface utilizing pulse reverse dissolution was hypothesized to require that two factors be optimized:

1. The gas evolution at the WE should be adjusted so that there is no continuous bubble growth. This can also be achieved through hydrodynamic interference, but the complex geometry of stents will result in uneven surface flow rates.

2. The titanium available in the non-oxidized form during the anodic pulse should be in balance with the Ni:Ti dissolution rates, so that the anodic pulse does not remove more nickel or titanium than its mass fraction in the surface layer. Matching the charge balance with the surface composition would prevent the situation in which the surface has had all available nickel removed. The remaining passivated TiO_2 would be broken through at the locations of surface defects leading to pitting or irregularities.

4.5 Dissolution Rate

The conditions which promote electropolishing rely on an appropriate gradient of dissolution rate at the part surface. The concentration at a point in the electrolyte close to the surface but outside the electric double layer will be set by diffusion. This is expressed in total mass transported during potential application, if the mass transport is limited by diffusion (this mass transport limited by diffusion will be referred to as the MTL). Below the MTL, the total mass removed from the working electrode is related to the activity co-efficients of the Ni and Ti in the surface layer at the applied potentials and under the charge and discharge dynamics of a specific applied waveform. The electrode kinetics induced by gas evolution and convection also play a role.

The effect of raising the anodic (positive) voltage on the overall mass loss rate (MLR) is shown in in figure 4.17. An increase in MLR with anodic voltage is evident. The samples that were not pickled show a consistently lower MLR, which is likely due to the need to remove the TiO_2 surface layer formed during thermal treatment. The TiO_2 will have a lower dissolution rate than nickel compounds due to its stability at

positive potentials. The pickled samples show a consistently higher MLR and little variation in MLR with a step in reverse voltage which indicates the surface layer dissolution is not impeded by a compound which requires a higher negative voltage or negative charge transfer to react and dissolve.

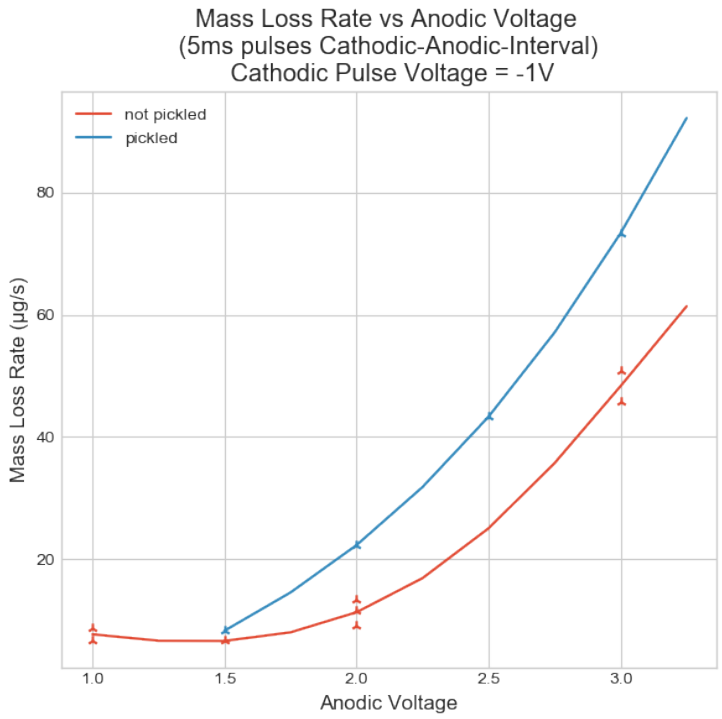

Figure 4.17: Mass loss rate vs anodic voltage
Note: These curves were fitted using polynomial regression algorithms from the Numpy Python library.

4.6 Electropolishing Control Algorithm

A control algorithm was developed to balance the charge transferred in the anodic and cathodic pulses. In conjunction with the charge transfer ratio, a duty cycle (ratio of cathodic:anodic pulse duration) is enforced to influence the gas evolution kinetics. From the Pourbaix diagram, it can be seen that there is minimum oxygen evolution at the WE at anodic potentials below 1.5V (confirmed by visual observation). However, hydrogen evolution begins at any potential below 0V. Thus, an additional control parameter in the form of an anodic pulse voltage limit was introduced, which sets the duration of the anodic pulse after a waveform and desired current density is set. A mathematical representation of the control algorithm is shown in algorithm 4.1. It was implented in C code on the Arduino Due microcontroller in the custom potentiostat controller. The effect of this algorithm is to steadily raise the

Algorithm 4.1 Feedback algorithm for galvanostatic control

$$Tc = Ta \times D$$

$$Ic = Ic + \begin{cases} -0.1 & Qc - Qa > 0 \\ 0.1 & Qc - Qa < 0 \end{cases}$$

$$Ia = \begin{cases} A & \frac{\delta V}{\delta t} > \frac{\delta V}{\delta (t - 0.0005)} \\ A + t * 1 & V < 2.5 \\ 0 & V \geqq 2.5 \end{cases}$$

In Algorithm 4.1 the variables represent:
Tc : duration of cathodic (positive voltage) pulse.
Ta : duration of anodic (negative voltage) pulse.
D : duty cycle
Ic : cathodic (positive) maximum current.
Qc : charge transferred during the cathodic pulse
Qa : charge transferred during the anodic pulse
Ia : anodic maximum current
A : anodic current setpoint
V : applied anodic voltage

4.6.1 Electropolishing With High Speed Charge Transfer

Using the custom potentiostat controller, a potential limit was placed on the anodic pulse of 2.5V, which was selected by trial and error to include roughly 1/3rd of the pulse duration spent in the oxygen evolution region. The cathodic pulse duty cycle was set to 0.5x the anodic pulse. The ratio of charge transferred during the positive and negative pulses was controlled in conjunction with the ratio of pulse durations. The charge ratio was scanned between 0.5 and 3.0 (anodic pulse charge / cathodic pulse charge), observing the surface brightness between sessions. A charge ratio of 1:1 yielded the brightest surface (all other ratio's were not at all bright, with pitting and surface inclusions visible to the naked eye).

The effect of introducing a small delay with the current set point at 0A between the cathodic and anodic pulses is shown in Figure 4.18. At the same time, the initial current of the anodic current scan was set to 2A instead of 0A. This moved the primary current controlled dissolution phase into a positive potential range, while maintaining a higher current density for this period. Following this dissolution phase, a section of charge was transferred in the oxygen evolution region to provide agitation and reduce the bubble size by raising the average evolution rate. The resulting surface roughness was the lowest of all polishing waveforms tested. The SEM was unable to resolve any surface features on an area free from defects and thus an image of the largest pitting feature is shown in Figure 4.19 (b). This result was achieved without the use of a pickling solution prior to electropolishing, which is a major process improvement. However there is a significantly higher incidence of surface inclusions, as seen in Figure 4.19 (d). Once again, surface imperfections were arranged in linear patterns oriented vertically, as the stent was mounted in the reaction cell. Although there is a possibility that this is a result of stress from the original tube manufacturing process, its seems most likely that gaseous evolution is the cause. This hypothesis is reinforced by the reduction in pitting and the elimination of the bubble shaped craters in this smoothest surface. This was achieved by polishing at current densities that ensured the bubble size was kept lower and no visible bubbles were allowed to form and grow on the surface, indicating a "micro bubbling" effect.

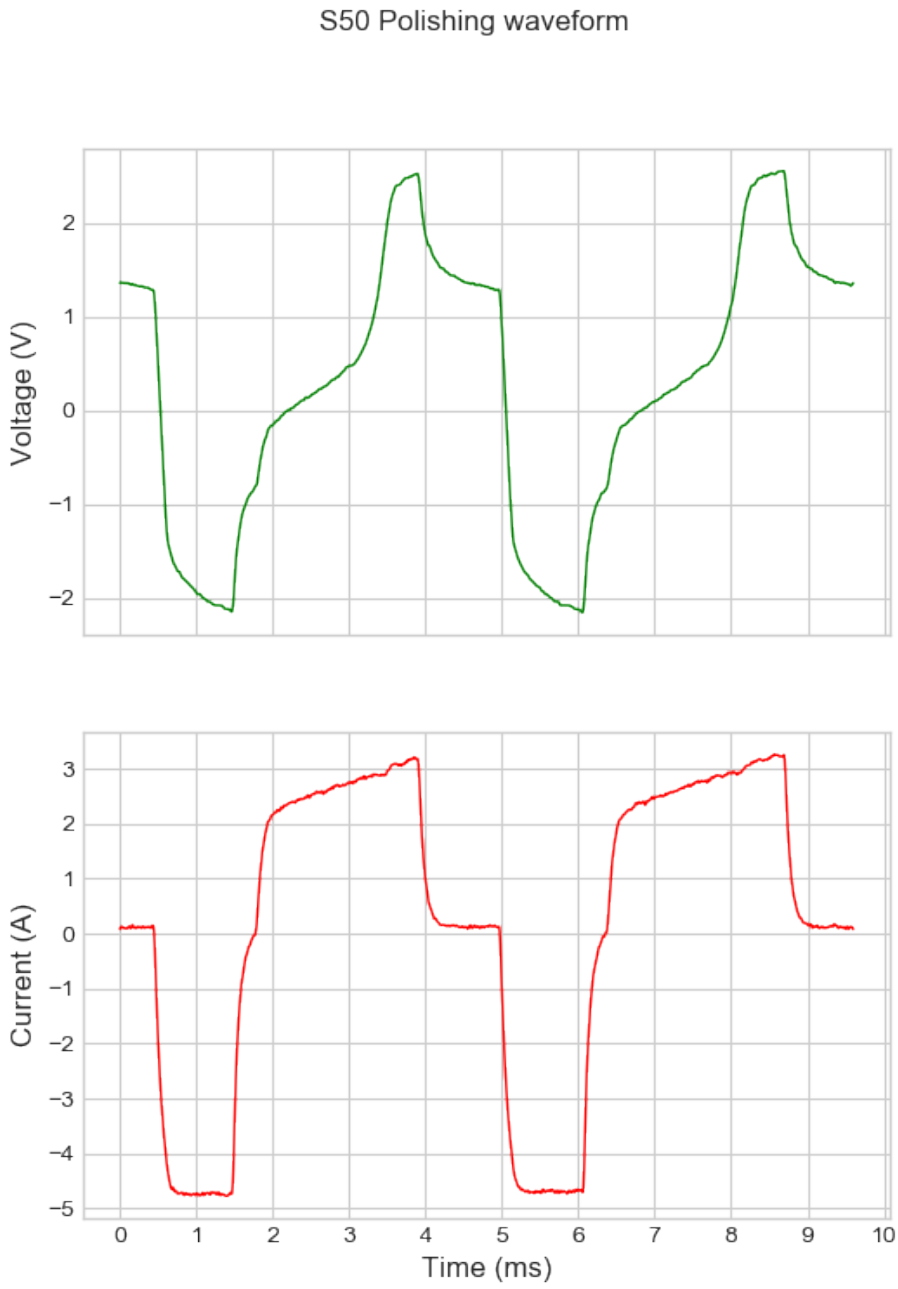

Figure 4.18: Waveform optimized for electropolishing

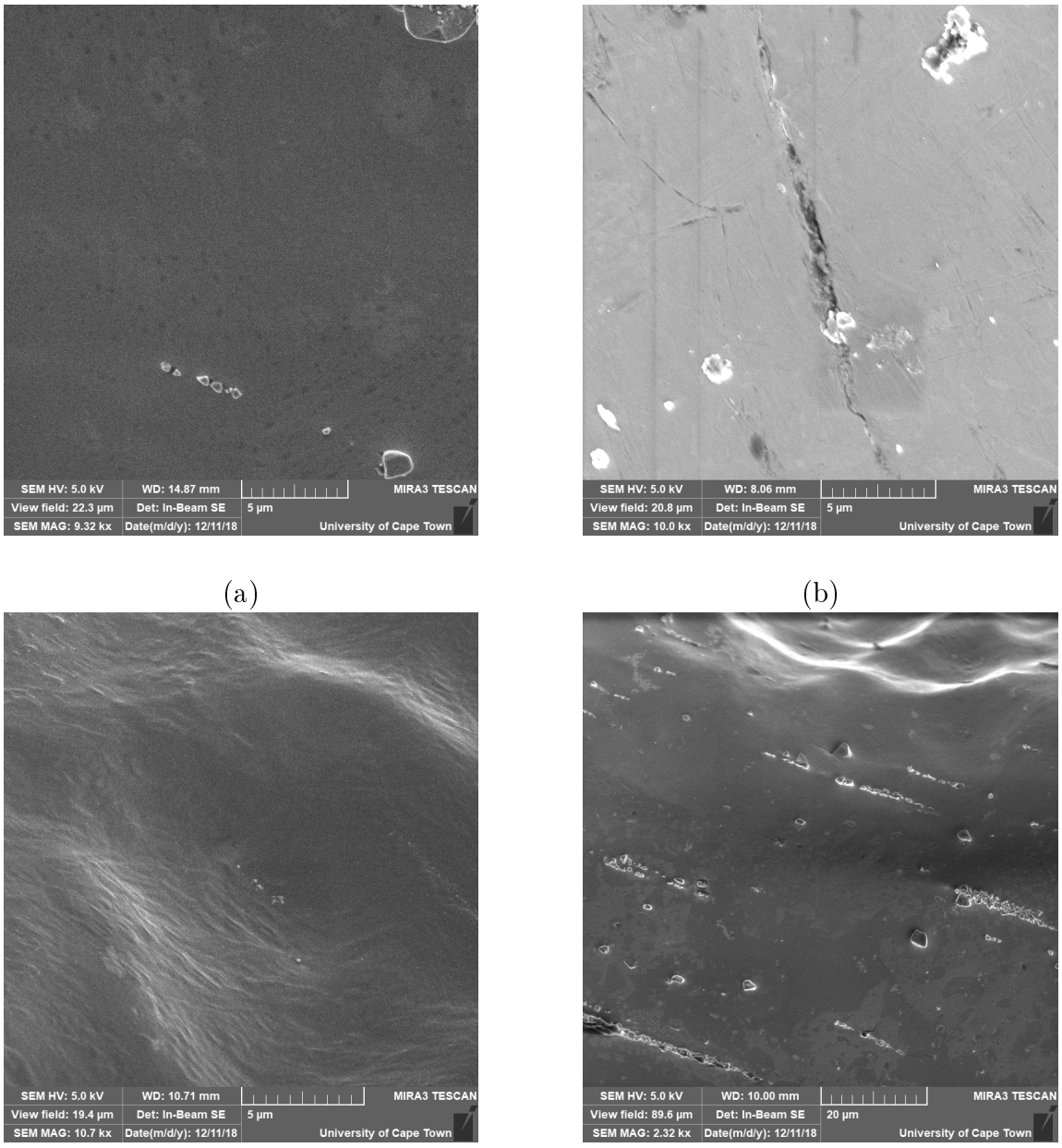

Figure 4.19: (a) Tube ID, (b) Tube OD, (c) Laser cut face, (d) Tubeouter surface to Laser cut face (OD at the bottom, oblique view of cut edge at the top)

4.7 Explanation for Balanced Charge Transfer

It is difficult to accurately classify the reactions that occur during the pulses because it is likely that several different dominant "equilibirum" states are passed through as the charge density builds up and the difference between the Fermi energy in the metallic surface and the lowest occupied molecular orbital in the electrolyte shifts.

Equations 4.1 and 4.2 show all the possible reactants and products sourced from the Nitinol part during the anodic (4.2) and cathodic (4.1) pulses.

$$TiO_2 + TiNi_3 + TiNi + NiO_2 \rightarrow Ti^{2+} + TiNi_3 + Ni(s) \tag{4.1}$$

$$TiNi_3 + Ni_{(s)} + TiNi \rightarrow Ni^{2+} + TiO_2 + NiO_2 \tag{4.2}$$

$$2H^+ + 2e^- \rightarrow H_2 \tag{4.3}$$

During the cathodic polarisation, electrons leave the Nitinol and are accepted by the hydrogen ions in the acid, causing hydrogen evolution as in equation 4.3. The electrons must travel through the TiO_2 surface layer and get accepted by the positive adsorbed hydrogen and sulfate ions. Ordinarily, the steady state of this process would involve diffusion of ions to and from the surface. Due to the extremely rapid polarization cycles used, the main limiting factor is initially the polarization of the electrolyte ions near the surface as they adsorb and the electric double layer is formed, leading to a rapid rise in measured potential. Although equations 4.1and 4.2 are unbalanced the nickel and titanium dissolution both involve the transfer of 2 electrons and oxygen. Since the Nitinol is nearly binary (56% Ni), this gives an indication of why the charge balance between positive and negative pulses must approach 1.0.

4.8 Surface Inclusions

Several common surface defects were observed under the SEM on polished parts. For reference, all flat areas around the inclusions reflect the data sheet values for the NiTi alloy used (56 wt% Ni and ~44 wt% Ti). By far the most common inclusions are irregular lumps that take a smooth round appearance and are sometimes accompanied by black patches on the surface nearby, as shown in Figure 4.20. When electropolishing samples that had not undergone the pickling process, two distinct types of inclusions were present. The type shown in Figure 4.21 (a) appears to be a titanium carbide crystal. It takes a regular geometric shape, or forms an oblong rounded version of the same shape. The EDS data on this shows a high Ti:Ni ratio, indicating that it is mostly titanium. The regular geometric shape found in a few of the inclusions of this type fits with the assumption that the electropolishing waveform is creating a surface with a minimum free energy. The other type shown in Figure 4.21 (b) is an irregular porous structure that always appears in linear clumps. The EDS shows a higher carbon content than the crystalline inclusions, as well as a higher Ti:Ni Ratio than the bulk. It is likely that these are formed from titanium dioxide fragments bound together by titanium carbide and clumps of carbon. This type of surface defect is almost entirely eliminated by electropolishing in the Austenite instead of the Martensite phase as shown in the low magnification images in Figure 4.22.

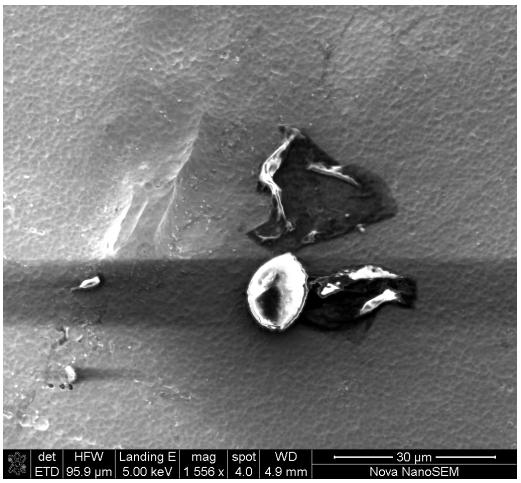

Figure 4.20: Inclusion on electropolished surface that was pickled prior to electropolishing

Description	C	O	Ti	Ni	Number of samples averaged
Black patches surrounding white spot	48.60	14.69	18.75	17.96	3
white spot	95.38	1.83	1.71	1.08	1

Table 4.3: EDS atomic percentage data for inclusion in Figure 4.20

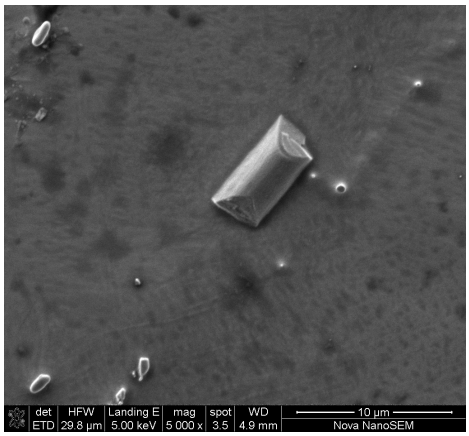

(a)

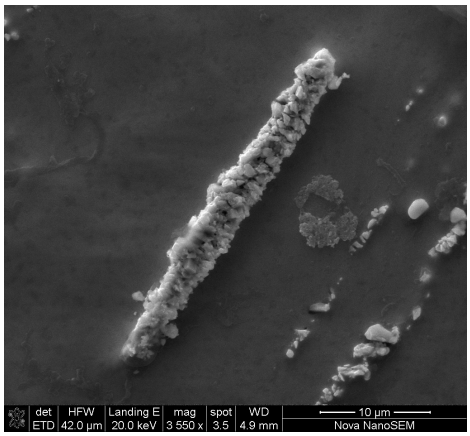

(b)

Data Type	C	O	Ti	Ni
Atomic%	15.61	19.09	43.6	21.7
Weight %	4.88	7.96	54.15	33.01

(c)

Data Type	C	O	Ti	Ni
Atomic %	29.1	22.04	30.42	18.45
Weight %	11.07	10.8	44.78	33.35

(d)

Figure 4.21: Surface defects on unpickled electropolished surface and EDS data on the inclusions

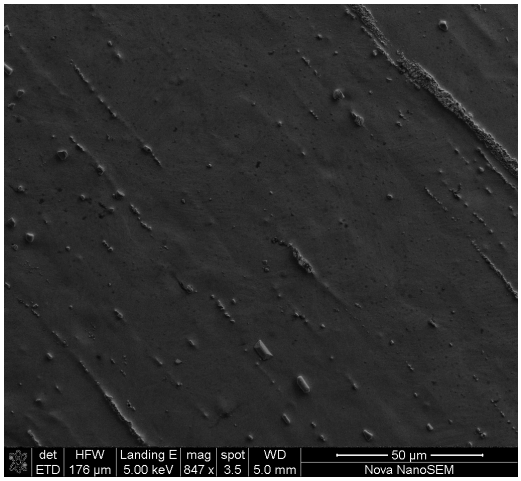

(a)

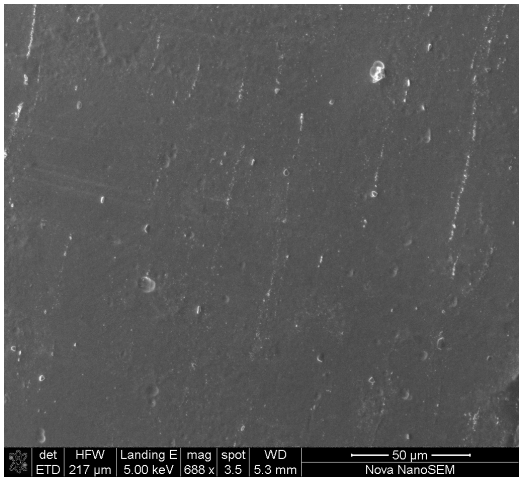

(b)

Figure 4.22: Nitinol stent surfaces electropolished in different crystal phases (a) Martensite (10 °C), (b) Austenite (35 °C)

4.9 Roughness Measurements

Classical roughness data is usually presented as an Ra value, which represents the average deviation from the mean. This is a somewhat misleading parameter, as it fails to account for larger irregular features, and it is blind to the spatial period of larger surface deviations. Subsequently, the Ra value is usually the smallest value of all the numerical roughness parameters that can be calculated. As a result, it is necessary to include several parameters to fully characterize a surface. Depending on the desired application, different parameters may be relevant. For example, minimizing corrosion susceptibility relies on reducing the effective surface area, thus the ratio between projected and actual surface area is a useful parameter.

Comparisons of roughness measurements before and after electropolishing were all done on a surface that was originally the tube outer surface. SEM images have shown that all three characteristic surfaces (outer, inner and cut edge surfaces) attain similar visual roughness after electropolishing. However, the laser cut surface maintains a macro (or micrometer) scale waviness upon which the roughness features reside, making it extremely difficult to map with an AFM. The inner diameter and laser cut face undergo a far greater reduction in surface roughness than the outer diameter used for comparison. The most drastic change in surface topology was on the initial inner diameter to the final electropolished surface shown by the SEM images in Figure 4.27. However, it is more valuable to present the best surface prior to electropolishing in order to verify that the process does not introduce any roughening.

SEM and AFM data on the electropolished surfaces produced here are presented in Figure 4.26. For comparison, a surface electropolished using a DC method at SAT and a commercial electropolishing solution , are presented in Figure 4.25. Line scans extracted from the AFM data are presented with equal y axis scales in Figure 4.23. Roughness measurements calculated based on the line scans vary between 0.01-0.15 µm Ra depending on the line orientation and position. Therefore, it will be more useful to look at roughness parameters calculated on areas. A comprehensive table of roughness data gathered from AFM scans is presented in table 4.4. A bar graph comparing the roughness (Sa and Ra values) of the surfaces analysed here is presented in figure 4.24.

The electropolished samples presented in this section were processed by two methods:

1. Pickled and electropolished using potentiostatic control and a sequence of voltage settings shown in table 4.2 in section 4.2.1.

2. Electropolished without pickling using the custom potentiostat controller balancing the charge in the pulses with a 2.5V positive pulse voltage limit while ramping the current from 2A. The positive:negative pulse duty cycle was 0.5 (negative pulse half the length of the forward pulse). The interval between the positive pulse and the negative pulse was equal to the negative pulse length and a 200µs interval was placed between the negative pulse and the positive pulse. This waveform is shown in figure 4.18 in section 4.6.1.

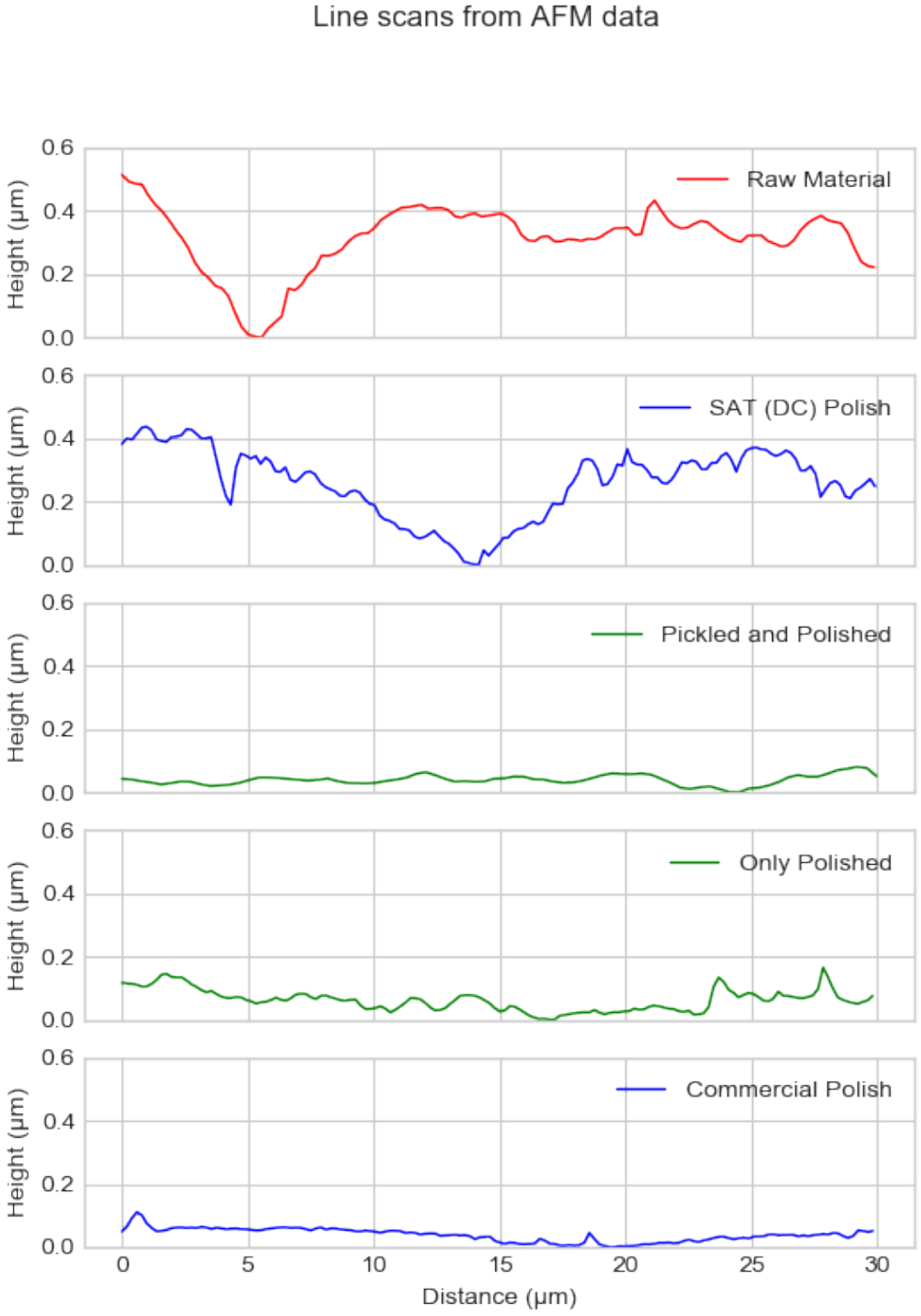

Figure 4.23: AFM line scans

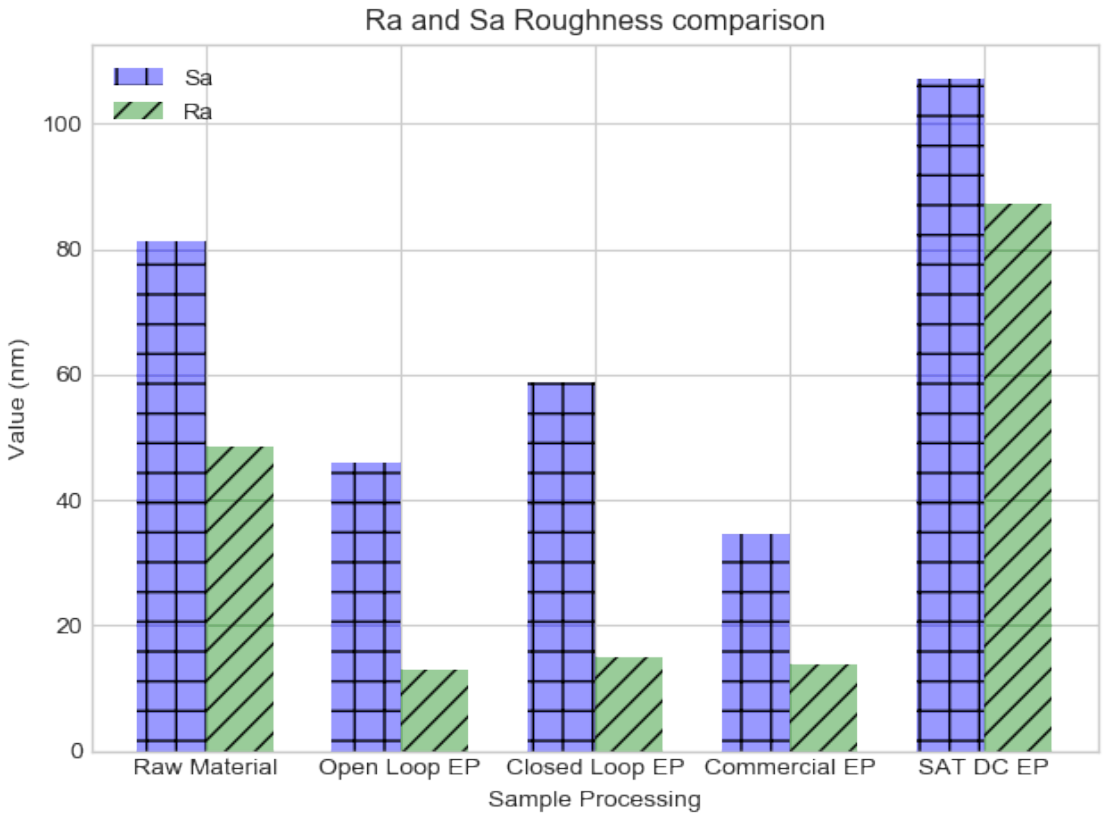

Figure 4.24: Roughness Comparison

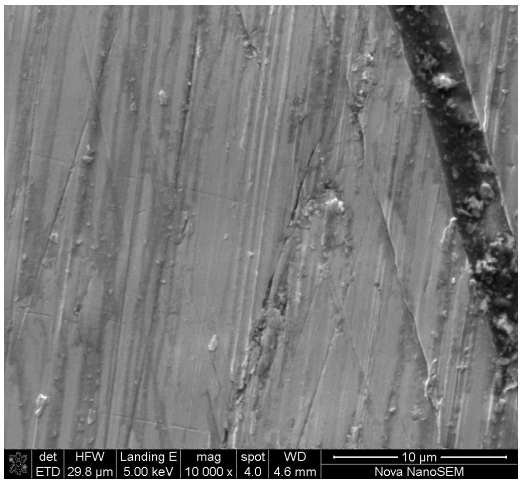

(a)SAT (DC) Electropolish

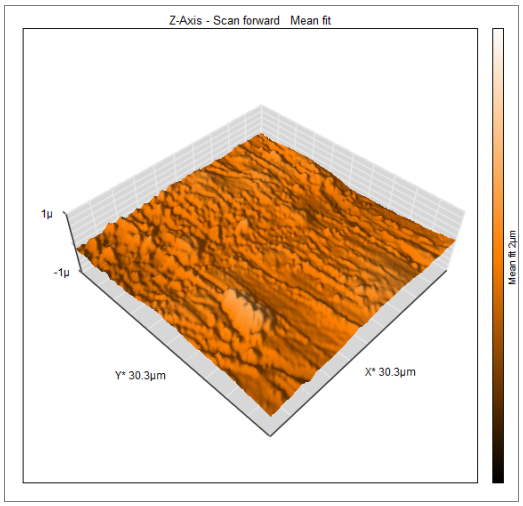

(b) SAT (DC)

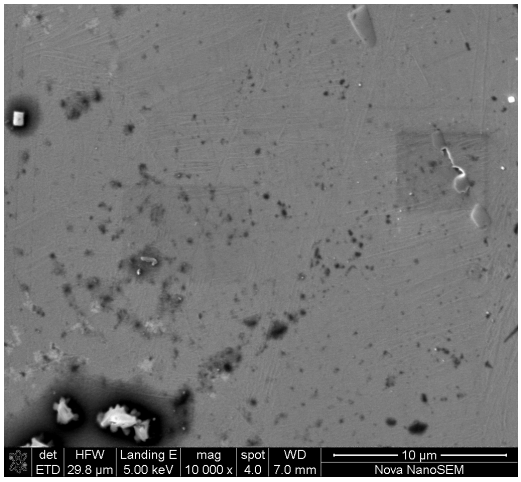

(c) Commercial Solution

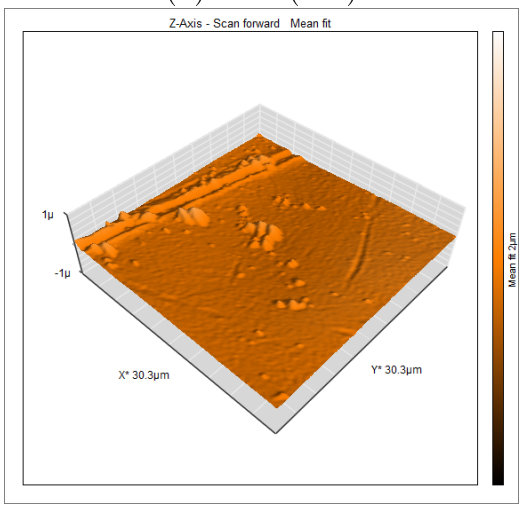

(d) Commercial Solution

Figure 4.25: AFM and SEM images of electropolished surfaces not produced in this thesis (a,b) Strait Access Technologies DC electropolish, (c,d) Commercial electropolishing

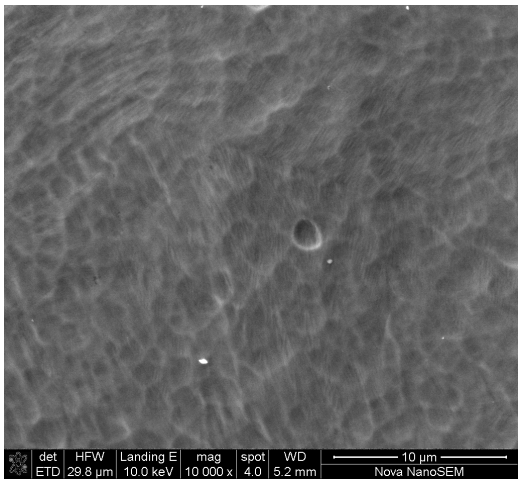

(a)

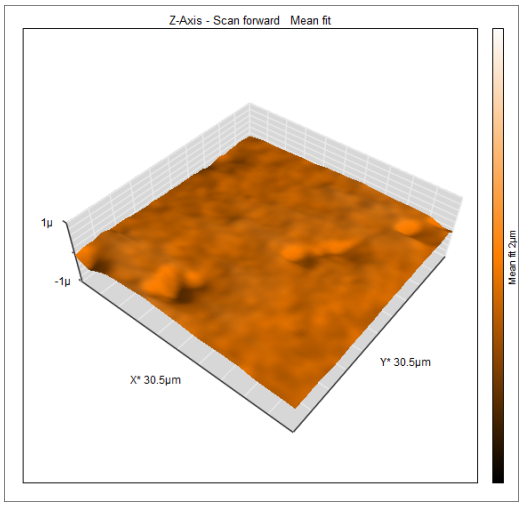

(b)

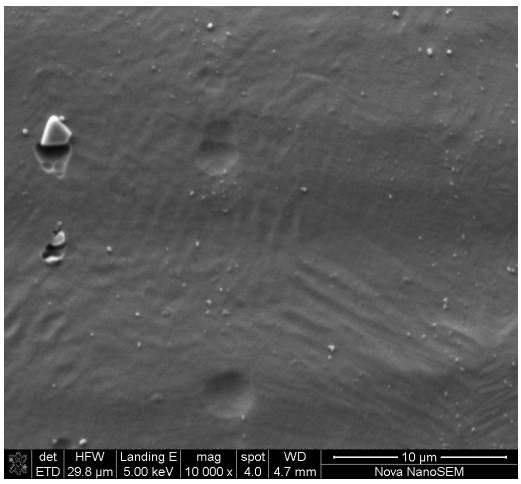

(c)

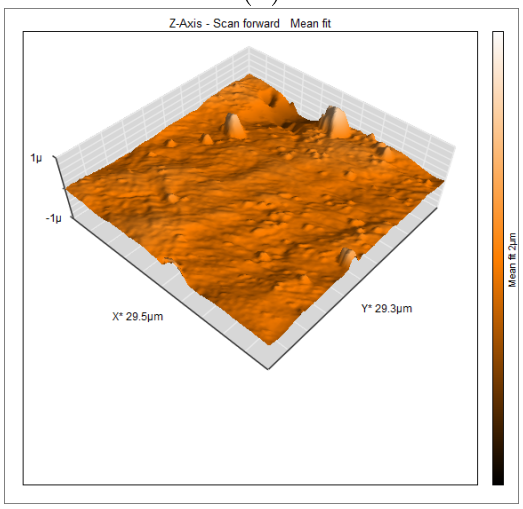

(d)

Figure 4.26: AFM and SEM images of electropolished surfaces produced in this thesis (a, b) Electropolished with pickling and open loop control (c,d)Electropolished without Pickling with closed loop control.

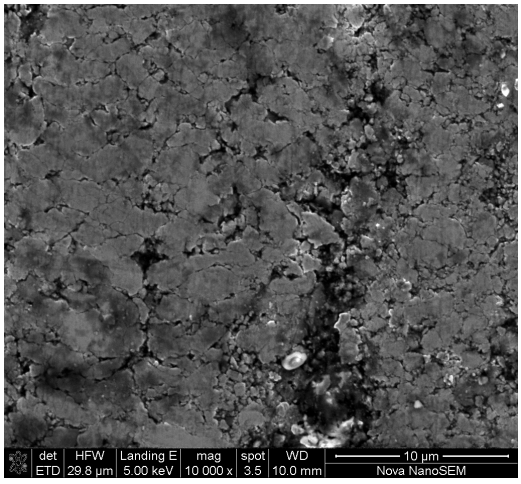

(a)

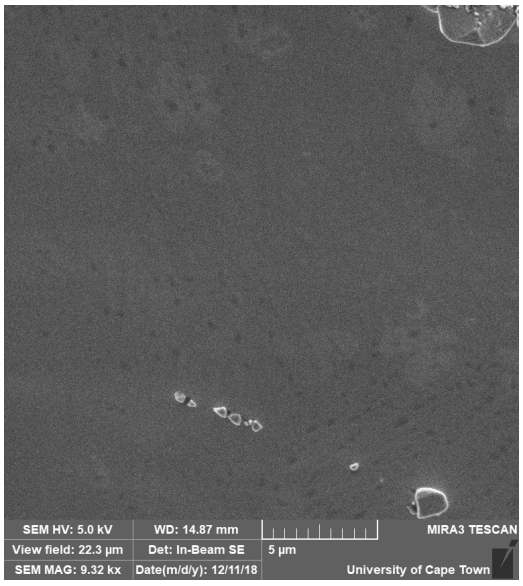

(b)

Figure 4.27: Change in surface topology on inner surface of Nitinol stent (a) Before thermosetting and electropolishing (b) after pulsatile closed loop electropolishing without pickling

Table 4.4: Comprehensive table of roughness values (kurtosis and skewness are included for completeness)

(a) Line Scan

Parameter from Line Scan	Raw Material	SAT (direct current)	Commercial Solution	Pulsatile with pickling s31	Pulsatile without pickling
Roughness Average (Ra) (nm)	48.62	87.39	13.94	12.97	14.9
Root Mean Square Roughness (Rq) (nm)	64.06	107.7	16.9	15.98	19.14
Average Maximum Height (Rz) (nm)	403	369.1	41.95	43.90	59.5
Scan Length (µm)	30.24	30.16	30.01	29.98	30.01
Skewness (Rsk)	-0.6276	-0.4088	1.050	-0.4713	0.3197
Kurtosis (Rk)	2.491	2.174	4.221	3.673	3.602

(b) Area Measurement (30x30 µm with mean plane subtraction to level the data)

Parameter From area analysis	Raw Material	SAT (direct current)	Commercial Solution	Pulsatile with pickling s31	Pulsatile without pickling
Roughness Average (Sa) (nm)	81.3 nm	107.2	34.73	45.91	58.85
Root Mean Square Roughness (Sq)(nm)	1244	131.7	48.06	57.84	97.03
Maximum Height (Sz)(nm)	1395	897	483.4	405.3	1239
Projected Area (μm^2)	943.6	915.9	915.9	928.3	851.2
Surface Area (μm^2)	966.5	933.0	919.4	929.4	858.3
Skew (Ssk)	0.9700	6.473 × 10-3	0.8830	-1.044	0.9789
Excess Kurtosis	8.712	-0.1673	3.619	1.448	13.43

4.10 Physiological Corrosion Testing

The following data was gathered according to the method laid out in section 3.3.4. The electropolished samples anaylzed where polished using a voltage feedback closed loop electropolishing method and paremeters described above in section 4.9. The purpose of this testing was to determine the minimum breakdown potential that can be expected to occur during implant in contact with blood. The de-aeration is performed to simulate worst case conditions where minimum dissolved oxygen is available to repassivate the surface. The results in Figure 4.28 indicate a breakdown potential (E_b) of 1.1V vs Ag/AgCl reference electrode (1.061V vs SCE), and a similarly high repassivation potential of 1.05V vs Ag/AgCl. A substantial improvement over the 0.2V (vs Ag/AgCl) breakdown potential that was observed prior to electropolishing (Figure 4.29). This shows that the electropolished surface has suitable corrosion characteristics for implant in the cardiovascular system, since no higher breakdown potential is reported for Nitinol in a de-aerated test solution anywhere in literature[68–73]. It is difficult to set a breakdown potential that will provide corrosion resistance in all physiological conditions. However, aside from comparing the performance with predicate devices that are operating successfully on the market, a general consensus among researchers is that a minimum E_b of 0.6V vs SCE is required for implant [69, 74].

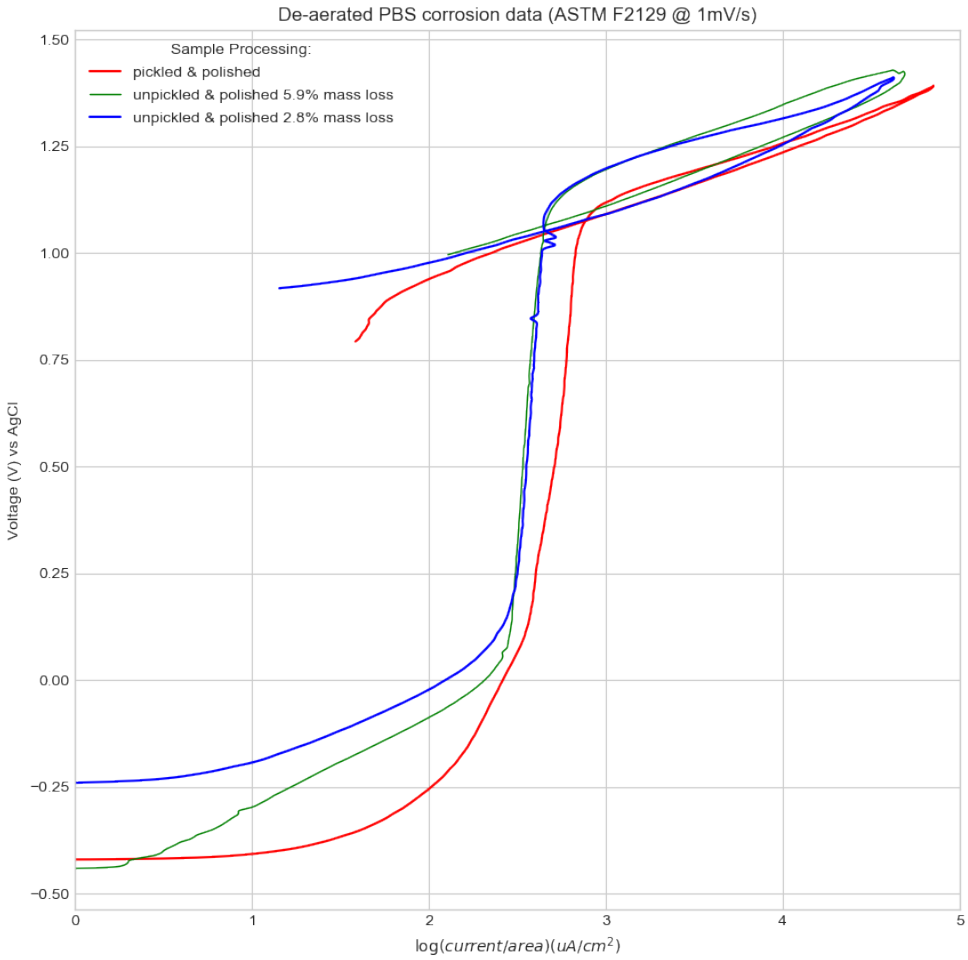

Figure 4.28: Cyclic polarization in PBS for charge balanced electropolishing (low pass filter applied to the data to eliminate spikes caused by touching the electrode leads during the test)

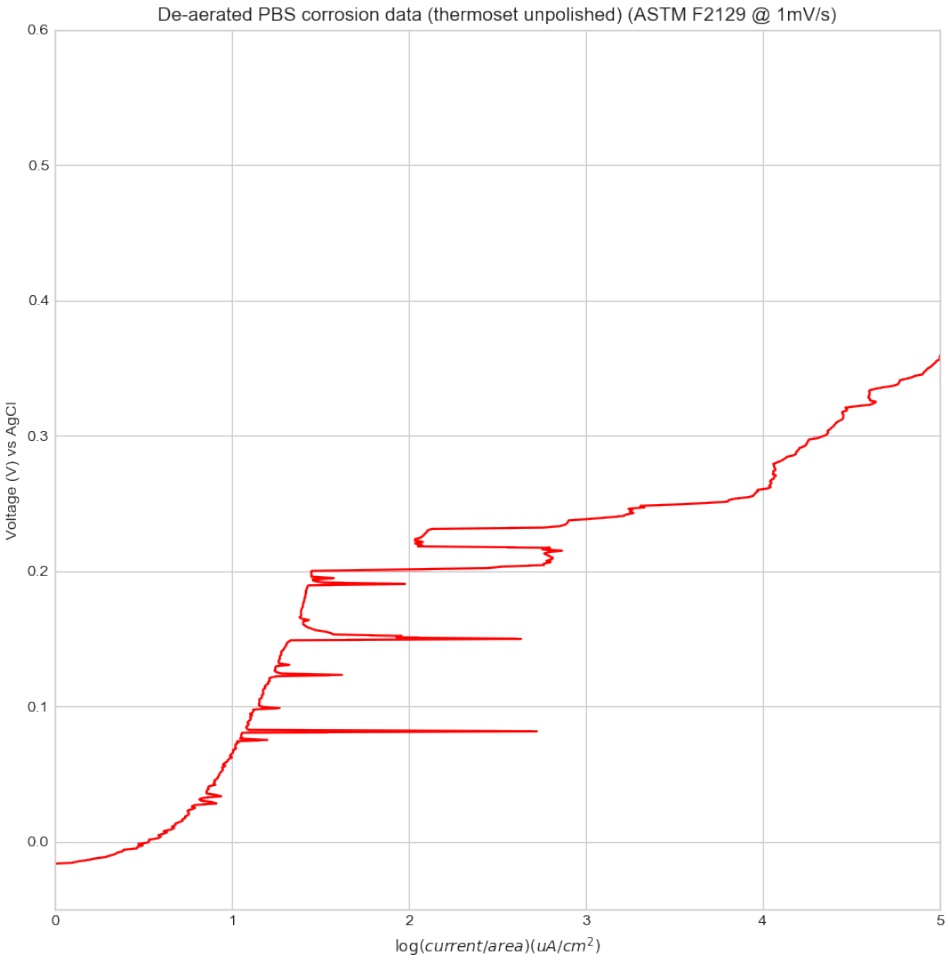

Figure 4.29: Cyclic polarization in PBS for unpolished thermoset sample

Chapter 5

Conclusions

5.1 Outcomes

The highly passive titanium dioxide component of Nitinol which is an impediment to electropolishing, was overcome using a rapidly alternating high current waveform. It was shown how the presented waveforms can achieve continuous uniform dissolution with a nanoscale electropolishing effect. A method for accurately and repeatably adjusting the surface morphology between patterns generated on the sub micrometer scale was described. Yuzhakov et al. report a similar nanoscale pattern emergence which they attribute to electric double layer effects on aluminium[75]. Improvement in roughness values on the surface of a laser cut Nitinol stent were optimized until ~50% reduction was achieved (48 nm Ra was reduced to 15 nm Ra with 8mg or 5% of the stents mass removed). Additionally, it was shown that the corrosion performance is sufficient for implant in human physiological environments with a breakdown potential (E_b) of 1.06V vs SCE. The smoothing results are compared with other stages of the process and with commercial solutions for the same raw material. Equivalent Ra values to those found in the commercial solution were observed. A feedback mechanism for surface composition utilizing differential pulse voltammetry was identified and used to select pulse waveform parameters. A closed loop control system that requires only one input parameter was made and tested on Nitinol stents. The need for a pickling process (and hence the use of hydrofluoric acid) was eliminated. Without the pickling stage a lesser degree of macro scale edge rounding was observed, and a higher incidence of surface inclusions was present post electropolishing. Shifting the temperature to perform electropolishing with the Nitinol in the austenitic crystal phase yields fewer inclusion.

5.2 Future Work

- The findings related to surface composition and pulsatile modification suggest the possibility of manufacturing materials with a custom surface that can be set in software without the need for complex electrolytes. With the use of an XPS enabled instrument and Augur electron spectroscopy, the differential pulse voltammogram could be converted to a quantitative measure. This would permit the generation of a truly programmable surface composition.

- The pulsatile control studied here relies on an alloy composition which includes a strongly oxidizing component. It may be possible to extend this control method to include the other two widely used medical alloys (Cobalt chromium and Stainless Steel).

- On a practical front, the design of an inert and universal stent attachment system that permits the stent to be immersed some distance below the surface is required for industrial applications. An epoxy coated tweezer mechanism that only leaves the contact point exposed is recommended, although it will require repositioning at least once to eliminated defects at the point of contact.

- Gaseous bubble diffusion and breakdown may be assisted in several ways:

  - Reducing or increasing reaction pressure (reduction raises gas solubility limit, increasing reduces bubble size). Further testing is required to determine how to minimize the effect of gas evolution on surface layer disturbance using pressure.
  - The use of a surfactant additive to the electrolyte that increases hydrogen and oxygen solubility and decreases surface tension.

- A suitable surfactant may provide a method of removing carbon inclusions that are revealed during dissolution.

There is some indication in literature and theory around electroplating regarding the characteristic length of the deposition effect[27, 31, 76]. This suggests that it may be possible to adjust the feature size which is affected purely through electrical parameter modification. It may require adjustments to electrolyte conductivity in order to facilitate the creation of a variable gradient in the charge density that tapers off away from the surface into the electrolyte bulk. Taylor et al report that several sets of pulse parameters are required which must be sequenced in order to produce surface smoothing on very rough surfaces (6 µm Ra was reduced to 1.8 µm Ra after removing 80 µm of material in this case)[77]. This was tested in this thesis using potentiostatic control prior to the publication of this information by Taylor et al. at the end of 2018. A sequence of galvanostatic closed loop control parameters must still be established to achieve a greater degree of micrometer scale roughness rounding without pickling.

5.2.1 Limitations

- Frequency of pulses was limited by the potentiostat to >2 ms.
- Current density was tested for values below 3 A/cm^2.
- No luggin capillary was used with the reference electrode due to concerns over response speed. Thus, there is some error in the measured potentials resulting from uncompensated solution resistance and electrode shielding. (this is minimized by the high conductivity of the electrolyte).

Appendix A

Chemical Solutions From Existing Publications

#	Material	Purpose	Process
1.	NiTi	Chemical Etching	10ml HF, 20ml HNO_3, 30ml H_2O [7]
2.	NiTi	Chemical Etching	4M aqueous KOH for 30 minutes at 120 °C [7]
3.	NiTi	Chemical Etching	saturated aqueous $Ca(OH)_2$in autoclave for 20h at 170 °C [7]
4.	NiTi	Electropolishing	33% nitric acid in methanol at -30 °C[7]
5.	NiTi	Electropolishing	5% perchloric acid in ethanol at 38V [7]
6.	NiTi	Electrochemical Etching	65% HNO_3in methanol (CH_3OH), volume ratio 33:67 (HNO_3: CH_3OH)[21]
7.	NiTi	Chemical Passivation	20% HNO_3@80 °C for 20 minutes[21]
8.	NiTi	Electropolishing	Aqueous solution of 30 wt% Sulfuric Acid (pulse reverse polishing)[11]
9.	NiTi	Electroetching	1 mol/l LiCl-Methanol (microscale stent etching)[10]
10.	NiTi	Electroetching	1 mol/l LiCl-Ethanol (microscale stent etching)[10]
11.	NiTi	Electro-etching	0.11 mol/l LiCl-ethanol (microscale stent etching)[10]
12.	NiTi	Electroetching	NH_4Cl - Methanol (microscale stent etching)[10]
13.	NiTi	Electro-Etching	1 mol/l H_2SO_4-methanol (microscale stent etching) - highest pitting of solutions 9-13[10]
14.	SS316L	Electropolish	2.4 mol/L H_2SO_4 , 5.9 mol/L H_3PO_4in distilled water. 50V, 12A Pulse 0.8 ms[36]
15.	SS	Electropolish	Aqueous ∼12% NaCl/$NaNo_3$(pulse reverse polishing)[31]

Appendix B

Electropolished Nitinol Surfaces From Literature

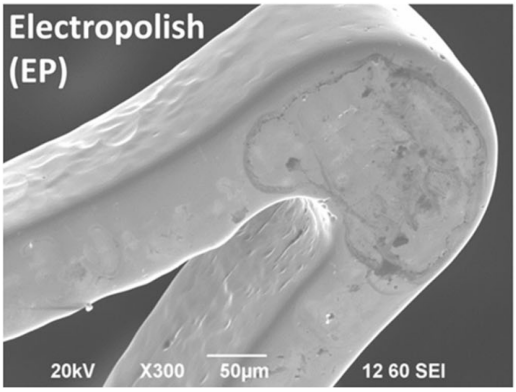

(a) Shabalovskaya DC electropolished[3]

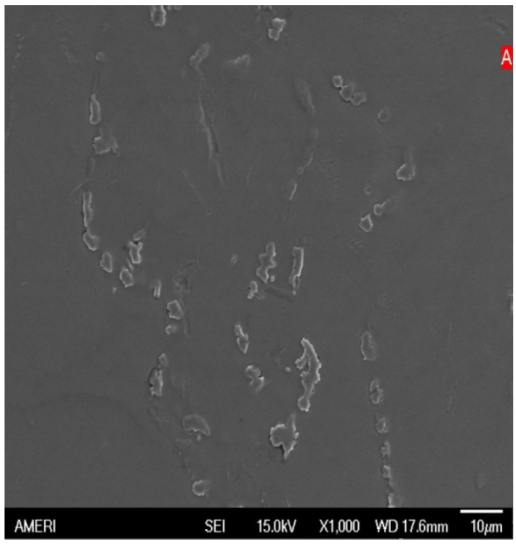

(b) Waseem Haider et al. (Magneto-electropolished)[78]

Figure B.1: Electropolished surfaces from literature

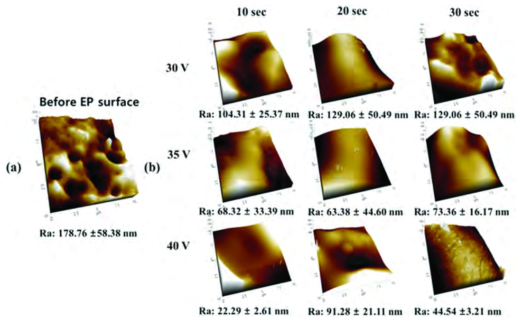

(a) J. Kim et al. DC Electropolished[79]

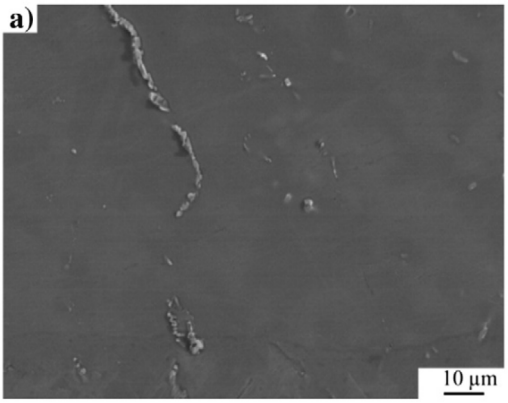

(b)P. Gill et al. Magneto-electropolished[80]

Figure B.2: Electropolished surfaces from literature (II)

Appendix C

Electronic Schematics

C.1 Potentiostat Controller Schematic

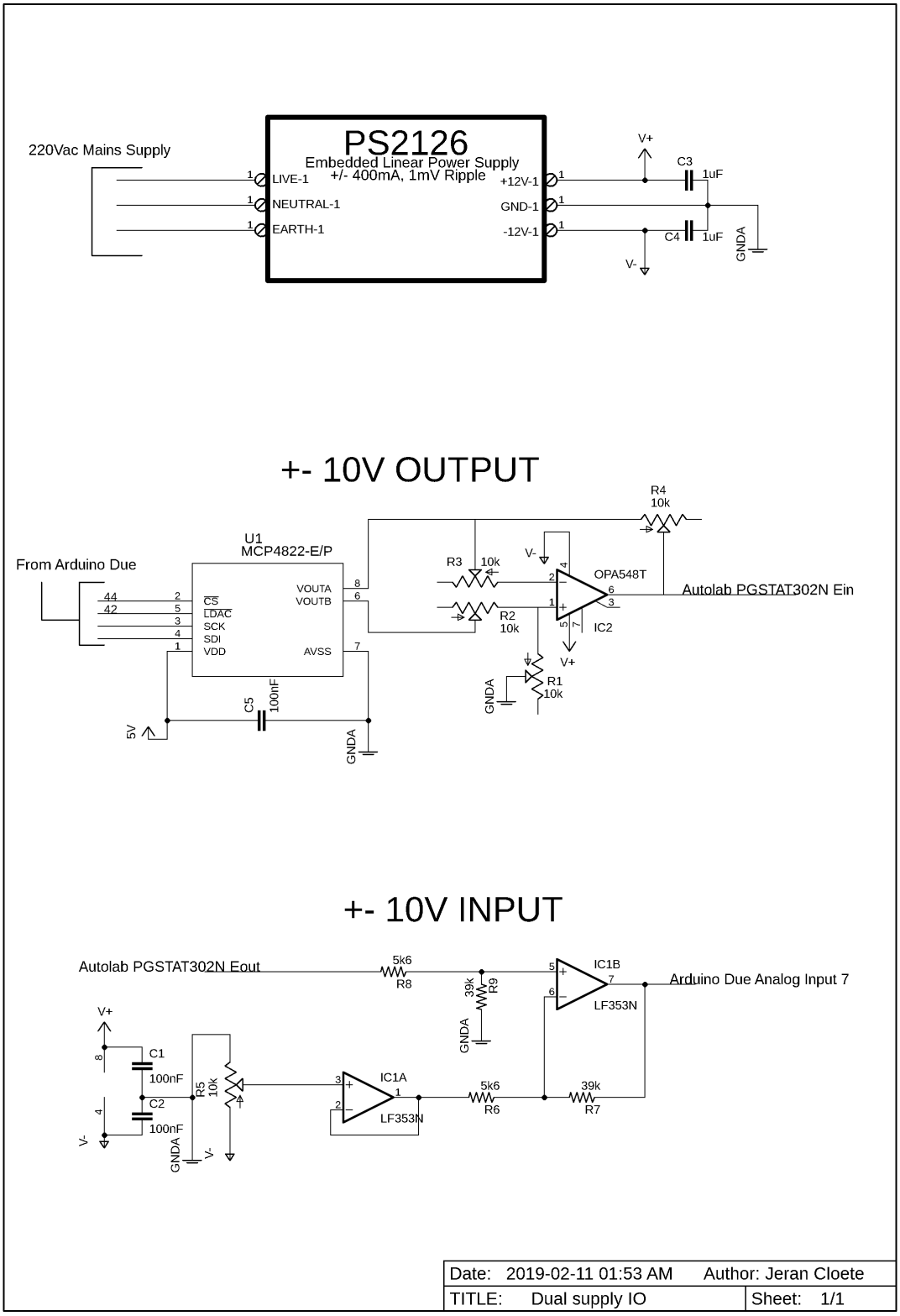

Figure C.1: Potentiostat Controller Schematic

C.2 Peristaltic Pump Schematic

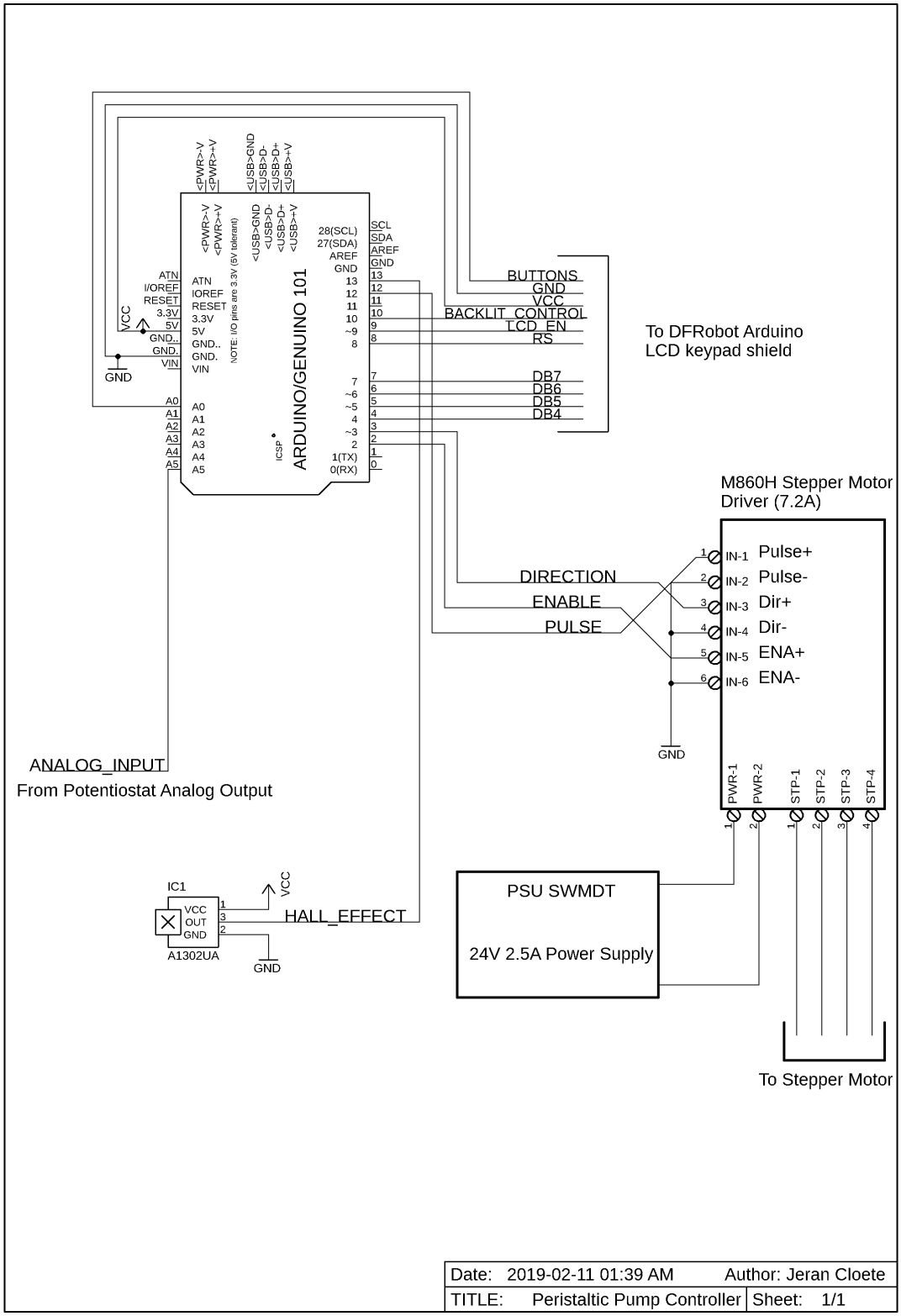

Figure C.2: Peristaltic Pump Schematic

Appendix D

Photographs of Manufactured Equipment

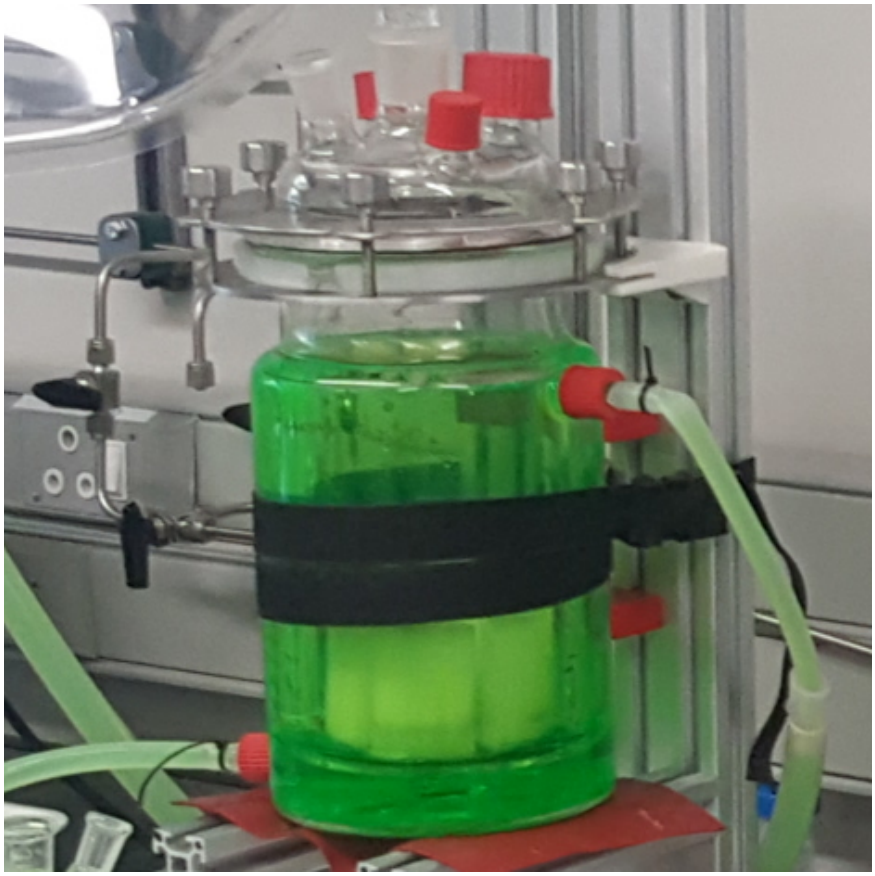

Figure D.1: Glasschem Reaction Vessel on Aluminium extrusion mount.

Figure D.2: Ultrasonic cleaner modified to create an internal jacketed beaker with coolant flow through the bath.

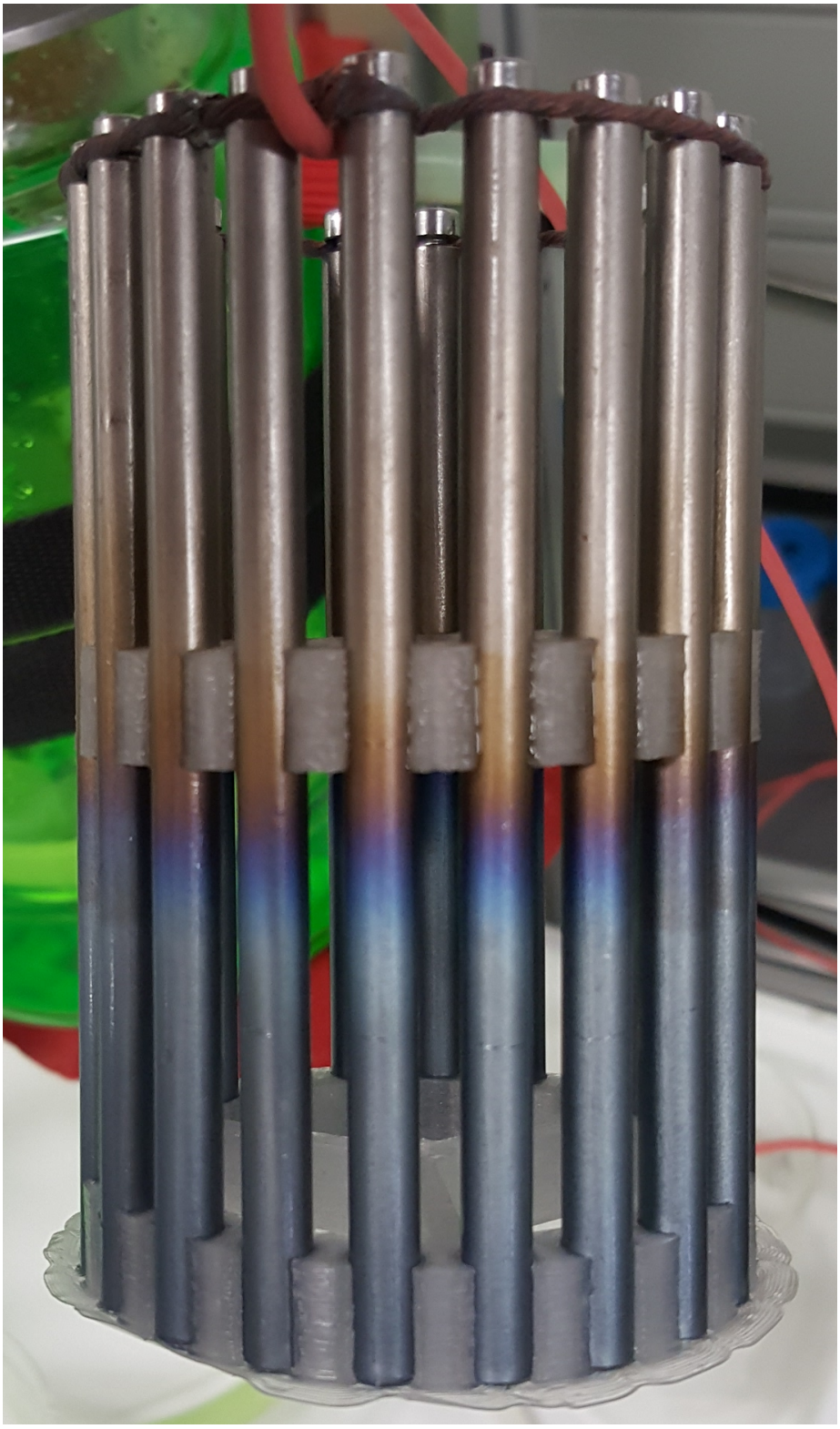

Figure D.3: titanium rod counter electrode.

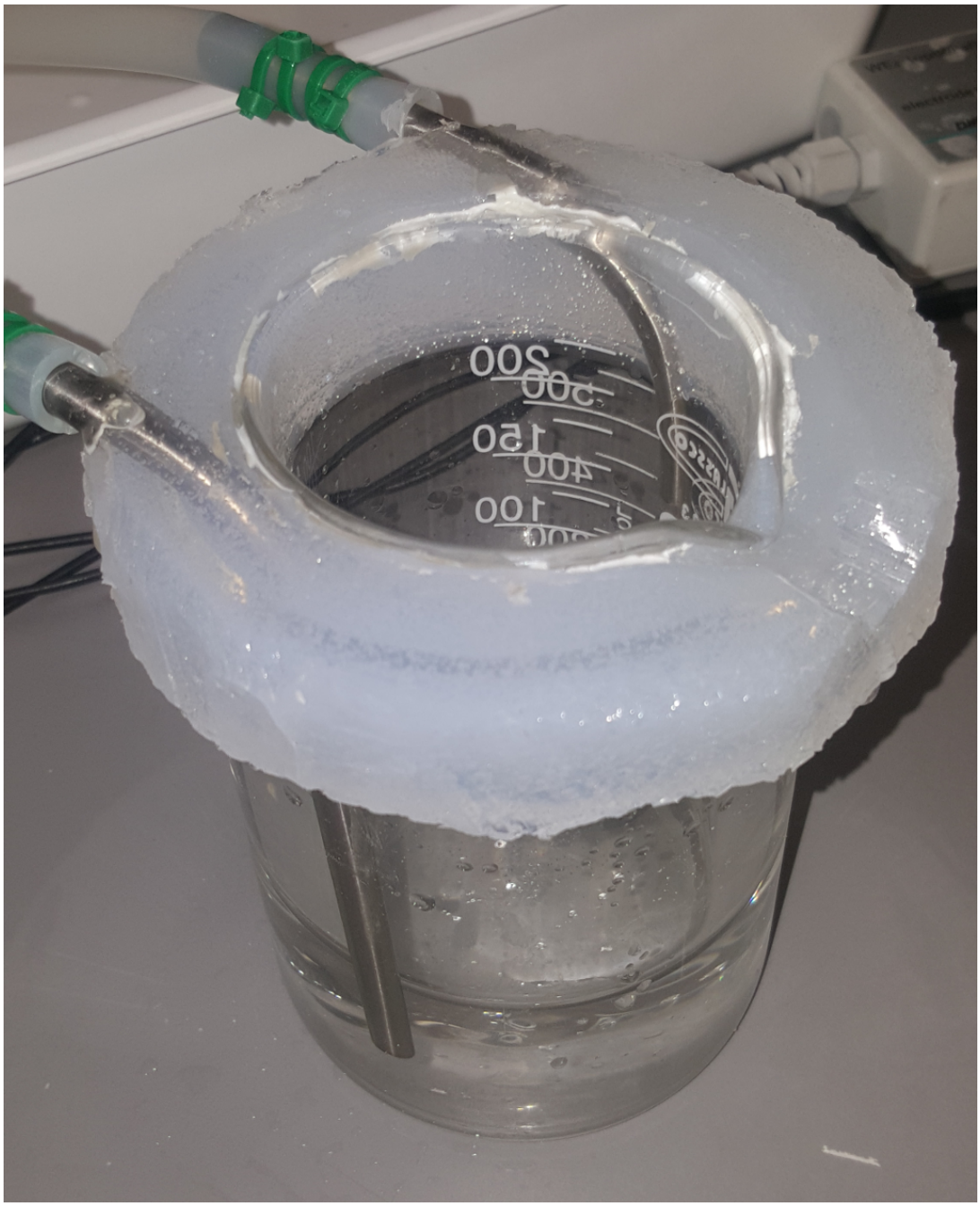

Figure D.4: DIY borosilicate beaker thermal exchange jacket.

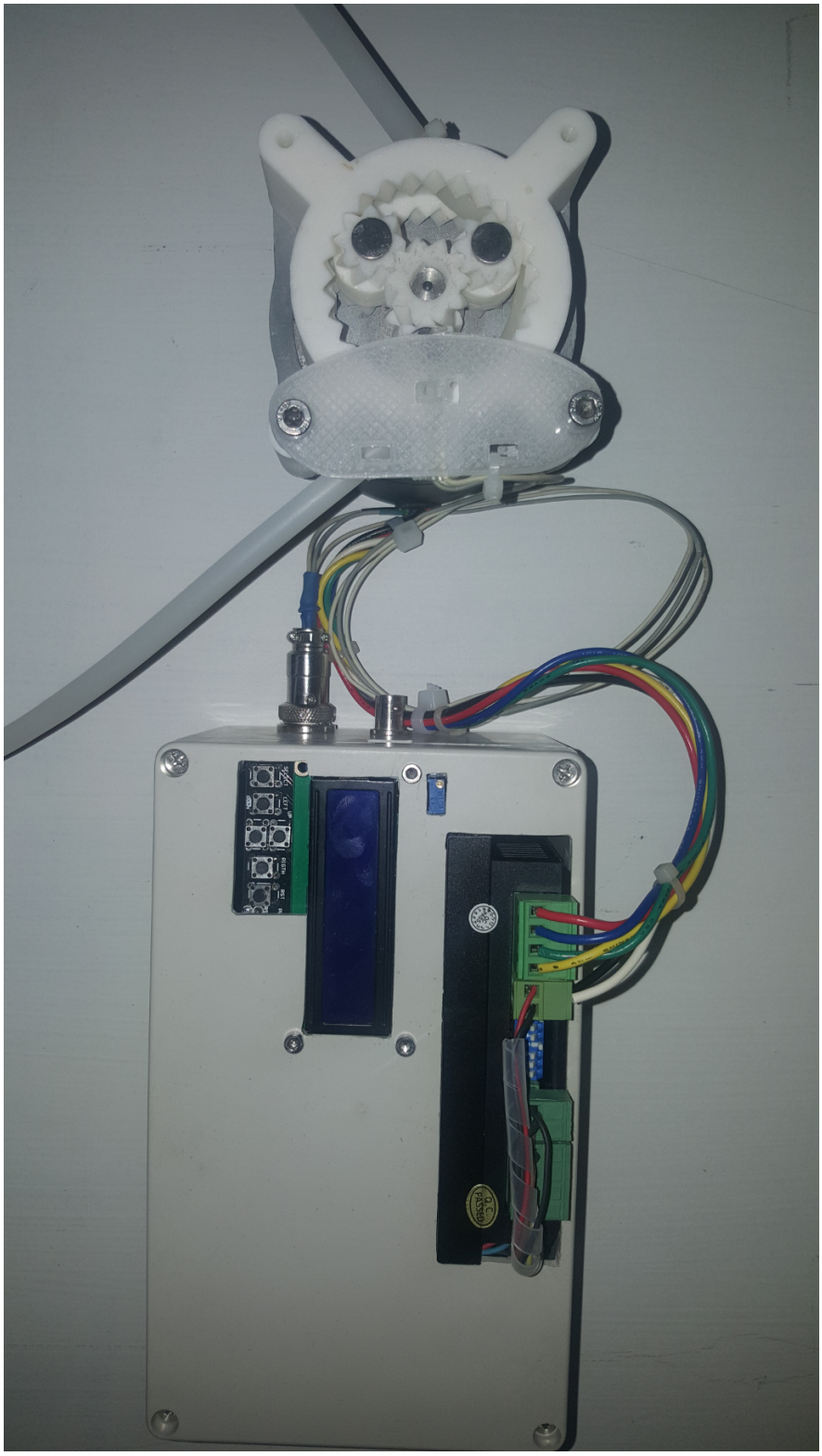

Figure D.5: Peristaltic Pump

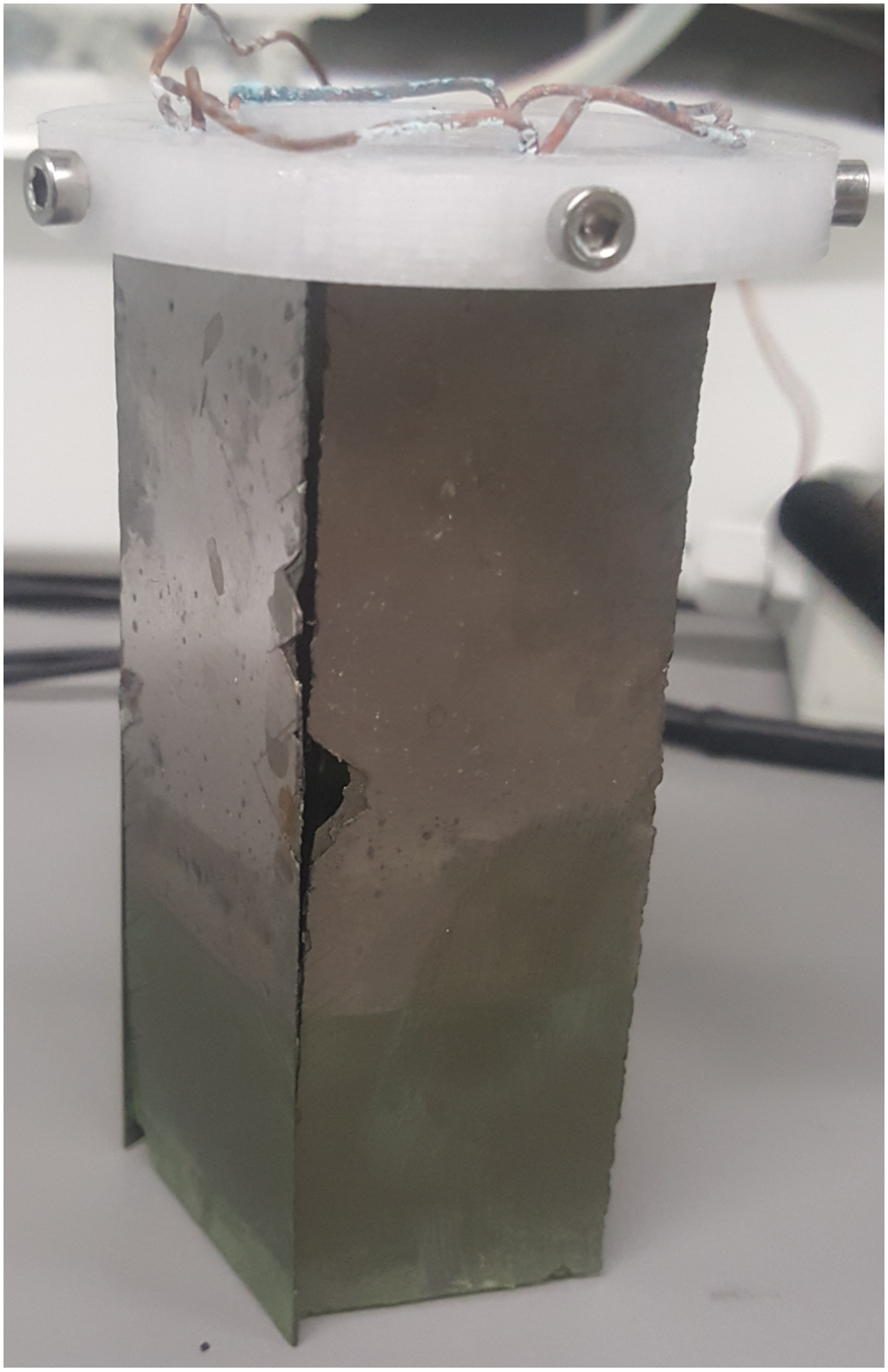

Figure D.6: tungsten plate counter electrode (plates arranged in a pentagon)

Bibliography

[1] Z. YANG et al. "Surface Modification of Nitinol By Chemical and Electrochemical Etching". In: *Modern Physics Letters B* 27.19 (2013), p. 1341012. ISSN: 0217-9849. DOI: 10.1142/S0217984913410121. URL: http://www.worldscientific.com/doi/abs/10.1142/S0217984913410121.

[2] X. Ma et al. "Electrochemical micromachining of nitinol by confined-etchant-layer technique". In: *Electrochimica Acta* 52.12 (2007), pp. 4191–4196. ISSN: 00134686. DOI: 10.1016/j.electacta.2006.11.046.

[3] S. Shabalovskaya, J. Anderegg and J. Van Humbeeck. "Critical overview of Nitinol surfaces and their modifications for medical applications". In: *Acta Biomaterialia* 4.3 (2008), pp. 447–467. ISSN: 17427061. DOI: 10.1016/j.actbio.2008.01.013.

[4] R. Podila et al. "Graphene coatings for enhanced hemo-compatibility of nitinol stents". In: *RSC Advances* 3.6 (2013), pp. 1660–1665. ISSN: 20462069. DOI: 10.1039/c2ra23073a.

[5] S. Spriano et al. "Processing and surface treatments for pseudoelastic wires and strands". In: *Materials and Manufacturing Processes* 32.4 (2017), pp. 394–403. ISSN: 15322475. DOI: 10.1080/10426914.2016.1198031.

[6] G. Tepe et al. "Reduced thrombogenicity of nitinol stents - In vitro evaluation of different surface modifications and coatings". In: *Biomaterials* 27.4 (2006), pp. 643–650. ISSN: 01429612. DOI: 10.1016/j.biomaterials.2005.06.004.

[7] A W Hassel. "Surface treatment of NiTi for medical applications". In: *Minimally Invasive Therapy and Allied Technologies* 13.4 (2004), pp. 240–247. ISSN: 13645706. DOI: 10.1080/13645700410020278.

[8] LibreTexts. "Pourbaix Diagrams". In: (2015). URL: https://chem.libretexts.org/Textbook%7B%5C_%7DMaps/Inorganic%7B%5C_%7DChemistry%7B%5C_%7DTextbook%7B%5C_%7DMaps/Map%7B%5C%%7D3A%7B%5C_%7DInorganic%7B%5C_%7DChemistry%7B%5C_%7D(Wikibook)/Chapter%7B%5C_%7D04%7B%5C%%7D3A%7B%5C_%7DRedox%7B%5C_%7DStability%7B%5C_%7Dand%7B%5C_%7DRedox%7B%5C_%7DReactions/4.5%7B%5C%%7D3A%7B%5C_%7DPourbaix%7B%5C_%7Ddiagrams.

[9] Jongsik Choi et al. "Calcium phosphate coating of nickel-titanium shape-memory alloys. Coating procedure and adherence of leukocytes and platelets". In: *Biomaterials* 24.21 (2003), pp. 3689–3696. ISSN: 01429612. DOI: 10.1016/S0142-9612(03)00241-2.

[10] T. Mineta, Y. Haga and M. Esashi. "ELECTROCHEMICAL ETCHING OF SHAPE MEMORY ALLOY USING NEW ELECTROLYTE SOLUTIONS". In: *Yamagata Research institute of Technology* ().

[11] M Inman et al. "Electropolishing and Throughmask ElectroEtching of Nitinol Stents and Other Materials in an Aqueous Electrolyte". In: ().

[12] S. X. Karamichailidou and G. Haidemenopoulos. "The Unique Properties , Manufacturing Processes and Applications of Near Equatomic Ni-Ti Alloys". In: *University of Thessaly Department of Mechanical Engineering Laboratory of Materials* (2016).

[13] H. Ibrahim et al. "In Vitro Corrosion Assessment of Additively Manufactured Porous NiTi Structures for Bone Fixation Applications". In: *Metals* 8.3 (2018), p. 164. ISSN: 2075-4701. DOI: 10.3390/met8030164. URL: http://www.mdpi.com/2075-4701/8/3/164.

[14] A Baran and M Polanski. "Microstructure and properties of LENS (laser engineered net shaping) manufactured Ni-Ti shape memory alloy". In: *Journal of Alloys and Compounds* 750 (2018), pp. 863–870. ISSN: 09258388. DOI: 10.1016/j.jallcom.2018.03.400. URL: https://doi.org/10.1016/j.jallcom.2018.03.400.

[15] M Monai, T Montini and P Fornasiero. "Brookite: Nothing New under the Sun?" In: *Catalysts* 7.10 (2017), p. 304. ISSN: 2073-4344. DOI: 10.3390/catal7100304. URL: http://www.mdpi.com/2073-4344/7/10/304.

[16] L Zhu et al. "Oxidation of Nitinol and Its Effect on Corrosion Resistance". In: *ASM Materials & Processes for Medical Device Conference 2003* 683 (2003), pp. 1–7. URL: http://citeseerx.ist.psu.edu/viewdoc/download;jsessionid=0E2F52EE19D438E5784AA7763A42A0CB?doi=10.1.1.620.2892%7B%5C&%7Drep=rep1%7B%5C&%7Dtype=pdf.

[17] G Jerkiewicz et al. "Discovery of reversible switching of coloration of passive layers on titanium". In: *Chemistry of Materials* 20.5 (2008), pp. 1877–1880. ISSN: 08974756. DOI: 10.1021/cm703052p.

[18] C. G. Slough. *A Study of the Nitinol Solid-Solid Transition by DSC*. Tech. rep. 7. 2007, pp. 1–5.

[19] A. Feeney and M. Lucas. "Differential scanning calorimetry of superelastic Nitinol for tunable cymbal transducers". In: *Journal of Intelligent Material Systems and Structures* 27.10 (2016), pp. 1376–1387. ISSN: 15308138. DOI: 10.1177/1045389X15591383.

[20] A. Apolinário et al. "Tailoring the Ti surface via electropolishing nanopatterning as a route to obtain highly ordered TiO2 nanotubes". In: *Nanotechnology* 25.48 (2014). ISSN: 13616528. DOI: 10.1088/0957-4484/25/48/485301.

[21] Z Huan et al. "Synthesis and characterization of hybrid micro/nano-structured NiTi surfaces by a combination of etching and anodizing". In: *IOP Publishing* 25 (2014). DOI: 10.1088/0957-4484/25/5/055602.

[22] C. Lutter et al. "Effect of specific surface microstructures on substrate endothelialisation and thrombogenicity: Importance for stent design". In: *Clinical Hemorheology and Microcirculation* 59.3 (2015), pp. 219–233. ISSN: 18758622. DOI: 10.3233/CH-141839.

[23] A. K. Solomon. *Encylopaedia Britannica Online*. URL: https://www.britannica.com/science/biophysics%7B%5C#%7Dref498219 (visited on 08/07/2018).

[24] R. Desai. *Fick's Law of Diffusion*. URL: https://www.khanacademy.org/science/health-and-medicine/respiratory-system/gas-exchange-jv/v/fick-s-law-of-diffusion (visited on 11/02/2018).

[25] D A C Brownson and C E Banks. "Interpreting Electrochemistry". In: *The Handbook of graphene electrochemistry*. Springer, 2014, pp. 23–77. DOI: 10.1007/978.

[26] Comsol. *Diffusion Equation*. URL: https://www.comsol.com/multiphysics/diffusion-equation (visited on 11/02/2018).

[27] G. S Frankel et al. *Encyclopedia of Electrochemistry*. 2003, p. 745. ISBN: 978-3-527-30396-0. DOI: 10.1179/000705968798326370.

[28] University of Cambridge. *The Electrical Double layer*. URL: https://www.ceb.cam.ac.uk/research/groups/rg-eme/teaching-notes/the-electrical-double-layer (visited on 05/03/2018).

[29] R. Nave. *Fermi Level*. 2018. URL: http://hyperphysics.phy-astr.gsu.edu/hbase/Solids/Fermi.html.

[30] P. B. Tailor, A. Agrawal and S. S. Joshi. "Numerical modeling of passive layer formation and stabilization in electrochemical polishing process". In: *Journal of Manufacturing Processes* 18 (2015), pp. 107–116. DOI: 10.1016/j.jmapro.2015.02.001.

[31] E. J. Taylor et al. "Breaking the Chemical Paradigm in Electrochemical Engineering : Case Studies and Lessons Learned from Plating to Polishing". In: ().

[32] A. F. Teixeira. "Development of an Electropolishing Method for Titanium Materials". In: *Concordia University* March (2011), p. 82.

[33] E. J. Taylor and M. E. Inman. "Electrochemical Surface finishing". In: *The electrochemical society interface* (2014).

[34] N Ibl, J C1 Puippe and H Angerer. "ELECTROCRYSTALLIZATION IN PULSE ELECTROLYSIS". In: *Surface Technology Elsevier Sequoia S.A* 6 (1978), pp. 287–300.

[35] S C Chen, G C Tu and C A Huang. "The electrochemical polishing behavior of porous austenitic stainless steel (AISI 316L) in phosphoric-sulfuric mixed acids". In: *Surface and Coatings Technology* 200.7 (2005), pp. 2065–2071. ISSN: 02578972. DOI: 10.1016/j.surfcoat.2005.06.008.

[36] YB. Kim and JW. Park. "Effect of pulse time on surface characteristics and corrosion resistance during pulse electrochemical polishing". In: *Trans. Nonferrous Met. Soc. China* 22 (2012), pp. 876–880. DOI: 10.1016/S1003-6326(12)61819-6.

[37] K. Nestler et al. "ScienceDirect Plasma Electrolytic Polishing - an Overview of Applied Technologies and Current Challenges to Extend the Polishable Material Range". In: *Procedia CIRP* 42 (2016), pp. 503–507. ISSN: 2212-8271. DOI: 10.1016/j.procir.2016.02.240.

[38] M. Cornelsen, C. Deutsch and H. Seitz. "Electrolytic Plasma Polishing of Pipe Inner Surfaces". In: *Metals* 8.1 (2017), p. 12. ISSN: 2075-4701. DOI: 10.3390/met8010012. URL: http://www.mdpi.com/2075-4701/8/1/12.

[39] V. Palmieri. "Fundamentals of electrochemistry - the electrolytic polishing of metals: application to copper and niobium". In: *ISTITUTO NAZIONALE DI FISICA NUCLEARE* (2003).

[40] K. Kontturi and D. J. Schiffrin. "Diffusion and migration in the electropolishing and anodic dissolution of metals". In: *Journal of Applied Electrochemistry* 19.1 (1989), pp. 76–82. ISSN: 0021891X. DOI: 10.1007/BF01039393.

[41] Anshuman Bhuyan et al. "PULSE AND DC ELECTROPOLISHING OF STAINLESS STEEL FOR STENTS AND OTHER DEVICES". In: 1 ().

[42] L. Yang et al. "Further study of the electropolishing of Ti6Al4V parts made via electron beam melting". In: *University of Louisville, Louisville, KY 40292* ().

[43] Hartmut Surmann and Jog Huser. "Automatic electropolishing of cobalt chromium dental cast alloys with a fuzzy logic controller". In: *Computers Chem Eng.* 22.7-8 (1998), pp. 1099–1111.

[44] K. Bhushan B. Winkelmann. *Atomic Force Miscroscopy*. URL: https://www.nanosurf.com/en/support/afm-modes (visited on 25/02/2018).

[45] Research Asylum. "Measuring Surface Roughness with Atomic Force Microscopy". In: *Asylum Research an Oxford Instruments company* (2013), pp. 2–3. URL: https://www.asylumresearch.com/Applications/SurfaceRoughness/SurfaceRoughness.pdf.

[46] V Prasad, D Semwogerere and E. R. Weeks. "Confocal microscopy of colloids". In: *J. Phys.: Condens. Matter* 19 (2007), pp. 113102–25. DOI: 10.1088/0953-8984/19/11/113102.

[47] Andor. *Andor Confocal Microscope Product Brochure*. URL: http://www.andor.com/microscopy-systems/dragonfly?gclid=EAIaIQobChMI55advM7J2QIV4Z3tCh3
NPD%7B%5C_%7DBwE (visited on 01/03/2018).

[48] K. R. Spring, T. J. Fellers and M. W. Davidson. *Resolution and Contrast in Confocal Microscopy*. URL: https://www.olympus-lifescience.com/en/microscope-resource/primer/techniques/confocal/resolutionintro/ (visited on 01/03/2018).

[49] S. Banerjee et al. "Scanning Electron Microscopy Measurements of the Surface Roughness of Paper". In: (2009), pp. 4322–4325.

[50] W van Aarle et al. "The ASTRA Toolbox: A platform for advanced algorithm development in electron tomography". In: *Ultramicroscopy* 157 (2015), pp. 35–47. ISSN: 18792723. DOI: 10.1016/j.ultramic.2015.05.002. URL: http://dx.doi.org/10.1016/j.ultramic.2015.05.002.

[51] A. A Rowe et al. "CheapStat: An Open-Source, "Do-It-Yourself" Potentiostat for Analytical and Educational Applications". In: *PLoS ONE* (2011), pp. 3–9.

[52] M. D.M. Dryden and A. R. Wheeler. "DStat: A versatile, open-source potentiostat for electroanalysis and integration". In: *PLoS ONE* 10.10 (2015), pp. 1–17. ISSN: 19326203. DOI: 10.1371/journal.pone.0140349.

[53] M. P.S. Mousavi et al. "Avoiding Errors in Electrochemical Measurements: Effect of Frit Material on the Performance of Reference Electrodes with Porous Frit Junctions". In: *Analytical Chemistry* 88.17 (2016), pp. 8706–8713. ISSN: 15206882. DOI: 10.1021/acs.analchem.6b02025.

[54] W. Botter, D. M. Scares and O. Teschke. "The influence of the Luggin capillary on the response time of a reference electrode". In: *Journal of Electroanalytical Chemistry* 267.1-2 (1989), pp. 279–286. ISSN: 00220728. DOI: 10.1016/0022-0728(89)80255-4.

[55] Nitinol Devices & Components. "Material Data Sheet of Superelastic Nitinol Alloys". In: 94539.510 (2014), p. 94539. URL: http://www.nitinol.com/wp-content/uploads/2012/01/Material-Data-Sheet-Superelastic.pdf.

[56] C. H. Fu, J. F. Liu and A Guo. "Statistical characteristics of surface integrity by fiber laser cutting of Nitinol vascular stents". In: *Applied Surface Science* 353 (2015), pp. 291–299. ISSN: 01694332. DOI: 10.1016/j.apsusc.2015.06.105.

[57] H Y Zheng, A R Zareena and H Huang. "Femtosecond Laser Processing of Nitinol". In: *Applied Surface Science* 228 (2004), pp. 206–221.

[58] ASTM. *Standard Guide for Descaling and Cleaning Titanium and Titanium Alloy*. 2011. DOI: 10.1520/B0600-09.1. URL: https://www.astm.org/Standards/B600.htm.

[59] A. N. Campbell. "The conductances of aqueous solutions of sulphuric acid at 50 and 75 C". In: *Canadian Journal of Chemistry* 31 (1953).

[60] Metrohm Autolab B.V. "Nova Software User manual". In: April (2007), pp. 1–52. ISSN: 0010-468X. DOI: 10.1007/SpringerReference_28001. arXiv: arXiv:1011.1669v3.

[61] Microscopy Australia. *Myscope Training*. 2014. URL: https://myscope.training/legacy/analysis/eds/accuracy/ (visited on 30/12/2018).

[62] Tim "Drmn4ea". *Parametric Peristaltic Pump*. URL: https://www.thingiverse.com/thing:454702 (visited on 20/08/2005).

[63] S A. Shabalovskaya et al. "The electrochemical characteristics of native Nitinol surfaces". In: *Biomaterials* 30.22 (2009), pp. 3662–3671. ISSN: 01429612. DOI: 10.1016/j.biomaterials.2009.03.034. URL: http://dx.doi.org/10.1016/j.biomaterials.2009.03.034.

[64] B Katona et al. "Chemical etching of nitinol stents". In: *Acta of Bioengineering and Biomechanics* 15.4 (2013), pp. 3–8. ISSN: 1509409X. DOI: 10.5277/abb130401.

[65] P. Lazic K.A. Persson, B. Waldwick. *Prediction of solid-aqueous equilibria: scheme to combine first-principles calculations of solids with experimental aqueous states*. 2012. URL: www.materialsproject.org/%7B%5C#%7Dapps/pourbaixdiagram.

[66] S Hrapovic et al. "Morphology, chemical composition, and electrochemical characteristics of colored titanium passive layers". In: *Langmuir* 17.10 (2001), pp. 3051–3060. ISSN: 07437463. DOI: 10.1021/la001694s.

[67] S. P. Ong et al. "Python Materials Genomics (pymatgen): A robust, open-source python library for materials analysis". In: *Computational Materials Science* 68 (2013), pp. 314–319. ISSN: 09270256. DOI: 10.1016/j.commatsci.2012.10.028. URL: http://dx.doi.org/10.1016/j.commatsci.2012.10.028.

[68] B. G. Pound. "Corrosion behavior of nitinol in blood serum and PBS containing amino acids". In: *Journal of Biomedical Materials Research - Part B Applied Biomaterials* 94.2 (2010), pp. 287–295. ISSN: 15524981. DOI: 10.1002/jbm.b.31647.

[69] M. K. Lonn, J. M. Metcalf and B. D. Choules. "In Vivo and In Vitro Nitinol Corrosion Properties". In: *Shape Memory and Superelasticity* 1.3 (2015), pp. 328–338. ISSN: 2199-384X. DOI: 10.1007/s40830-015-0036-x. URL: http://link.springer.com/10.1007/s40830-015-0036-x.

[70] B. G. Pound. "Susceptibility of nitinol to localized corrosion". In: *Journal of Biomedical Materials Research - Part A* 77.1 (2006), pp. 185–191. ISSN: 00219304. DOI: 10.1002/jbm.a.30584.

[71] M. Di Prima, E. Gutierrez and J. D. Weaver. "The effect of fatigue on the corrosion resistance of common medical alloys". In: *Journal of Biomedical Materials Research - Part B Applied Biomaterials* 105.7 (2017), pp. 2019–2026. ISSN: 15524981. DOI: 10.1002/jbm.b.33738.

[72] A Nissan et al. "Effect of long-term immersion on the pitting corrosion resistance of nitinol". In: *SMST-2007 - Proceedings of the International Conference on Shape Memory and Superelastic Technologies* (2008), pp. 271–278. DOI: 10.1361/cp2007smst271.

[73] G Nuno and S Mealha. "ENHANCEMENT OF NITI ALLOYS BIOCOMPATIBILITY AND CORROSION RESISTANCE BY THERMAL TREATMENTS". In: *Tecnico Lisboa University* December (2016).

[74] C C Shih et al. "Increased corrosion resistance of stent materials by converting current surface film of polycrystalline oxide into amorphous oxide". In: *Journal of Biomedical Materials Research* 52.2 (2000), pp. 323–332. ISSN: 00219304. DOI: 10.1002/1097-4636(200011)52:2<323::AID-JBM11>3.0.CO;2-Z.

[75] V. V. Yuzhakov et al. "Pattern selection during electropolishing due to double-layer effects". In: *Chaos* 9.1 (1999), pp. 62–77. ISSN: 10541500. DOI: 10.1063/1.166380.

[76] K Juttner. *Electrochemical Engineering*. Vol. 5. 2007. ISBN: 9783527303977. DOI: 10.1002/9783527610426.bard050001. URL: http://doi.wiley.com/10.1002/9783527610426.bard050001.

[77] T. D. Hall et al. "Electrochemical surface finishing of additively manufactured parts". In: *ECS Transactions* 85.4 (2018), pp. 155–166.

[78] W Haider. "Enhanced biocompatibility of NiTi (Nitinol) via surface treatment and alloying". In: *FIU Electronic Theses and Dissertations* Paper 177 (2010). DOI: 10.25148/etd.FI10041612.

[79] J Kim et al. "Optimization of Electropolishing on NiTi Alloy Stents and Its Influence on Corrosion Behavior". In: *Journal of Nanoscience and Nanotechnology* 17.4 (2017), pp. 2333–2339. ISSN: 1533-4880. DOI: 10.1166/jnn.2017.13324. URL: http://www.ingentaconnect.com/content/10.1166/jnn.2017.13324.

[80] P Gill et al. "Surface modification of NiTi alloys for stent application after magnetoelectropolishing". In: *Materials Science and Engineering C 50* 50 (2015), pp. 37–44. DOI: 10.1016/j.msec.2015.01.009.